UNIVERSIDAD MICHOACANA DE SAN NICOLÁS DE HIDALGO

DIVISIÓN DE ESTUDIOS DE POSGRADO DE LA FACULTAD DE INGENIERÍA ELÉCTRICA

"DETERMINATION OF STEADY-STATE AND TRANSIENTLY STABLE OPTIMAL EQUILIBRIUM POINTS IN ELECTRIC POWER SYSTEMS"

BY

ALEJANDRO PIZANO MARTÍNEZ

THESIS

REQUERIMENT FOR THE DEGREE OF

DOCTOR IN SCIENCES IN ELECTRICAL ENGINEERING

ADVISOR

DR. CLAUDIO RUBÉN FUERTE ESQUIVEL

CO-ADVISOR

DR. DANIEL RUÍZ VEGA

MORELIA, MICHOACÁN FEBRUARY 2010

Acknowledgements

I would firstly like to thank and acknowledge my advisor Prof. Claudio Rubén Fuerte Esquivel, for his support and guidance during this Ph.D. research work, but also during my master degree studies. In all our meetings he has provided appreciated attention, experience, knowledge and friendship, always encouraging me to carry out my research work. I had the pleasure of sharing with him my Doctoral research living, frequently very good meals and sometimes soccer matches.

I wish to thank my co-advisor Prof. Daniel Ruiz Vega, he gave guidance to my research work since early stages of my Doctoral studies. He has been always available to provide very valuable knowledge, appreciated time and wise suggestions.

I take advantage of this particular opportunity to acknowledge the very valuable job of each one of my professors; they provided me great classes, valuable discussions and a great example of professionalism.

To the División de Estudios de Posgrados de la FIE de la UMSNH, where I had the great opportunity of carrying out posgraduate studies.

I thank and acknowledge to the Consejo Nacional de Cinecia y Tecnología (CONACyT) of Mexico by the financial support recived through the grant No. 169408.

I appreciate and acknowledge Profs. Mania Pavella, Damien Ernst and Louis Wehenkel by accepting me in their research group during my Ph. D. leaving in the Université de Liegé. Their suggestions hugely improved my research work. I also would like to thank Profs. Thierry Van Cutsem and Mevludin Glavic, both of them gave me time to discuss some ideas or simply to speech about our corresponding countries, family, etc,.

Essentials for carrying out my research work were happiness, friendship and love, but overall patience, all those widely provided by my wife and sons. With care, I acknowledge and thank a lot for your special support.

Especial acknowledge to my mother, father, brother, sister and my wife’s family, by their good wishes at any moment of my Ph.D. studies.

Summarized in very few words because the list is fortunately too large; from Colima to Morelia and from Morelia to Belgium, I thank a lot to all my dear colleagues and friends who shared with me their time, experiences, knowledge, good meals, ice creams, some drinks or any similar thing.

Abstract

This research work focuses on the way of extending a conventional Newton-based Optimal Power Flow (OPF) approach to compute optimum steady state operating points under two important aspects in power systems operation. On the one hand, the conventional OPF approach is modified to consider a proposed steady state detailed model of a Voltage Source Converter-based High Voltage Direct Current (VSC-HVDC) system. The VSC-HVDC's ability to provide independent control of the converters AC voltage magnitudes and phase angles relative to the system voltage, which allows the use of separate active and reactive power control loops for system regulation, is well represented by the proposed model. This development allows computing optimum steady state equilibrium points of power systems considering the operation of VSC-HVDC devices.

On the other hand, the conventional OPF approach is modified to derive two new global Transient Stability Constrained-Optimal Power Flow (TSC-OPF) approaches. In both approaches, the SIngle Machine Equivalent (SIME) method is used to represent the multi-machine system dynamics by a corresponding One Machine Infinite Bus (OMIB) equivalent system. The multi-machine system transient stability is controlled by ensuring the transient stability of the corresponding OMIB equivalent system. Each one of the proposed TSC-OPF approaches formulates a corresponding new stability constraint in terms of the angular deviation of the OMIB equivalent rotor angle trajectory, at one specific integration time step of the interval to be considered into the TSC-OPF analysis. This formulation yields the following two main advantages: a substantial reduction of problem size and complexity related to the TSC-OPF global approaches and a non-heuristic representation of the system transient stability limits.

Clearly, these advantages are the effect of using SIME salient parameters into the proposed TSC-OPF formulation, and allow the efficient and accurate computation of steady state operating points that ensure the system transient stability under credible contingency scenarios.

The effectiveness and main characteristics of the two main aspects developed in this research work are illustrated by means of numerical examples.

Table of Contents

List of Tables

List of Figures

List of Terms

Acronyms:

OPF	:	Optimal Power Flow
VSC-HVDC	:	Votage Source Coverter-High Voltage Direct Current system
TD	:	Time-Domain analysis
TSC-OPF	:	Transient Stability Constrained-Optimal Power Flow
SIME	:	SIngle Machine Equivalent
OMIB	:	One Machine Infinite Bus equivalent system
COI	:	Center Of Inertia
IP	:	Initial steady state operating Point
CT	:	Critical stable Trajectory
UT	:	Unstable Trajectory
CCT	:	Critical Clearing Time
AC	:	Alternating Current
DC	:	Direct Current
P	:	Active power
Q	:	Reactive Power
S_{Ci}	:	Voltage source converter apparent power
DAEs	:	Differential-Algebraic Equations set
KKT	:	Karush-Kuhn-Tucker first order optimality conditions
pu	:	Per unit
s	:	Second (time)
deg.	:	Degree
rad.	:	Radian

Sub-scripts:

afic	:	Active functional inequality constraint
aicv	:	Active inequality constraint on variable
sys	:	System
*	:	Optimal point
inj	:	Injected
Ci	:	Voltage source converted connected at node *i*

Scalars:

$\boldsymbol{S}$	:	Penalty weighting factor
$\boldsymbol{c}$	:	Convexification factor
$\boldsymbol{N_g}$	:	Number of generators
$\boldsymbol{N_b}$	:	Number of buses
$\boldsymbol{N_s}$	:	Number of integration steps
υ	:	Constraint violation index
$\boldsymbol{Tol_{add}}$	:	Violation tolerance for adding constraints to the active set
$\boldsymbol{Tol_{free}}$	:	Violation tolerance for releasing constraints from the active set

$\boldsymbol{t_0}$	:	Lower integration interval
$\boldsymbol{t_{cl}}$	:	Fault clearing time
$\boldsymbol{t_{end}}$	:	Upper integration interval
$\boldsymbol{t_u}$	:	Time to instability assessed by SIME
$\boldsymbol{t_r}$	:	Time to stability assessed by SIME
$\boldsymbol{t_{ctrl}}$	:	Time step of the system dynamics at which is imposed the stability constraint

Sets:

CM	:	Set of Critical Machine(s)
NM	:	Set of Non critical Machine(s)
$NCVCS$	:	Normalized Candidate Violated Constraint Set
$NCRCS$	:	Normalized Candidate Released Constraint Set
$\boldsymbol{x_s}$	:	Set of state (dynamic) variables
$\boldsymbol{y}$	:	Set of algebraic variables
$\boldsymbol{u}$	:	Set of non-time varying system parameters
$\boldsymbol{\lambda}$	:	Vector of Lagrangian multipliers associated to equality constraints
$\boldsymbol{\mu}$	:	Vector of Lagrangian multipliers associated to inequality constraints
$\boldsymbol{P_g}$	:	Set of generated active powers
$\boldsymbol{V}$	:	Set of nodal voltage magnitudes
$\boldsymbol{\theta}$	:	Set of nodal voltage angles
$\boldsymbol{E}$	:	Set of internal voltages of the synchronous generators
$\boldsymbol{\delta}$	:	Set of angles of the rotors of the synchronous generators
$\boldsymbol{\omega}$	:	Set of speeds of the rotors of the synchronous generators

Matrices:

J	:	Jacobian matrix
W	:	Hessian matrix
H	:	Hessian sub-matrix

Functions:

$f(\bullet)$	:	Multi-variable objective function
$\mathcal{L}(\bullet)$	:	Multi-variable Lagrangian function
$\nabla\mathcal{L}(\bullet)$	:	Multi-variable Gradient function
$E(y)$	:	Quadratic penalty function

Generators:

δ	:	Generator’s rotor angle
ω	:	Generator’s rotor speed
E	:	Voltage magnitude of the internal node of the generator.
P_m	:	Mechanical input power

P_e	:	Active power delivered at the terminals of the generator
x_d'		Direct axis transient reactance
H		Coefficient of inertia

Loads:

P_L	:	Active constant power
Q_L	:	Reactive constant power
$V_i^{t_0}$	:	Nominal voltage at load node

Chapter 1

Introduction

1.1. Motivation and Justification

Engineers in the power industry are facing the complex problem of operating large and interconnected power systems. This task becomes more complicated due to the continuous demand increasing under a stressed and competitive environment, where economical along with security aspects must be integrated for power systems accurate operation. Trying of operating a power system in the most accurate way, engineers in control centers routinely execute three main computations; power flow, fault and stability analysis [Stott, 1979]. Conventional power flow analysis yields steady state operating points [Acha et al., 2004], from which contingency and stability analysis are carried out to assess the system static and dynamic security [Vittal, 2000]. However, conventional power flow analysis can not handle with the economic operation of power system, as required by the aforementioned competitive environment. In addition, contingency and stability analysis determine if the system is secure for a given contingency scenario, but do not yield recommended control actions to guarantee the system security.

The aforementioned encourage the development of more sophisticated power system operation tools able to be used in either control centers or energy management systems. By way of example, the concept of optimal power flow has received great attention since its introduction to power systems analysis. At the beginning, this analysis represented a rout toward the power system economic operation, since its formulation is given as an optimization problem with an economical objective function to be minimized under a large variety of constraints [Huneault and Galiana, 2009; Gomez-Exposito et al., 2009]. These constraints can accurately represent steady state physical and operating limits, in other words, power systems static security limits [Gomez-Exposito et al., 2009]. Therefore, the solution of an optimal power flow model yields steady state operating points that readily can satisfy static security constraints. This means that the optimal power flow formulation is flexible so to as consider not only economical aspects of power systems, but also security requirements [Momoh et al., 1997]. As consequence, in order to accurately assess optimal operating points that satisfy static security limits, the optimal power flow analysis must consider into the optimization problem the steady state mathematical models of basics elements of a power system.

Nowadays, flexible AC transmission systems (FACTS) have been worldwide installed with the concern of making more controllable the power networks [Acha et al., 2004]. In this context, high voltage DC systems are installed with the aims of transferring scheduled amounts of electric energy between power systems. The new generation of power electronics devices has given rise to innovative technologies, such as voltage source

converters (VSC)-based high voltage DC systems. In order to assess optimum steady state operating points that satisfies static security constraints whilst exploiting the capabilities of the voltage source converters (VSC)-based high voltage DC systems [Hingorani and Gyugyi, 1999], the conventional optimal power flow analysis must be upgraded to consider models of this kind of devices.

However, static aspects are not today the only challenges to optimal power flow [Momoh et al., 1997], since the stressed and competitive environment of power systems imposes the needed of fulfilling dynamic security aspects along with static security and economical issues. A main component that affects the dynamic security is the system transient stability [Kundur et al., 2004], this dynamic phenomenon is therefore of great interest in electric power systems operation and planning. Attempts of including stability constraints along with the economical operation of power systems have been developed in two main different ways; by means of global and sequential approaches [Ruiz-Vega and Pavella, 2003]. Global approaches yield optimal solutions that ensure system transient stability but suffer of the course of dimensionality, huge computational burden and robustness. Sequential approaches are robust and very efficient, but yield sub-optimal solutions that guarantee system transient stability. In other words, global approach could assess more economical solutions than sequential approaches, but might not be applied for practical operation purposes. This fact suggests that from a practical viewpoint, the compromise between economy and transient stability security requirements has not been enough fulfilled through either global or sequential approaches.

1.2. Current state of art

Complexity of planning and operating modern power systems is continually increasing because of larger power transfers over longer distances, opening of the market for delivery of cheaper energy to customers, greater interdependence among interconnected systems, more difficult coordination and complex interaction among various system controllers and less power reserves. These requirements must be addressed with the objective of planning and operating the modern electric power systems in a reliable, secure and economical way. To accomplish this objective, it is necessary to integrate the aforementioned requirements into different power system analysis tools or Energy Management Systems (EMS) functions, which allow assessing high quality control strategies that reduce the complexity of the tasks achieved by control center operators and planners [Carpentier and Bornard, 1991]. In this context, this research work aims at improving one of the main functions of the EMS; the Optimal Power Flow Analysis (OPF).

The idea of optimal power operation was first introduced by Dommel and Tinney in the early 1960's [Huneault and Galiana, 2009]. OPF is a generic term that describes a broad class of optimization problems in which a specific objective function must be optimized while satisfying operational and physical constraints of the electric network [Momoh et al., 1999a]. It must be pointed out that the objective function can be formulated in different ways to reflect the optimization of a specific aspect of the power system operation. In conventional OPF analysis the minimization of the operating cost of thermal resources is usually considered. The mathematical OPF formulation constitutes a static nonlinear optimization problem. From the power systems planning viewpoint the solution of this model yields the optimal settings for electric variables in a power network, for given values of loads and system parameters [Huneault and Galiana, 2009]. From the power system

operation and control viewpoints, an OPF solution gives an answer to adjust available controls should be adjusted in order to meet demand in the most economically manner while keeping within bounds all the constraints imposed on the system.

A great deal of optimization techniques have been employed to solve OPF problems, such as linear, nonlinear, quadratic, mixed integer programming, interior-point methods and Newton-based methods [Huneault and Galiana, 2009; Momoh et al., 1999a; Momoh et al., 1999b]. The OPF Newton algorithm has been used in several practical applications [Sun et al., 1984; Maria and Findlay, 1987; Sun et al., 1988; Hong, 1992] and in available commercial software [Gomez-Exposito et al., 2009]. For example, Newton method was the most popular for EMS applications [Alsac et al., 1990] and a commercial software product [PTI Version 30.2.1], with a global users base, has selected this method as the optimization vehicle for carrying out optimization studies of electrical power systems.

In recent years, OPF studies are being used more and more by engineers in the electric power industry for assessing steady state and recommending control actions for off-line and on-line studies, but further applications ranging from modern system planning studies to operational control are of great interest and must be investigated [Momoh et al., 1997]. In this work a Newton-based conventional OPF approach is considered to take into account the development of two important applications for modern power systems planning and operation, as described below.

1.2.1. Steady State Operation of VSC-HVDC systems

The need for more efficient power systems management, and the fast development of power electronics equipments based on new and powerful semiconductor devices, have given rise to innovative technologies, such as Voltage Source Converters (VSC)-based FACTS controllers [Hingorani and Gyugyi, 1999].

Among the VSC-based controllers commissioned and installed in several transmission systems around the world, the VSC-HVDC system, also called HVDC-Light® or HVDC-Plus®, is a recent technology which has demonstrated to be successful in enhancing the power system controllability [Asplund, 2001]. In contrast to traditional HVDC transmission, which uses phase commutated converters; HVDC links using voltage source converters can not only control active power flow but also provide an independent voltage regulation to the connected *AC* system because the surplus or deficit in reactive power can be accommodated by the VSC. The first project at Näs Head on the Southern tip of Gotland started operation in November 1999. This has been followed by several VSC-HVDC projects around the world. Examples of such installations can be found in Sweden, Australia, USA, México and Norway [Asplund, 2001].

In contrast to the healthy number of publications addressing key aspects on the performance and characteristics of the VSC-HVDC technology [Bahrman et al., 2003; ABB, 2005], very few papers have actually focused on mathematical modeling suitable for large scale power systems steady-state analysis; with references [Angeles-Camacho et al., 2003; Zhang, 2005] being a fair representation of the latter category. In these papers, the modeling approach is based on an ideal variable *AC* voltage source, where the voltage source magnitude and angle are iteratively adjusted to achieve control targets. Simplicity is a key asset of this modeling approach but a major drawback is the fact that there is no way of assessing whether or not the *DC* side voltages, as well as the amplitude modulation

index of the Pulse Width Modulation (PWM) scheme, are within limits. This is of fundamental importance because such parameters impinge directly on the *AC* voltage magnitudes required to achieve the specified control targets. To circumvent this modeling shortcoming, in this research work the VSC-HVDC model has been developed with explicit representation of the converter *AC* and *DC* voltages as a function of the PWM modulation index.

It should also be brought to attention that the work in references [Angeles-Camacho et al., 2003; Zhang, 2005] is limited to modeling and implementation of VSC-HVDC for power flow analysis. A very useful literature review of OPF algorithms incorporating FACTS controllers is given in [Abdel-Moamen and N.P. Padhy, 2003]. However, suitable VSC-HVDC models for the more challenging problem of optimal power flow (OPF) studies, using Newton approach, have not yet been reported anywhere. Therefore the developed VSC-HVDC model is implemented into an existing OPF program to carry out power system optimum steady state operating points whilst exploiting the controller capabilities.

1.2.2. Dynamic security of power systems

Modern power systems are large and complex systems whose operation should be reliable, secure, and economical [Stott et al., 1987]. On one hand, the reliability and security are the first important things that need to be considered. Security refers to the ability of the power system to withstand sudden disturbances with minimum loss of the quality of service [Kundur et al., 2004]. For proper planning and operation, this means that, after a disturbance occurs, the system survives the ensuing transient and moves into an acceptable equilibrium point where all components are operating within established limits. Analyses required to judge if the system is secure are based on both, Dynamic and Static Security Assessment studies (DSA and SSA, respectively) [Vittal, 2000].

DSA covers all aspects of power system stability, and transient stability is one of its essential components [Vittal, 2000]. If DSA determines that transient instability could take place when the power system is subjected to credible contingency scenario, control actions need to be designed and applied preventively in order to avoid a partial or complete service interruption. Among different preventive control measures, generation rescheduling has been considered to be one effective control scheme to bring a vulnerable system into a secure state under transient stability constraints [Kuo and Bose, 1995]. Though this idea is simple and intuitive, traditionally the generation dispatch that steers the system to a secure equilibrium point is sought in a heuristic way, which may produce high operating costs and possible discrimination among market players [Gan et al., 2000].

The aforementioned heuristic search of a secure steady state operating point thus affects the economical factors, which on the other hand are very important to the optimal operation of power systems. The economic operation can be readily achieved by operating the power system according to the optimal equilibrium point assessed by conventional OPF study, however this analysis does not consider security constraints and therefore yields an equilibrium point that might not guarantee the system transient stability. In this context, security and economical aspects of power system operation should not be treated as separated problems [Stott, 1979]. Bearing this in mind, and trying to reconcile the conflict between economics and dynamic security requirements in power system operation, it has been proposed to formulate the transient stability and the optimal generation dispatch

problems as an integrated mathematical optimization problem, which is referred to as transient stability-constrained optimal power flow (TSC-OPF) [Momoh et al., 1997].

In addition to a given objective function, the general TSC-OPF optimization model is composed by three main set of constraints: Steady state, dynamic state and transient stability constraints. The steady state constraints are just those considered in a conventional OPF model, so they represent the physical laws and operating limits that govern the system steady state operation. The dynamic-state equality constraints are formulated by a set of Differential-Algebraic Equations (DAEs) representing in its simple form the so-called swing equations and nodal power flow mismatch equations, and must be satisfied during the whole transient period of the system dynamics. By converting the differential equations into numerically equivalent difference (algebraic) equations, the TSC-OPF problem is formulated as an algebraic optimization problem that can be solved by conventional nonlinear optimization techniques [La Scala et al., 1998; Gan et al., 2000]. However, because of this new set of difference-algebraic equality constraints must be satisfied in every time step of the whole transient period of the dynamics, the number of constraints considered into the TSC-OPF model is extremely huge and proportional to the number of discretized intervals. Transient stability constraints ensure that the synchronous generators maintain stability in response to a specified contingency, to formulate these constrains a transient stability index must be defined.

In general, the solution of the TSC-OPF problem consists of an iterative procedure of two main steps [La Scala et al., 1998; Gan et al., 2000]. Firstly, from a given initial equilibrium point, transient stability analysis is carried out to determine if the system is stable under a set of contingencies. In case a contingency (or more) could make the system unstable, simulation results are used in order to compute a set of stability constraints. Secondly, transient stability constraints are included into the conventional optimal power flow model, which determines a new improved steady state operating condition. Stability analysis is performed again to check that the new operating condition guarantees the system transient stability. This two-step iterative process is repeated iteratively until reaching an equilibrium point which satisfies transient stability constraints.

Many researchers have been investigating the most efficient and accurate way of integrating transient stability constraints into the conventional OPF model. Up to now, based on how these dynamic and stability constraints are handled in the optimization problem, TSC-OPF approaches are classified in either sequential or global approaches [Ruiz-Vega and Pavella, 2003; Sun et al., 2004]. In the sequential category, transient stability constraints are indirectly expressed in terms of the traditional OPF constraints, and the general two main steps of the TSC-OPF approaches can be implemented by sequentially using a conventional OPF and a transient stability programs [Fouad and Jianzhong, 1993; Bettiol et al., 1999; Ruiz-Vega and Pavella, 2003; Nguyen and Pai, 2003]. Since sequential approaches use a conventional OPF formulation they are computationally efficient and can provide transparency about the salient parameters responsible for the system loss of synchronism, but the main objection is that they do not ensure finding a optimal solution [Ruiz-Vega and Pavella, 2003]. That sub-optimality is mainly associate with the fact of sequential approaches do not consider an explicit stability constraint into the optimization problem.

On the other hand, the global category focused in this research work extends the conventional OPF formulation by including additional sets of stability and dynamic

constraints [La Scala et al., 1998; Gan et al., 2000; Yuan et al., 2003; Sun et al., 2004; Hakim et al., 2009]. The optimization process minimizes a given objective function by rescheduling the available generation while satisfying both, transient stability and steady-state security constraints at the same time. The optimal equilibrium point given by the solution assures that the system would maintain stability in response to a specified contingency. Attempting to reduce the course of dimensionality and computational burden of the aforementioned global approaches, the TSC-OPF problem can be viewed as aproblem of controlling transient trajectories which are completely defined by their corresponding steady state operating point, the TSC-OPF problem can be considered as an initial value problem that can be formulated in the Euclidian space if there is not interest in the detail of transient trajectories of the state variables [Chen et al., 2001]. Based on this idea, a functional transformation technique is applied in [Chen et al., 2001; Xia and Chan, 2006] to transform the TSC-OPF problem from the functional space of time domain to the Euclidian space where the problem is completely defined by the variable values computed at the steady-state period. Hence, the transformed TSC-OPF problem has the same number of variables as those of the conventional OPF with finite number of constraints.

Despite the computational burden reduction achieved by the aforementioned global approaches, it must be pointed out that the stability index, used to indicate if whether or not the system is stable, necessarily affects the computational burden and accuracy of the TSC-OPF approaches. On the one hand, the number of dynamic and transient stability constraints to be included in the formulation is a direct function of the adopted transient stability index. On the other hand, if the selected transient stability index does not well represent the system testability limit, the computed solution by global approaches could be even less optimal (economic) than that given by a sequential approach, but requiring much more computational effort. In this context, two transient stability indexes have already been widely adopted in the TSC-OPF global formulations to assure the transient stable behavior of the power system, namely dot product [La Scala et al., 1998] and rotor angle limit [Gan et al., 2000], as described below.

a) Transient stability index based on dot product

This index is obtained from the assumption that a stable equilibrium point (SEP) is surrounded by unstable equilibrium points lying in a surface called potential energy boundary surface (PEBS) [La Scala et al., 1996]. Considering that all system trajectories crossing the PEBS are unstable whereas all stable trajectories remain inside the PEBS, it is possible to define a transient stability constraint to prevent the system trajectories crossing the PEBS, which is used as an index of system stability. The constraint is formulated as the dot product of the vector of the accelerating power of rotors and the vector of rotor angles displacements from rotors angles of the SEP at the post-disturbance dynamical period. All vectors are expressed with respect to the center of inertia (COI). Based on the fact that the dot product is negative inside the PEBS and positive outside, the stability index establishes that as long as the dot product evaluated is less than zero at each time step of the discretized trajectory, the system is stable [La Scala et al., 1998]. This stability index has been also been formulated as stability constraint in [Sun et al., 2004].

This index is completely general and it is independent of the number of machines in the system; i.e. it is only required one stability constraint for each time step of integration included in the optimization process because the PEBS criterion is referred to the whole

system but not to each machine. However, the number of dynamic plus stability constraints depends on the upper integration interval t_{end} which is selected arbitrarily. The formulation of this index into the TSC-OPF problem is more complicated than the rotor angle index due to the computation of the derivative in the optimization process. Lastly, a-power flow-alike algorithm is employed at the beginning of each iteration of the optimization process to evaluate the post-contingency stable operating point used in the computation of the dot product [La Scala et al., 1998].

b) Transient stability index based on rotor angle limit

This index is directly obtained from the observation of time domain simulations by considering that rotor angles of unstable machines move away from the COI and eventually loss synchronism, whereas rotor angles of stable machines move coherently with respect to the COI and oscillate within a certain boundary. Hence, the transient stability constraint is formulated such as the deviation of rotor angles with respect to COI must be within certain limit for each time step of the entire integration period *T*. This limit corresponds to the index for identifying transient instability [Gan et al., 2000].

The actual value of this index is not easy to establish because its variation with different systems and operating conditions; therefore, this problem has been solved by adopting a fixed value heuristically during the whole optimization process. By way of example, the maximum allowable deviation of rotor angles w.r.t. COI is of 100° in [Gan et al., 2000; Yuan et al., 2003; Layden and Jeyasurya, 2004], whilst values of 120° and 144° have been used in [Xia and Chan, 2006] and [Chen et al., 2001], respectively. The lack of a generic method to select an appropriate value to the index can produce a very conservative transiently stable optimal operating point if index is set to a low value. On the other hand, if the threshold is too relaxed, the operating point can be transiently unstable even if the limit has not been exceeded in the period span considered in the TSC-OPF problem.

Lastly, independently of the value given to the stability index, the number of stability constrains to be included into the TSC-OPF is equal to the number of generators times the number of the integration steps considered in the optimization process. But the dimensionality burden increases due to the fact that the integration period to be considered into the TSC-OPF problem is also heuristically selected, thus the number of transient stability plus dynamic constraints might substantially increase.

Real-world power systems are operated such that any generator rotor angle w.r.t. COI will not be greater than a specified threshold, which has a value of 180 degrees in extreme cases [Sauer and Pai, 1998]. Hence the index based on the rotor angle limit has been widely adopted for utility engineers for determination of transient stability [Gan et al., 2000]. Based on this fact and previous discussions, this research work aims on improving not only the course of dimensionality and computational efficiency of TSC-OPF global approaches using the rotor angle limit index, but also the accuracy and transparency about the salient parameters responsible for the system loss of synchronism. This goal is achieved by reducing the multi-machine system angle trajectories to a Single One Infinite Bus (OMIB) equivalent angle trajectory by applying the SIME approach [Pavella et al., 2000], from which a new stability index is proposed as described below.

c) Transient stability index based on OMIB rotor angle limit

Based on the equivalent model, it is possible to compute a transiently stable optimal equilibrium point by stabilizing the OMIB single rotor angle trajectory, representing the whole system rotors angle dynamics, instead of stabilizing the whole set of individual machine angle trajectories. The limit imposed on the angular deviation of the single equivalent machine to ensure transient stability can be calculated off-line through SIME approach, so that it is not selected heuristically. This idea is investigated in this research work and also in [Zárate-Miñano et al., 2010], but having quite different stabilization procedures and advantages w.r.t. those approaches based on the dot product and the rotor angle limit.

In this thesis the new proposed stability index based on OMIB rotor angle limit is used in two different ways, such that two general, non-heuristic, accurate and efficient transient stability preventive control approaches are investigated. The theoretical basis, detailed characteristics and main advantages of the proposed transient stability preventive control approaches are discussed in this document.

1.3. Objectives

This research work focuses the way of extending a conventional Newton-based Optimal Power Flow (OPF) approach to compute optimum steady state operating points under two important aspects in power systems operation. The first aspect considers the steady state operation of a VSC-HVDC system, such that a detailed mathematical model of this device must be developed and included into the conventional OPF analysis.

The second issue is related to the accurate and efficient determination of optimum steady state operating points where the system transient stability is preventively ensured for a credible contingency scenario. To accomplish this task, the SIME method must be considered to reduce the problem size and complexity associated to global transient stability constrained-optimal power flow approaches.

1.4. Methodology

In order to accomplish with the proposed objectives, this research work was developed according to the following methodology,

a) *Computation of steady state optimum operating points considering VSC-HVDC systems*
   - Review of the state of the art of VSC-HVDC systems
   - Development of the VSC-HVDC steady state detailed model
   - Computational implementation of the VSC-HVDC model
   - Development of case studies

b) *Computation of transiently stable steady state operating optimum operating points*
   - Review of the state of the art of preventive transient stability control global and sequential approaches
   - Computational implementation of the TD program
   - Computational implementation of SIME method

- Results validation
- Development of transient stability control Approach I
- Development of transient stability constraint for Approach I
- Computational implementation of Approach I
- Approach I results validation
- Development of transient stability control Approach II
- Development of transient stability constraint for Approach II
- Computational implementation of Approach II
- Approach II results validation

1.5. Primary Contributions

The main contributions of this research work are summarized below.

1. A detailed steady state model of a VSC-HVDC system suitable for OPF studies has been developed. The model has been also implemented into an existing C++ code for large scale Newton based-OPF program [Ambriz-Pérez, 1998].
2. Two novel SIME-based transient stability constrained OPF for the transient stabilization of multi-machine power systems is proposed in this thesis. The most important aspect of the new proposed approach is the significant reduction of the computational burden of global OPF-based approaches.
3. The first proposed approach allows reducing the computational burden of extended (global) OPF-based approaches in both important aspects: 1) The size of the set of dynamic constraints. The length of the time domain simulation that should be discretized and included into the extended OPF formulation (hence the size of the set of dynamic constraints) is limited to the time to instability tu determined by SIME, and is thus no longer arbitrary or unnecessarily large. 2) The size of the set of stability constraints. Using SIME, the proposed transient stability constraint is formulated for one machine equivalent trajectory at a single integration time step, making the dimension of the TSC-OPF problem well-defined, and reducing the dimension of the set of stability constraints with respect to other approaches by Ng times the number of time integration steps. Furthermore, as the stability constraint is formulated with respect to a critical trajectory of the OMIB rotor angle, power system operation is not limited with respect to a fixed value, but to a sound physically-based value that is adjusted to the actual system dynamics. The proposed approach's capability to control transient stability has been successfully illustrated by numerical examples.
4. In the second proposed approach, the global TSC-OPF formulation only requires considering a single stability constraint applied at the initial system operating point, replacing the (usually large) sets of dynamic and transient stability constraints required by other TSC-OPF formulations. This is because the optimization process is performed in the Euclidian space, such that is not necessary to add either dynamic constraints or transient stability constraints in the TSC-OPF formulation to stabilize a specified fault scenario.

1.6. Publications

The publications derived from this research work are given as follows.

Journal papers

1. A. Pizano-Martínez, C.R. Fuerte-Esquivel, H. Ambriz-Peréz, and E. Acha, "Modeling of VSC- based HVDC systems for a Newton-Raphson OPF Algorithm," *IEEE Trans. on Power Syst.*, ISSN 0885-8950, Vol. 22, No.4, pp.1794-1803, Nov., 2007.
2. A. Pizano-Martínez, C.R. Fuerte-Esquivel, and D. Ruiz-Vega, "Global transient stability-constrained optimal power flow using an OMIB reference trajectory," *IEEE Trans. on Power Syst.*, ISSN 0885-8950, Vol.25, No.1, pp 392-403, Feb., 2010.

Conference papers

3. Pizano-Martínez A., Fuerte-Esquivel C.R., and Ruiz-Vega D., "Global Transient Stability-Constrained Optimal Power Flow using the SIME Method," *IEEE-PES General Meeting*, ISSN 1944-9925, 26-30, July, 2009, Calgary, Canada, 8 pages.
4. Pizano-Martínez A., Fuerte-Esquivel C.R., and Ruiz-Vega D., "Global Transient Stability-Constrained Optimal Power Flow using SIME Sensitivity analysis," *IEEE-PES General Meeting*, 2010.

Submitted journal papers

5. Gutierrez-Martinez V.J., Cañizares C.A., Fuerte-Esquivel C.R., Pizano-Martínez A., and Gu X., "Neural-network security-boundary constrained optimal power flow," *Transactions on Power Systems*, 2010.

1.7. Cites to papers

Cited Paper:

A. Pizano-Martínez, C.R. Fuerte-Esquivel, H. Ambriz-Peréz, and E. Acha, "Modeling of VSC- based HVDC systems for a Newton-Raphson OPF Algorithm," *IEEE Trans. on Power Syst.*, ISSN 0885-8950, Vol. 22, No.4, pp.1794-1803, Nov., 2007.

Cited by:

1. A. Lotfjou and M. Shahidehpour, "Security-Constrained Unit Commitment with AC/DC Transmission Systems," *IEEE Trans. on Power Syst.*, ISSN 0885-8950, Vol. 25, No.1, pp.531-543, Feb., 2010.

2. Q.- Y. Jiang, and G.-C. Geng, "Interior-point optimal power flow with the high voltage direct current transmission system," *Zhongguo Dianji Gongcheng Xuebao/Proceedings of the Chinese Society of Electrical Engineering*, Vol.29, No. 25, 2009, pp. 43-49.

3. J. Hazra, Y. Phulpin, and D. Ernst, " HVDC Control Strategies to Improve Transient Stability in Interconnected Power Systems," *IEEE Bucharest Power Tech*

Conference (Power Tech 2009), June 28-July 2 2009, Bucharest, Romania, pp 1-6.

4. W. Liu, and Z. Cai, "Model analysis and robust control design of VSC-HVDC converter with dq0 axis," *3rd International Conference on Deregulation and Restructuring and Power Technologies, DRPT 2008*, paper. no. 4523697, pp. 1792-1796, 2008.
5. R.K. Varma, W. Litzenberger, J. Bolton, N.R. Chaudhuri, and S. Auddy, "Bibliography of HVDC Transmission: 2006–2007 IEEE Working Group Report." *IEEE Power and Energy Society General Meeting - Conversion and Delivery of Electrical Energy in the 21st Century 2008*, July 20-24 2008, Pittsburgh, Pennsylvania, USA, pp 1–7.

1.8. Organization of the thesis

This thesis is organized as follows,

In Chapter 2, the theoretical bases of the conventional OPF analysis are presented. The OPF problem is firstly formulated as a general nonlinear programming problem, subjected to equality and inequality constraints. In order to solve this constrained problem, the Lagrangian function is assembled to convert the problem into a nonlinear unconstrained optimization problem. The Karush-Kuhn-Tucker (KKT) first order optimality conditions are applied to the Lagrangian function, resulting in a nonlinear algebraic equation set. The solution of this nonlinear algebraic set is then solved by mean the Newton method, where the inequality constraints are handled by means of quadratic penalty functions and the Lagrange multipliers method. The Newton based-OPF algorithm is presented.

The Chapter 3 gives in detail the derivation of the model of a VSC-HVDC system suitable for conventional OPF solutions using Newton algorithm. The VSC-HVDC's ability to provide independent control of the converters AC voltage magnitudes and phase angles relative to the system voltage, which allows the use of separate active and reactive power control loops for system regulation, is well represented by the model. In this new development in Newton OPF, the VSC-HVDC system equations are incorporated directly into the Lagrangian function, Hessian matrix and gradient vector of whole system for a unified optimal solution in a single frame-of-reference. The effectiveness of the VSC-HVDC model and its proposed implementation in a Newton-based OPF existing program [Ambriz-Pérez, 1998] is demonstrated by means of two sample systems.

In Chapter 4 the theoretical bases for transient stability assessment and preventive control through a generic global approach are presented. To investigate the system transient stability of the power system the TD analysis is formulated according to the Simultaneous Implicit model. To accomplish with this model, the system transient dynamics are mathematically modeled by the classical model of the generator and the structure preserving model of the network, which is described by a set of differenetial-alegebraic equations DAE. The DAE set is transformed into difference algebraic equations by applying the implicit trapezoidal rule, resulting in a set of non linear algebraic equations that can be readily solved by means of Newton method.

The general formulation of the TSC-OPF problem is presented in terms of steady state, dynamic state and stability constraints. Steady state constraints are those

corresponding to the conventional OPF, whilst the dynamic constraints are the difference algebraic equations set, which results of applying the trapezoidal rule to the DAE set that describes the power system dynamics. In this generic TSC-OPF model, the transient stability constraints are formulated according with the stability index based on the rotor angle limit. The general TSC-OPF algorithm is presented in order to fix the basis of the proposed stability control approaches.

The Chapter 5 deals with the SIME method and the proposed transient stability preventive control approaches. Based on the assumption that the mechanism of loss of synchronism in a power system originates from the irrevocable separation of its machines into two groups, the SIME SIngle Machine Equivalent (SIME) method reduces the trajectories of a multi-machine system to a trajectory of a One Machine Infinite Bus (OMIB) equivalent. This reduced model makes easy to carry out the transient stability preventive control because it is only necessary to stabilize one single trajectory, which represents the whole system, instead of each machine trajectory. Based on this idea, it is proposed to take advantage of the OMIB equivalent derived by SIME to carry out the transient stabilization process by a global TSC-OPF approach.

Chapter 6 presents the general conclusion of this research work and discusses related areas that require further investigation.

Chapter 2

Optimal Power Flow

In this chapter the theoretical bases of the conventional OPF analysis are presented. The OPF problem is firstly formulated as a general nonlinear programming problem, subjected to equality and inequality constraints. In order to solve this constrained problem, the Lagrangian function is assembled to convert the problem into a nonlinear unconstrained optimization problem. The Karush-Kuhn-Tucker (KKT) first order optimality conditions are applied to the Lagrangian function, resulting in a nonlinear algebraic equation set. The solution of this nonlinear algebraic set is then solved through the Newton method, where the inequality constraints are handled by means of quadratic penalty functions and the Lagrange multipliers method. The Newton based-OPF algorithm is presented.

2.1. General formulation

Since its early stages the OPF problem has been a very interesting and active research area of electric power systems [Huneault and Galiana, 2009; Momoh et al., 1999a]. Different methods have been proposed for efficiently solving the OPF problem, their differences mainly depend on the objective considered to be optimized and the search algorithm used in the optimization process [Huneault and Galiana, 2009; Momoh et al., 1999a]. Despite the large variety of OPF methods, the conventional OPF problem is stated as the following constrained nonlinear optimization general mathematical model [Bertsekas, 1998],

$$\text{Minimize} \quad f(\boldsymbol{y}) \tag{2.1}$$

$$\text{Subject to} \quad \boldsymbol{h}(\boldsymbol{y}) = \mathbf{0}; \tag{2.2}$$

$$\boldsymbol{g}(\boldsymbol{y}) \geq \mathbf{0} \tag{2.3}$$

$$\underline{\boldsymbol{y}} \leq \boldsymbol{y} \leq \overline{\boldsymbol{y}} \tag{2.4}$$

where the mapping $f(\boldsymbol{y}):\Re^q \to \Re$ is the objective function to be minimized. $\boldsymbol{h}(\boldsymbol{y}):\Re^q \to \Re^n$ is a set of equality constraint functions corresponding to both power flow mismatch equations and control equations. $\boldsymbol{g}(\boldsymbol{y}):\Re^q \to \Re^m$ is a set of inequality constraint functions which prevent the violation of system operating and physical limits. The vector of system variables $\boldsymbol{y} \in S \subseteq \Re^q$, includes the dependent steady state variables $\boldsymbol{x} \in \Re^{sv}$ and control variables $\boldsymbol{u} \in \Re^{cv}$ (see §2.1.1), with lower and upper limits represented by $\underline{\boldsymbol{y}}$ and $\overline{\boldsymbol{y}}$, respectively.

A point $\boldsymbol{y}$ in the search space S that satisfies the set of equality and inequality constraints is defined as a feasible point $\boldsymbol{y}_F$, the infinite set of feasible points defines the feasible region F. Additionally, a feasible point $\boldsymbol{y}_F$ is said to be an optimum point $\boldsymbol{y}^*$ if the

evaluation of the objective function at points $\boldsymbol{y}^*$ and $\boldsymbol{y}_F$ of F satisfies $f(\boldsymbol{y}^*) \leq f(\boldsymbol{y}_F)$. The active set of inequality constraints consists of those variables and functions explicitly enforced to specified values in a particular feasible solution. The set of inequality constraints that must be active at the optimum solution $\boldsymbol{y}^*$ is called the binding set. All equality constraints are regarded as active at any feasible point since they must be satisfied unconditionally at the solution of (2.1)-(2.4).

2.1.1. Classification of variables

The solution of (2.1)-(2.4) involves the computation in a single unified reference frame of a large set of system variables $\boldsymbol{y}$ and constraint variables $\boldsymbol{c} \in \Re^{n+m}$. For the purpose of efficiently implementing an OPF algorithm, all variables to be considered in the optimization model can be classified into the categories described below.

The set of control variables $\boldsymbol{u} \subset \boldsymbol{y}$ represent the quantities that can be adjusted within limits by the algorithm to achieve the minimization of the objective function. Variables of this kind represent the active power output of generators, transformer tap ratios, transformer phase shift angles and voltage magnitudes at all nodes with reactive power compensation [Sun et al., 1984; Sun et al., 1988].

The dependent steady state variables $\boldsymbol{x} \subset \boldsymbol{y}$ represent the quantities of the system that are achieved as consequence of the tuning of the control variables. Equal to the control variables, the dependent variables are set at any value within their limits by the optimization process to perform an OPF solution. Examples of those variables are the reactive power at all generation nodes, active power generation cost, active and reactive power flows in the network elements, the network voltage profile represented by magnitude and phase angle of all nodes, except the voltage magnitude at nodes with reactive compensation, and the phase angle of the slack node. This phase angle is fixed at zero to be considered as the reference of any system variable representing an angular quantity.

The set of constraint variables $\boldsymbol{c}$ includes the subset $\boldsymbol{\lambda} \in \Re^n$ and $\boldsymbol{\mu} \in \Re^m$, where the vector of variables $\boldsymbol{\lambda} \in \Re^n$ is related to equality constraints (2.2), whilst the vector of variables $\boldsymbol{\mu} \in \Re^m$ is associated to inequality constraints (2.3) and (2.4). Both subsets are classified as auxiliary variables and represent the Lagrangian Multipliers (see §2.2.1).

For the computational implementation of an OPF algorithm it is also necessary to consider a set of parameters that are not variables during the optimization process, but are required to perform the problem solution. Examples of such parameters are the power system topology, electric power demand, electric characteristics of the network and devices of the power system, etc.

2.1.2. Objective function

Conventional OPF studies can consider a large variety of objectives to be optimized, the one most studied is the total generation cost [Huneault and Galiana, 2009] and it is considered in this research work. The generation cost $C_i\,(\$/hr)$ at thermal unit i can be represented by the following non-linear second order model [Sun et al., 1984; Wollenberg and Wood, 1984],

$$C_i(P_{Gi}) = a_i + b_i P_{Gi} + c_i P_{Gi}^2 \tag{2.5}$$

where the variable P_{Gi} (MW) is the active power generated at unit i. The parameters a_i, b_i and c_i are the cost curve coefficients. Based on (2.5) the model that represents the total system generation cost can be readily represented as,

$$f(\boldsymbol{y}) = \sum_{i}^{N_g} C(P_{Gi}) \tag{2.6}$$

where N_g is the number of generator in the power system to be included in the dispatch. At difference with the conventional power flow studies, the generator connected at slack node must be considered in the formulation (2.6) [Lee et al., 2010], otherwise the minimization algorithm will dispatch at its maximum capacity this generator while dispatching all the remaining units at their minimum capacity. This fact might not be practical because could produce transmission lines overloading, and even could yield algorithm convergence problems.

2.1.3. Equality constraints

The set of equality constraints $\boldsymbol{h}(\boldsymbol{y})$ of the OPF model describe the laws that are governing the physics of the power system and, as already mentioned, they must be satisfied unconditionally at the optimal solution. The equality constraints are typically associated to the nodal power mismatch equations, and provide a means to achieve the active and reactive power balance in every node of the whole network during steady state operation.

The set of power mismatch equations states that the power generation must satisfy the active and reactive power demand plus network losses,

$$P_i^{inj}(\boldsymbol{V}, \boldsymbol{\theta}) + P_{Li} - P_{Gi} = 0 \tag{2.7}$$

$$Q_i^{inj}(\boldsymbol{V}, \boldsymbol{\theta}) + Q_{Li} - Q_{Gi} = 0 \tag{2.8}$$

where P_{Li} and Q_{Li} are the active and reactive power loads at node i, respectively. P_{Gi} and Q_{Gi} are the active and reactive power generations at node i, respectively. P_i^{inj} and Q_i^{inj} are the active and reactive power injections at node *i*, respectively. It must be pointed out that constraints (2.7) and (2.8) have nonlinear terms, which are function of system variables that represent the network nodal voltage magnitudes $\boldsymbol{V}$ and phase angles $\boldsymbol{\theta}$. Consequentially, equality constraints can relate control variables $\boldsymbol{u}$ and dependent steady state variables $\boldsymbol{x}$.

Among other applications, equality constraints can also be used to set the value of a control or dependent state variable at some predefined set point, for example, setting the complex power flow through a transmission line at some specified value. These kinds of applications are presented with more detail further in the document.

2.1.4. Inequality constraints

The set of inequality constraints considered in an OPF model can be classified in different categories as functional and variable inequality constraints [Acha et al., 2004]. The functional inequality constraints represent the bounds of functions that depend on control and dependent variables, such as the bounds on the reactive output power of a controllable

source. On the other hand, the variable inequality constraints are useful to represent the bounds of one variable, such as active output power of the generators.

The most common functional inequality constraints considered in OPF studies are,

- Lower $Q_{Gi}^{\min}$ and upper $Q_{Gi}^{\max}$ bounds on the reactive output power Q_{Gi} of the generators,

$$Q_{Gi}^{\min} \leq Q_{Gi} \leq Q_{Gi}^{\max} \quad i=1,\ldots,N_g \tag{2.9}$$

- where N_g is the number of generation nodes and Q_{Gi} is computed from (2.8), as follows,

$$Q_{Gi} = Q_i^{inj}(\boldsymbol{V},\boldsymbol{\theta}) + Q_{Di} \tag{2.10}$$

- Upper bound $F_{km}^{\max}$ on the active power flow F_{km} in the transmission line connecting node *k* and *m*,

$$\left|F_{km\,i}(\boldsymbol{V},\boldsymbol{\theta})\right| < F_{km\,i}^{\max} \quad i=1,\ldots,N_{Lc} \tag{2.11}$$

  where N_{Lc} is the number of transmission lines with constrained active power flow. The active power flow in the line is assessed through of the nonlinear term $F_{km}(\boldsymbol{V},\boldsymbol{\theta})$, which is a function of the complex voltages at nodes *k* and *m*.

The most common variable inequality constraints considered in OPF studies are,

- Lower $P_{Gi}^{\min}$ and upper $P_{Gi}^{\max}$ bounds on the active output power P_{Gi} of the generators,

$$P_{Gi}^{\min} \leq P_{Gi} \leq P_{Gi}^{\max} \quad i=1,\ldots,N_g \tag{2.12}$$

- Lower $V_i^{\min}$ and upper $V_i^{\max}$ limits on nodal voltage magnitudes V,

$$V_i^{\min} \leq V_i \leq V_i^{\max} \quad i=1,\ldots,N_b \tag{2.13}$$

  where N_b is the number of node of the system and N_g is the number of generation nodes.

2.2. Application of Newton method for computing OPF solutions

The Newton method is a powerful solution algorithm of nonlinear equations; this is because of its quadratic convergence characteristic near the solution. In electrical engineering, this method is widely used to solve the power flow analysis, which is commonly modeled by a set of nonlinear equations whose initial conditions are well defined near the solution.

The OPF research can be characterized as the application of increasingly powerful optimization tools [Huneault and Galiana, 2009]. Some of these optimization tools have been developed based on the Newton method, so they are classified as Newton-Based category [Momoh et al., 1999b]. To solve the OPF problem through the Newton method, it is necessary to construct a Lagrangian function $\mathcal{L}(\boldsymbol{y},\boldsymbol{\lambda},\boldsymbol{\mu})$ that converts the constrained nonlinear OPF problem into a nonlinear unconstrained problem. The function $\mathcal{L}(\boldsymbol{y},\boldsymbol{\lambda},\boldsymbol{\mu})$ is written in terms of the Karush-Kuhn-Tucker (KKT) first order optimality conditions [Luenberger, 1984; Nocedal and Wright, 1999], which results in a set of nonlinear

equations. The Newton method is then applied to solve this set of nonlinear equations, as in the conventional power flow analysis.

It must be pointed out that, due to the fact $\mathcal{L}(\boldsymbol{y},\boldsymbol{\lambda},\boldsymbol{\mu})$ is constructed with terms associated with inequality constraints, its composition suffers *k* changes, according to the active set updating, until reaching the binding set. This means the Lagrangian function is *k* times rewritten according to the KKT conditions, and therefore the Newton method must be sequentially applied to solve *k* different set of nonlinear systems. The *k-th* nonlinear system corresponds to the binding set and its solution yields the steady state operating point that minimizes the objective function and satisfies the whole set of equality and inequality constraints.

2.2.1. Lagrangian function

The solution of (2.1)-(2.4) by the Newton approach requires the creation of a Lagrangian function where equality and inequality constraints on variables are handled by means of the Lagrange multiplier method [Bertsekas, 1996]. In this method, inequality constraints on functions are handled by penalty functions which are added to the objective function to obtain an augmented Lagrangian function. Furthermore, in order to ensure that this function becomes convex in the neighborhood of a feasible solution, convexification terms are added to the system variables [Bertsekas, 1979]. The augmented Lagrange function is,

$$\mathcal{L}_{sys}(\boldsymbol{y},\boldsymbol{\lambda},\boldsymbol{\mu}) = f(\boldsymbol{y}) + \boldsymbol{\lambda}^t \boldsymbol{h}(\boldsymbol{y}) + \psi(\boldsymbol{g}(\boldsymbol{y}), \boldsymbol{\mu}^{afic}) + \psi(\boldsymbol{y}, \boldsymbol{\mu}^{aicv}) + \boldsymbol{C_c}^t (\boldsymbol{y} - \boldsymbol{y}_r)^2 \qquad (2.14)$$

where $\psi(\boldsymbol{g}(\boldsymbol{y}), \boldsymbol{\mu}^{afic})$ and $\psi(\boldsymbol{y}, \boldsymbol{\mu}^{aicv})$ are penalty functions for the i^{th} active functional inequality constraint (*afic*) and i^{th} active inequality constraint on variables (*aicv*); respectively. $\boldsymbol{\lambda} \in \Re^n$ and $\boldsymbol{\mu} \in \Re^{afic+aicv}$ are vectors of Lagrange multipliers. $\boldsymbol{C_c}$ is a vector of penalty parameters, and $\boldsymbol{y_r}$ is a vector of reference system variables.

2.2.2. Optimality conditions for Newton method

According to the optimization theory, the optimal solution of the OPF optimization model must satisfy the following KKT first order necessary optimality conditions [Luenberger, 1984; Nocedal and Wright, 1999],

$$\nabla_y \mathcal{L}_{sys}(\boldsymbol{y}^*,\boldsymbol{\lambda}^*,\boldsymbol{\mu}^*)=0 \qquad (2.15)$$

$$\nabla_{\boldsymbol{\lambda}} \mathcal{L}_{sys}(\boldsymbol{y}^*,\boldsymbol{\lambda}^*,\boldsymbol{\mu}^*)=0 \qquad (2.16)$$

$$\boldsymbol{\mu}^{*afic} > 0, \text{ if } g(\boldsymbol{y}) = 0 \qquad (2.17)$$

$$\boldsymbol{\mu}^{*aicv} > 0, \text{ if } \boldsymbol{y}-\overline{\boldsymbol{y}}=0 \qquad (2.18)$$

$$\boldsymbol{\mu}^{*aicv} < 0, \text{ if } \boldsymbol{y}-\underline{\boldsymbol{y}}=0 \qquad (2.19)$$

$$\boldsymbol{\mu}^*=0, \boldsymbol{\mu} \notin \Re^{aicv+afic} \qquad (2.20)$$

where the vector $\boldsymbol{z}=[\boldsymbol{y}^*,\boldsymbol{\lambda}^*,\boldsymbol{\mu}^*]$ defines the optimal solution, the last four constraints are called complementary conditions. Therefore according to the KKT conditions, the optimal solution of the OPF model (2.1)-(2.4) can be found by solving,

$$\nabla_z \mathcal{L}(\boldsymbol{z})=0 \qquad (2.21)$$

In OPF studies the gradient of the Lagrangian function (2.21) is a set of nonlinear equations, which can be solved through the Newton method.

2.2.3. Linearized set of equations

The OPF solution by Newton method requires the linearization of the nonlinear system (2.21), obtained from the application of the KKT conditions to (2.14). For the sake of illustration, in this section the linearized set of equations is derived from the Lagrangian function (2.22), which is constructed based on power balance equality,

$$\mathcal{L}_{sys}(\boldsymbol{y},\boldsymbol{\lambda})=F_T+\sum_{i=1}^{N_b}\lambda_{pi}(P_i^{inj}(V,\theta)+P_{Li}-P_{Gi})+\sum_{i=1}^{N_b}\lambda_{qi}(Q_i^{inj}(V,\theta)+Q_{Li}-Q_{Gi}) \tag{2.22}$$

where N_b is the number of buses of the system. F_T is the objective function described by (2.6). λ_{pi} and λ_{qi} are the Lagrange multipliers for active and reactive power equations, respectively. The summations are taken over all the nodes, except those where the reactive power injected by generators is within limits. In (2.22) the term associated to each inequality constraint is not considered, but its formulation into the OPF analysis by Newton method is given in sections 2.2.4 and 2.2.5.

According with Newton method, the linearized system is as follows,

$$\boldsymbol{W}\Delta\boldsymbol{z}=-\nabla\mathcal{L}_{sys}(\bullet) \tag{2.23}$$

This equation (2.21) can be written as,

$$\begin{bmatrix}\boldsymbol{W}\end{bmatrix}\begin{bmatrix}\Delta\boldsymbol{y}\\ \Delta\boldsymbol{\lambda}\end{bmatrix}=-\begin{bmatrix}\nabla_{\boldsymbol{y}}\mathcal{L}_{sys}(\bullet)\\ \nabla_{\boldsymbol{\lambda}}\mathcal{L}_{sys}(\bullet)\end{bmatrix} \tag{2.24}$$

where

$$\boldsymbol{W}=\begin{bmatrix}\boldsymbol{H} & \boldsymbol{J}^{tr}\\ \boldsymbol{J} & \boldsymbol{0}\end{bmatrix} \tag{2.25}$$

$$\nabla_{\boldsymbol{y}}\mathcal{L}_{sys}(\bullet)=\begin{bmatrix}\dfrac{\partial\mathcal{L}_{sys}(\bullet)}{\partial\boldsymbol{P_G}}, & \dfrac{\partial\mathcal{L}_{sys}(\bullet)}{\partial\boldsymbol{\theta}}, & \dfrac{\mathcal{L}_{sys}(\bullet)}{\partial\boldsymbol{V}}\end{bmatrix}^{tr} \tag{2.26}$$

$$\nabla_{\boldsymbol{\lambda}}\mathcal{L}_{sys}(\bullet)=\begin{bmatrix}\dfrac{\partial\mathcal{L}_{sys}(\bullet)}{\boldsymbol{\lambda}_p}, & \dfrac{\partial\mathcal{L}_{sys}(\bullet)}{\boldsymbol{\lambda}_q}\end{bmatrix}^{tr} \tag{2.27}$$

$$\Delta\boldsymbol{y}=\begin{bmatrix}\Delta\boldsymbol{P_G} & \Delta\boldsymbol{\theta} & \Delta\boldsymbol{V}\end{bmatrix}^{tr} \tag{2.28}$$

$$\Delta\boldsymbol{\lambda}=\begin{bmatrix}\Delta\boldsymbol{\lambda}_p & \Delta\boldsymbol{\lambda}_q\end{bmatrix}^{tr} \tag{2.29}$$

where the superscript *tr* denotes transposition. Partial derivatives are used to assemble the Hessian matrix $\boldsymbol{W}$. Matrix $\boldsymbol{W}$ contains the second partial derivatives of the Lagrangian function $\mathcal{L}_{sys}(\bullet)$ with respect to the state variables $\boldsymbol{y}$ and Lagrange multipliers $\boldsymbol{\lambda}$, as follows,

$$\boldsymbol{H}=\frac{\partial^2\mathcal{L}_{sys}(\bullet)}{\partial\boldsymbol{y}^2}=\frac{\partial^2 f(\boldsymbol{y})}{\partial\boldsymbol{y}^2}+\left(\frac{\partial^2 h(\boldsymbol{y})}{\partial\boldsymbol{y}^2}\right)^{tr}\boldsymbol{\lambda} \tag{2.30}$$

$$\boldsymbol{J}=\frac{\partial^2 \mathcal{L}_{sys}(\bullet)}{\partial \boldsymbol{y}\partial \boldsymbol{\lambda}}=\frac{\partial h(\boldsymbol{y})}{\partial \boldsymbol{y}} \tag{2.31}$$

Matrix $\boldsymbol{W}$ is symmetric and has a null matrix at its lower right hand corner because the second partial derivatives of the form $\partial^2 \mathcal{L}_{sys}(\bullet)/\partial\lambda_i\partial\lambda_j$ do not exist. First partial derivatives of the gradient vector $\nabla \mathcal{L}_{sys}(\bullet)$ yield the second partial derivatives of the Lagrangian function $\mathcal{L}_{sys}(\bullet)$. $\Delta\boldsymbol{z}$ is the vector of correction terms. The steady state variables are the active power generations, the nodal voltage magnitudes and angles, $\boldsymbol{P_g}$, $\boldsymbol{V}$ and θ, respectively. Lagrange multipliers are the incremental costs for active and reactive powers, λ_p and λ_q, respectively [Acha et al., 2004].

2.2.4. Handling of inequality constraints on variables

The selection of inequality constraints to be enforced is carried out in two steps [Sun et al., 1988]: i) The candidate constraints for enforcement are identified; ii) from the candidate set, those constraints that are to be added to the active set are identified.

A constraint is considered to be a candidate if it is not already part of the active set, and following its updating according to (2.23), one of its limits is violated.

The criterion to enforce a candidate constraint is based on the relative severity of its limits violation. In order to have consistency in their relative ranking, candidate constraints are grouped in different sets according to the kind of variables they are, e.g. voltage magnitudes, active powers, reactive powers. The controller's variables and its inequality control specifications are grouped as follows: (i) magnitudes of the voltage sources representing the controller and the set of *AC* voltage magnitude inequalities are grouped together with the nodal voltage magnitudes of the entire network; (ii) the active (reactive) power to be controlled within limits is grouped with the active (reactive) power transmission lines limits. For each candidate constraint y_i of a given set, a violation index is defined by [Crisan and M. Mohtadi, 1992],

$$\upsilon_i^k = \frac{y_i^k - \text{violated limit}}{\Delta y_i^k} \qquad i=1,\cdots,m_\upsilon \tag{2.32}$$

where k indicates the main iteration number. The relative severity of limit violations is obtained by defining the normalized candidate violated constraint set (*NCVCS)* as follows [Crisan and M. Mohtadi, 1992],

$$NCVCS = \frac{\left(\upsilon_1^k,\cdots,\upsilon_{m_\upsilon}^k\right)}{\max\left(\upsilon_1^k,\cdots,\upsilon_{m_\upsilon}^k\right)} \tag{2.33}$$

Candidate constraints that will be added to the active set are those corresponding to the elements of *NCVCS* which are equal to or larger than a specified tolerance TOL_{add}. A value of TOL_{add}=0.7 was found to be a good compromise between the selection of active constraints and algorithm performance [Acha et al., 2004].

Once inequality constraints to be added to the active set have been selected, they are included into $\mathcal{L}(\bullet)$ using the following generic form of function $\psi_i(y_i^k, \mu_i^{k-1})$ [Bertsekas, 1996]:

$$\psi_i(y_i^k,\mu_i^{k-1})=\begin{cases}\mu_i^{k-1}(y_i^k-\overline{y}_i)+\dfrac{c^{k-1}}{2}(y_i^k-\overline{y}_i)^2 & \text{if } \mu_i^{k-1}+(y_i^k-\overline{y}_i)\geq 0\\ \mu_i^{k-1}(y_i^k-\underline{y}_i)+\dfrac{c^{k-1}}{2}(y_i^k-\underline{y}_i)^2 & \text{if } \mu_i^{k-1}+(y_i^k-\underline{y}_i)\leq 0\\ 0 & \text{otherwise}\end{cases} \tag{2.34}$$

In order to consider the activated inequality constraint in (2.22), the first and second derivatives of $\psi_i(y_i^k, \mu_i^{k-1})$ with respect to y are added to $\nabla\mathcal{L}_{sys}(\bullet)$ and the $\boldsymbol{W}$ matrix, respectively, of the linear system given by (2.23).

All constraints in the active set are checked at the end of a main iteration, for its possible removal from the set. From a given set of active inequality constraints, a constraint is considered a candidate to be released if it has reached its maximum (minimum) limit and its Lagrange multiplier μ_i^{k-1} has a negative value, or a positive value, depending on the limit it has reached. The normalized candidate released constraint set (*NCRCS)* is defined as,

$$NCRCS=\frac{\left(\mu_1^{k-1},\cdots,\mu_{m_v}^{k-1}\right)}{\max\left(\mu_1^{k-1},\cdots,\mu_{m_v}^{k-1}\right)} \tag{2.35}$$

The candidate constraints that will be released from the active set are the ones corresponding to the elements of *NCRCS* whose normalized Lagrange multipliers are equal to or larger than a specified tolerance TOL_{free}. A value of TOL_{free}=0.1 is used in the algorithm. The release of inequality constraints from the active set is considered in (2.22) by eliminating their contributions to the gradient and $\boldsymbol{W}$ matrix elements.

Once the set of active inequality constraints has been refined, the Lagrange multipliers μ_i are updated as follows [Bertsekas, 1996],

$$\mu_i^k=\begin{cases}\mu_i^{k-1}+c^{k-1}(y_i^k-\overline{y}_i) & \text{if } \mu_i^{k-1}+c^{k-1}(y_i^k-\overline{y}_i)\geq 0\\ \mu_i^{k-1}+c^{k-1}(y_i^k-\underline{y}_i) & \text{if } \mu_i^{k-1}+c^{k-1}(y_i^k-\underline{y}_i)\leq 0\\ 0 & \text{otherwise}\end{cases} \tag{2.36}$$

The accurate selection of the weighting factor initial condition c^0 is very important for the good performance of the Lagrangian Multipliers method. Suggestions for a good initial condition selection are given in 2.3.4.

2.2.5. Handling of inequality constraints on functions

Arguably, the most important functional inequality constraints are those corresponding to controllable sources of reactive power. Reactive power generator limits are checked at the end of each global iteration. It should be pointed out that the reactive power equation of

each generator is placed in the matrix ***W***, however, when the generator is within limits, the method places a large penalty weighting factor S in the diagonal element associated to λ_q. Hence, the corresponding equation is deactivated from the Lagrangian function and its effects on the optimization process are nullified. The functional inequality constraints are activated only when it becomes necessary to enforce either upper or lower limits on reactive power. This is done by removing the large number from the corresponding diagonal element. Penalty function techniques are used to either activate or deactivate the equations corresponding to generation nodes.

Quadratic penalty functions are used since they have first and second derivatives. The form of the penalty function for the reactive power constraint at generation node k is [Luenberger, 1984; Nocedal and Wright, 1999],

$$E_{qi}=\frac{1}{2}S\lambda_{qi}^2 \tag{2.37}$$

and its first and second derivatives are,

$$\frac{dE_{qi}}{d\lambda_{qi}}=S\lambda_{qi} \tag{2.38}$$

$$\frac{d^2E_{qi}}{d^2\lambda_{qi}}=S \tag{2.39}$$

where S is a positive large penalty weighting factor (e.g. S=1x10^9).

Adding the first and second derivatives to the corresponding gradient and diagonal element in matrix ***W*** associated with λ_{qi}, deactivates the reactive power flow equations of the generation node i. In this situation λ_{qi} has a zero value. When a reactive power limit is violated, the derivatives are removed and the node changes from being a generation node to a load node, then λ_{qi} changes its value from zero to nonzero. The sign of λ_{qi} indicates whether or not the reactive power has returned to be within limits [Luenberger, 1984; Nocedal and Wright, 1999], as shown in Table 2.1.

Table 2.1. Handling constraints on reactive power generation

Violated Limit	$\lambda_{qi} < 0$	$\lambda_{qi} > 0$
Upper	to add penalty term	to remove penalty term
Lower	to remove penalty term	to add penalty term

2.3. Implementation of Newton-Based OPF

The OPF mathematical theory given in previous sections was implemented into an existing object oriented C++ computer program [Ambriz-Pérez, 1998]. The main steps of the algorithm are shown in Fig. 2.1.

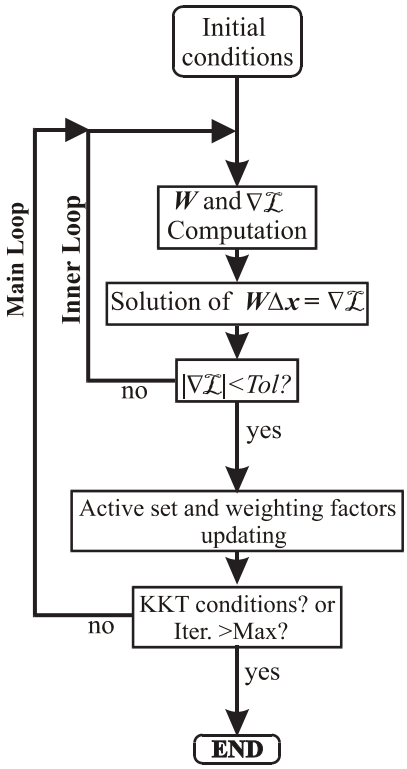

Fig. 2.1. Newton-based optimal power flow chart.

The first step of the Newton-Based OPF algorithm is the initialization of control $\boldsymbol{u}$ and steady state $\boldsymbol{x}$ variables, as well as of both sets of Lagrangian Multipliers $\boldsymbol{\lambda}$ and $\boldsymbol{\mu}$. The related details are given in this section.

After setting initial conditions, the algorithm considers a main loop. One of the two main tasks of this loop is to update the active set of inequality constraints, Lagrangian multipliers $\boldsymbol{\mu}$ and weighting factors. The second task is verifying the KKT conditions, if these conditions are satisfied, the algorithm ends, else goes to the inner loop.

In the inner loop, the nonlinear system obtained from the KKT conditions is solved through the iterative Newton process. In other words, the Newton method is applied to solve the gradient of the Lagragian function equals to zero (2.21). This fact implies the repetitive assembling and solution of the linear system (2.23), until reaching the pre-specified convergence tolerance of Newton method, e.g. $1e^{-6}$. It must be clear that the inner loop is either executed as many times as the KKT conditions are not satisfied in the main loop or until reaching the pre-specified number of allowed main loop iterations, e.g. 20.

An important practical detail is that matrix $\boldsymbol{W}$ is modified to nullify the increments of the slack node angle. This is achieved by placing a large penalty weighting factor in the diagonal element associated with θ_{slack}. Very small increments may still exist but their effect on the rest of the variables is negligible. For practical purposes, the increment $\Delta\theta_{slack}$ is set as 0 at every iteration.

2.3.1. Network voltages initial conditions

Steady state variables are similarly initialized to load flow problems, i.e. 1 pu voltage magnitudes and 0 voltage angles for all nodes. This provides a suitable starting condition.

Engineering experience indicates that, for most problems, the variation of voltage magnitude and voltage angle from the 1 and 0 initial conditions is relatively small, i.e. $0.95 \leq V_k \leq 1.05$ and $-15^0 \leq \theta_k \leq 15^0$.

2.3.2. Economic active power schedule

An economic dispatch as opposed to a load flow solution provides good starting conditions for the full OPF solution. The equal incremental cost criterion is used for this purpose [Wollenberg and Wood, 1984]. The economic dispatch considering active power generation limits, and a lossless network, yields a good starting condition for the Lagrangian multipliers associated to active power balance equality constraints and active power generation variables. The consideration of the network losses into the economic dispatch might yield a better initial condition guess, however it would require higher computing time.

2.3.3. Lagrange multipliers

As already mentioned, the Lagrangian multipliers λ_p, associated to the active power balance constraints, are initialized at their corresponding value of the incremental cost computed by the economic dispatch. The Lagrangian multipliers λ_q, associated to the reactive power balance constraints, are initialized as zero. The Lagrangian Multipliers method uses the multipliers μ, which are also initialized as zero.

2.3.4. Penalty-weighting factors

Effective evaluation of the penalty parameter c is achieved by giving an initial value c^0, with subsequent evaluations of c^k based on monotonic increments: $c^k = \beta c^{k-1}$. Values of c^0 within the range 10^2 - 10^5 have proved being effective starting conditions. In the developed program, a value of c^0=1000 is chosen for voltage magnitude constraints, whereas for active power constraints a good value of c^0 is 1000 times the largest quadratic coefficient of the cost curves [Acha et al., 2004]. Values of β = 1.3 produce very reliable solutions. It is our experience that larger values of β lead to ill-conditioned situations whereas smaller values of β lead to a slow rate of convergence.

The Penalty Functions method used to handle inequality constraints on functions uses the weighting factor S, which is initialized as S=10^{10}.

2.3.5. Convexification term

At the n^{th} iteration of the inner loop, the convexification term is given by

$$C_c \left(y^n - y_r^k \right)^2 \tag{2.40}$$

The scalar penalty parameter C_c has a fixed value during the iterative process. A value of C_c between 0.005 and 0.05 is used in the program. We have found that a value of 0.01 works well on the majority of cases. In (2.40), y_r^k is a reference value of the variable y, at the k^{th} iteration of the main loop, and it changes through the optimization process according with (2.41), at the end of each inner iteration loop. If at the end of this loop y is within limits, the

reference value is given by $y^k = y_r^k$. Otherwise, if y^k violates one of its limits, y_r^{k+1} has a constant value equal to the violated limit.

$$y_r^k = \begin{cases} \underline{y} & \text{if } y^k < \underline{y} \\ \overline{y} & \text{if } y^k > \overline{y} \\ y^k & \text{if } \underline{y} \le y^k \le \overline{y} \end{cases} \tag{2.41}$$

In the developed program, the convexification factor is only applied to voltage magnitude variables. The rationale behind this is that minimization of active power generation costs will, indirectly, reduce transmission network losses; i.e. large network losses mean more active power generation. As a consequence of this, during the repetitive solution of (2.23), voltage magnitudes tend to high values in order to reduce transmission losses. During the development stage of the algorithm, it was observed that in certain cases the voltage magnitudes would tend to unrealistically high values, say around 2 pu. Such a bizarre voltage profile performance was solved by using convexification factors. It should be pointed out that similar observations concerning high voltage magnitudes during the optimization process have been reported elsewhere [Soman et al, 1994], where the unrealistic voltage profile was corrected by using a quadratic penalty term similar to (2.40) but with no convexification factor C_c.

2.4. Conclusions

The OPF analysis is one important function of the Energy Management System, since it is able to provide much useful information for realistic power system operation. In general, the analysis yields the steady state operating point of the power system that minimizes any objective function and satisfies static security aspects. This chapter presents the Newton-based OPF mathematical principles, which focuses on the determination of the most economic dispatch to supply the electric power demand, whilst the violation of any considered power system limit is avoided.

The basic OPF formulation presented in this chapter can be extended to consider different objective functions, many realistic steady and dynamic state security constraints, as well as to consider the inclusion of mathematical models representing a large variety of different power system electric components. Some of these important issues are focused further in this work.

Chapter 3

VSC-HVDC representation in Newton-based OPF

This chapter presents in detail the derivation of the model of a VSC-HVDC system suitable for conventional OPF solutions using the Newton algorithm. The VSC-HVDC's ability to provide independent control of the converters AC voltage magnitudes and phase angles relative to the system voltage, which allows the use of separate active and reactive power control loops for system regulation, is well represented by the model. In this new development in the OPF Newton method, the VSC-HVDC system equations are incorporated directly into the Lagrangian function, Hessian matrix and gradient vector of whole system for a unified optimal solution in a single frame-of-reference. The effectiveness of the VSC-HVDC model and its proposed implementation in the Newton-based OPF existing program [Ambriz-Pérez, 1998] is demonstrated by means of two sample systems.

3.1. VSC-HVDC system model

The VSC-HVDC system consists of two VSC converters with series-connected Insulated Gate Bipolar Transistor (IGBT) valves controlled with Pulse Width Modulation (PWM). According to the application, the converters are connected Back to Back (BtB) in a substation or linked through a common *DC* link, as shown in Fig. 3.1 [ABB, 2005].

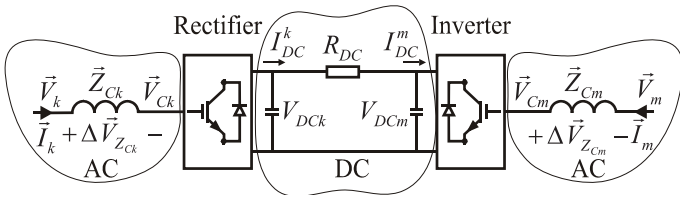

Fig. 3.1. VSC-HVDC transmission link.

The PWM switching control makes possible to have a simultaneous adjustment of the amplitude and phase angle of the converter *AC* output voltage with constant *DC* voltage. This control characteristic allows representing the converter *AC* output voltage at side *i* (*i=k,m*) by a modulated *AC* voltage source $\vec{V}_{Ci} = V_{Ci}\angle\theta_{Ci}$, with amplitude and phase angle limits $V_{Ci}^{\min} \le V_{Ci} \le V_{Ci}^{\max}$ and $0 \le \theta_{Ci} \le 2\pi$, respectively. Hence, the VSC-HVDC transmission link can be represented by the voltage source-based model given in Fig. 3.2. The impedance of the coupling transformer is given by $\vec{Z}_{Ci}$. The converter *DC* side is

represented by the active power exchanged among the converters via the common *DC* link, which must be balanced at any instant, and the *AC-DC* side voltage converter relationships.

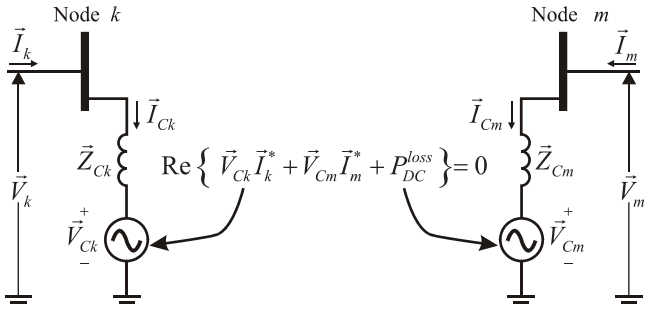

Fig. 3.2. Equivalent circuit of the VSC-HVDC transmission link.

3.1.1. Physical constraints

Based on the equivalent circuit shown in Fig. 3.2, it is possible to obtain the power flows across the *AC* terminals *k* and *m* of the VSC-HVDC system. The powers flowing from node *i* to *j* (*i=k,m*; *j=k,m*; *i≠j*) are,

$$P_{ij}^{inj} = V_i^2 G_{Ci} - V_k V_{Ci}\left[G_{Ci} cos(\theta_i - \theta_{Ci}) + B_{Ci} sin(\theta_i - \theta_{Ci}) \right] \tag{3.1}$$

$$Q_{ij}^{inj} = -V_i^2 B_{Ci} - V_i V_{Ci}\left[G_{Ci} sin(\theta_i - \theta_{Ci}) - B_{Ci} cos(\theta_i - \theta_{Ci}) \right] \tag{3.2}$$

where $G_{Ci} + jB_{Ci} = 1/\vec{Z}_{Ci}$. The powers flow into the converter connected at node *i=k,m* are given as follows:

$$P_{Ci} = V_{Ci}^2 G_{Ci} - V_{Ci} V_i\left[G_{Ci} cos(\theta_{Ci} - \theta_i) + B_{Ci} sin(\theta_{Ci} - \theta_i) \right] \tag{3.3}$$

$$Q_{Ci} = -V_{Ci}^2 B_{Ci} - V_{Ci} V_i\left[G_{Ci} sin(\theta_{Ci} - \theta_i) - B_{Ci} cos(\theta_{Ci} - \theta_i) \right] \tag{3.4}$$

The *AC* side voltage magnitude of the converter connected at node *i*, V_{Ci}, is related to the PWM's amplitude modulation index M_{Ci}, and to the average *DC* capacitor voltage V_{DCi} by [Acha et al., 2004],

$$V_{Ci} = \frac{M_{Ci} V_{DCi}}{2\sqrt{2}} \qquad M_{Ci} \in [0,1] \tag{3.5}$$

The constraining equation relating to the active power exchanged between converters is obtained by neglecting losses in the converter circuits. For the BtB scheme, it is given by,

$$\mathrm{Re}\left\{ \vec{V}_{Ck}\vec{I}_{Ck}^* + \vec{V}_{Cm}\vec{I}_{Cm}^* \right\} = 0 \tag{3.6}$$

For a *DC* link with a series resistance $R_{DC} > 0$, the active power exchanged between converters is constrained by,

$$\mathrm{Re}\left\{ \vec{V}_{Ck}\vec{I}_{Ck}^* + \vec{V}_{Cm}\vec{I}_{Cm}^* \right\} + P_{DC}^{loss} = 0 \tag{3.7}$$

The active power flow direction through the *DC* link must be in accordance with the *DC* voltage magnitudes. This relation is achieved by including the Kirchhoff voltage law

equation on the *DC* side given by (3.8), where the power flowing into the converter connected at node *j* is considered negative.

$$\sum V_{DC} = V_{DCj} - V_{DCi} + P_{Cj} R_{DC} / V_{DCj} = 0 \tag{3.8}$$

It must be pointed out that in order to get practical OPF feasible solutions, the VSC-HVDC model takes into account the operational constraints presented in the following section.

3.1.2. Operational constraints

The operational constraints considered in the model are listed below.

The AC voltage magnitude V_C and phase angle θ_C limits of the VSCs connected at node $i=k,m$, are given as:

$$V_{Ci}^{\min} \le V_{Ci} \le V_{Ci}^{\max} \tag{3.9}$$

$$0 \le \theta_{ci} \le 2\pi \tag{3.10}$$

The modulation index M_C and DC capacitors voltage V_{DCi} limits of the converter connected at node $i=k,m$, are defined as:

$$M_{Ci}^{\min} \le M_{Ci} \le M_{Ci}^{\max} \tag{3.11}$$

$$V_{DCi}^{\min} \le V_{DCi} \le V_{DCi}^{\max} \tag{3.12}$$

It should be noted that (3.12) is only applicable when V_{DCi} is not fixed at a specified value.

In addition, each converter has a specified rating complex power, which is mathematically represented by,

$$S_{Ci} \le S_{Ci}^{r} \tag{3.13}$$

where S_{Ci} is the complex power flowing through the voltage source converter connected at node i ($i=k,m$), defined as follows,

$$S_{Ci} = \sqrt{P_{Ci}^2 + Q_{Ci}^2} \tag{3.14}$$

where P_{Ci}^2 and Q_{Ci}^2 are the active an reactive power through the voltage source converter, respectively. It must be pointed out that P_{Ci}^2 and Q_{Ci}^2, and therefore S_{Ci}, are function of system variables, as corroborated by (3.3) and (3.4).

3.1.3. Control mode constraints

The active power exchanged between the converter and the network is controlled by adjusting the phase shift angle δ_{iCi} between the voltage on the *AC* bus and the fundamental frequency voltage generated by the converter, $\delta_{iCi} = \theta_i - \theta_{Ci}$. The reactive power flow is determined by controlling the difference between these voltage amplitudes, $\Delta V_{iCi} = V_i - V_{Ci}$. Hence, two independent power control loops can be used for regulation, namely active power and reactive power control loops [Bahrman et al., 2003]. In the active power control loop, one converter is set to control the injected active power P_{ij}^{inj} at its *AC* terminal while

the other is set to control the *DC* side voltage V_{DCj} [Bahrman et al., 2003]. In the reactive power control loop both converters have independent control over either voltage magnitude V_i or injected reactive power Q_{ij}^{inj} at their *AC* terminal.

Based on the aforementioned sentence, the control modes *PQ* and *PV* are defined. If the active and reactive powers are set to be controlled by converter *i* at values P_{ij}^{spec} and Q_{ij}^{spec}, respectively; the constraint equations to be satisfied are,

$$P_{ij}^{inj} - P_{ij}^{spec} = 0 \qquad Q_{ij}^{inj} - Q_{ij}^{spec} = 0 \tag{3.15}$$

If the active power and *AC* voltage magnitude are set to be controlled by converter *i*, at values P_{ij}^{spec} and V_i^{spec}, respectively; the constraint equations to be satisfied are

$$P_{ij}^{inj} - P_{ij}^{spec} = 0 \qquad V_i - V_i^{spec} = 0 \tag{3.16}$$

In both cases, the other converter is set to control the *DC* side voltage at a fixed value V_{DC}^{esp}, independently of the reactive power loop control setting, i.e.,

$$V_{DCj} = V_{DCj}^{espc} \tag{3.17}$$

Since the *DC* side voltage is kept constant by converter *j* at a value V_{DCj}^{spec}, this control action is used in the constraining equation representing the active power balance between the two converters to assess losses in the common *DC* link. Hence, the active power losses in the *DC* link are $P_{DC}^{loss} = \left(P_{Cj}^2 R_{DC}\right) / \left(V_{DCj}^{spec}\right)^2$.

3.2. VSC-HVDC OPF formulation

The inclusion of the VSC-HVDC in the OPF algorithm requires the construction of the controller's Lagrangian function which is added to the augmented Lagrangian function given by (2.14). The nodal power mismatch equations at the *AC* controller terminals and the active power exchanged between converters are considered in the OPF formulation through equality constraints. If the power flow through the VSC-HVDC is controlled at a specified value, then this control action is considered as an equality constraint in the formulation. On the other hand, if a control is setting within physical limits, this is taken into account through inequality constraints.

3.2.1. Lagrangian terms of physical and control modes constraints

The equality constraints associated with the VSC-HVDC system operation and all control settings must be satisfied exactly and unconditionally for a feasible OPF solution, so they must be terms of the general augmented Lagrangian function.

For the VSC-HVDC link shown in Fig. 3.2, the Lagrangian term corresponding to the power mismatch equations at nodes *k* and *m* is,

$$\begin{aligned} \mathcal{L}_{km}(\boldsymbol{y}, \boldsymbol{\lambda}) = {} & \lambda_{pk}(P_k^{inj} + P_{Lk} - P_{Gk}) + \lambda_{qk}(Q_k^{inj} + Q_{Lk} - Q_{Gk}) + \\ & \lambda_{pm}(P_m^{inj} + P_{Lm} - P_{Gm}) + \lambda_{qm}(Q_m^{inj} + Q_{Lm} - Q_{Gm}) \end{aligned} \tag{3.18}$$

where λ_{pk}, λ_{pm}, λ_{qk}, λ_{qm} are Lagrange multipliers at nodes *k* and *m*, respectively. The vector of system variables is $\boldsymbol{y} = [\boldsymbol{V}, \boldsymbol{\theta}, \boldsymbol{V_C}, \boldsymbol{\theta_C}]^{tr}$, where $\boldsymbol{V}$ and $\boldsymbol{\theta}$ are nodal voltage magnitudes and angles, whilst $\boldsymbol{V_C}$ and $\boldsymbol{\theta_C}$ are source converter voltage magnitudes and angles; respectively. The superscript *tr* indicates transposition. P_{Li}, and Q_{Li} are the active and reactive power loads at node $i=(k, m)$; respectively. P_{Gi} and Q_{Gi} are the scheduled active and reactive power generations at node $i=(k, m)$; respectively. P_i^{inj} and Q_i^{inj} are the active and reactive power flows at the controller node $i=(k, m)$, given by

$$P_i^{inj} = \sum_{j \in i} P_{ij}^{inj} \qquad Q_i^{inj} = \sum_{j \in i} Q_{ij}^{inj} \tag{3.19}$$

where $\sum_{j \in i}$ is the set of nodes adjacent to node *i*. The equality constraints associated to the VSC-HVDC system operation are included in the OPF algorithm by the following Lagrangian terms,

$$\mathcal{L}_{ACDC}(\boldsymbol{y}, \boldsymbol{\lambda}) = \sum_{i=k,m} \lambda_{ti} \left(V_{Ci} - M_{Ci} V_{DCi} / 2\sqrt{2} \right) \tag{3.20}$$

$$\mathcal{L}_{LVK}(\boldsymbol{y}, \boldsymbol{\lambda}) = \lambda_V \left(\sum V_{DC} \right) \tag{3.21}$$

$$\mathcal{L}_{DC}(\boldsymbol{y}, \lambda) = \lambda_{DC} (P_{Ck} + P_{Cm} + P_{DC}^{loss}) \tag{3.22}$$

where λ_{ti}, λ_V and λ_{DC} are the Lagrange multipliers. For the case of the BtB scheme, the explicit representation of the *DC* link is not required and $P_{DC}^{loss} = R_{DC} = 0$.

The control of active and reactive power flowing from node *i* to *j* ($i=k,m$; $j=k,m$; $i \neq j$) through the VSC-HVDC is represented by the following Lagrangian functions,

$$\mathcal{L}_{CP_{ij}} = \lambda_{CP_{ij}} (P_{ij}^{spec} + P_{ij}^{inj}) \tag{3.23}$$

$$\mathcal{L}_{CQ_{ij}} = \lambda_{CQ_{ij}} (Q_{ij}^{spec} + Q_{ij}^{inj}) \tag{3.24}$$

where $\lambda_{CP_{ij}}$ and $\lambda_{CQ_{ij}}$ are Lagrange multipliers, P_{ij}^{spec} and Q_{ij}^{spec} are the active and reactive power flows to be controlled; respectively. Lastly, P_{ij}^{inj} and Q_{ij}^{inj} are the calculated active and reactive powers given by (3.1) and (3.2), respectively.

As explained in Section 3.1.3, the active power control loop of one converter can be set to control either the active power or the *DC* side voltage. Similarly, the reactive power control loop can be set to control either the reactive power or the *AC* voltage magnitude. If a converter is controlling neither, active nor reactive power, then a quadratic penalty factor is applied to the corresponding multiplier $\lambda_{CF_{ij}}$ ($F=P$ or $F=Q$). In this case the quadratic penalty term given by (3.25) is added to the augmented Lagrange function.

$$E_{\lambda_{CFij}} = \left(S_{\lambda_{CFij}} \left(\lambda_{CFij} \right)^2 \right) / 2 \tag{3.25}$$

The first and second derivatives of (3.25) are added to the corresponding location of the gradient and diagonal entry in the $\boldsymbol{W}$ matrix, associated with $\lambda_{CF_{ij}}$; respectively. This is equivalent to removing the Lagrangian term (3.23) or (3.24) from (3.30), but without

changing the matrix structure, i.e. a large number $S_{\lambda_{CFij}} = 1x10^{10}$ is introduced in the diagonal element of matrix $\boldsymbol{W}$ leading to $\lambda^{k}_{CF_{ij}}$ =0.

The voltage magnitude to be controlled at one of the VSC-HVDC *AC* terminals is set at the specified value V_i^{spec} (i=k,m) and a quadratic penalty term is imposed on this variable during the optimization process. The term to be added to the Lagrange function to take account of this control option is,

$$\mathcal{L}_{CVi} = \frac{1}{2} S_{CV}^{g,W} \left(V_i \right)^2 \tag{3.26}$$

Since the specified voltage is different from zero, it is necessary to produce a null correction of V_i in order to keep it at the specified value during the iterative process. This is achieved by considering a null gradient of (3.26), i.e. $S_{CV}^{g} = 0$, whilst the second derivative of $\mathcal{L}_{CVi}$ adds a large penalty weighting factor $S_{V_{DC}}^{W}$=1x10^{10} to the diagonal entry corresponding to V_i in $\boldsymbol{W}$ matrix. This is equivalent to deactivating equations of partial derivatives of the augmented Lagrangian function with respect to V_i from Newton formulation. Similarly, the *DC* controlled voltage V_{DCj} is kept at a specified value by using the penalty function,

$$E_{V_{DCj}}(\boldsymbol{y}) = \left(S_{V_{DC}}^{g,W} \left(V_{DCj} \right)^2 \right) \Big/ 2 \tag{3.27}$$

where $S_{V_{DC}}^{g}$=0 and $S_{V_{DC}}^{W}$=1x10^{10}.

3.2.2. Handling operational inequality constraints

The operational constraints considered in the VSC-HVDC are all represented by inequalities. Constraints (3.9)-(3.12) are inequality constraints on variables, which can be readily handled through the Lagrange Multiplier method described in Section 2.2.4.

On the other hand, the apparent power rating of each converter is represented as inequality constraint on functions (3.13). In the OPF algorithm it is implemented as described in the next section.

3.2.3. MVA ratings modeling

The power rating of the converters is modeled by the inequality (3.13). In order to handle it with the Quadratic Penalty Function method (see §2.2.5), the constraint is represented by the Lagrangian and penalization terms given below,

$$\mathcal{L}_{r_{Ci}}(\boldsymbol{y},\boldsymbol{\lambda}) = \boldsymbol{\lambda}_{r_{Ci}} (S_{Ci} - S_{Ci}^{r}) \tag{3.28}$$

$$E_{\lambda r_{Ci}} = \frac{1}{2} S_{r_{Ci}} (\boldsymbol{\lambda}_{r_{Ci}})^2 \tag{3.29}$$

where the $\boldsymbol{\lambda}_{r_{Ci}}$ is the Lagrangian Multiplier associated to (3.28), S_{Ci} is the net complex power output of the converter *Ci* connected at node i=k,m. $S_{r_{Ci}}$ is a large positive scalar number ($S_{r_{Ci}}$=1x10^{10}).

The term (3.28) is unconditionally considered in the OPF model during all the optimization process. However, at the beginning of the optimization process it is considered that the complex power of any converter satisfies its MVA power rating (S_{Ci} is lower or equal than S_{Ci}^{r}). Thus, $\lambda_{r_{Ci}}$ must be initialized as zero, and penalized at this value by adding only the second derivative of Lagrangian term (3.29) to corresponding diagonal $\boldsymbol{W}$ matrix element. This is equivalent to remove (3.28) from the OPF model, therefore the source complex output power S_{Ci} is not enforced at its rating S_{Ci}^{r}.

At each step of the optimization process, the apparent output power of any converter must be verified. If there is any violation (S_{Ci} is higher than S_{Ci}^{r}), the inequality (3.13) is activated and the penalization on $\lambda_{r_{Ci}}$ must be removed, i.e., the second derivative of the Lagrangian term is eliminated from $\boldsymbol{W}$. This fact allows updating of $\lambda_{r_{Ci}}$, which acquires values different from zero. This is equivalent to activate the equality $S_{Ci}=S_{Ci}^{r}$, which is implicit in (3.28), so the apparent output power of the converter is enforced to be its rating value.

After removing the penalization on $\lambda_{r_{Ci}}$, it is necessary verifying the sign of $\lambda_{r_{Ci}}$ during the next iterations of the optimization process. If the value of the multiplier is $\lambda_{r_{Ci}}<0$, it means that the converter apparent output power is newly inside of its MVA ratings. Then, the multiplier $\lambda_{r_{Ci}}$ must be set at zero and must be penalized as at the beginning of the procedure. Otherwise, no penalization on $\lambda_{r_{Ci}}$ must be set.

It is important to mention that the aforementioned procedure does not produce structural changes in matrix $\boldsymbol{W}$, which avoids to execute sparse matrix re-ordering techniques.

3.2.4. VSC-HVDC system general Lagrangian function

Based on the control options given in Section 3.1.3, the Lagrange function of the VSC-HVDC system $\mathcal{L}_{km}^{C}$ can take several forms according with the selected control mode. For the case of active and reactive power flow control from node *k* to *m* and the voltage magnitude at node *m* set at a specified value, the Lagrangian term to be added to the augmented Lagrangian function (2.14) is given by (3.30). For this case, the reactive power control from node *m* to *k* is deactivated by the quadratic penalty term $E_{\lambda_{CQkm}}$. The converter connected at node *k* is assumed to be operating within its MVA rating limits, therefore $\lambda_{r_{Ck}}$ must be penalized with the quadratic term $E_{\lambda r_{Ck}}$. On the other hand, it is assumed that the converter connected at node *m* is operating outside its MVA rating limits.

$$\begin{aligned}\mathcal{L}_{km}^{C}=&\mathcal{L}_{km}+\mathcal{L}_{CD}+\mathcal{L}_{LVK}+\mathcal{L}_{CADC}+\mathcal{L}_{CP_{km}}+\mathcal{L}_{CQ_{km}}+\mathcal{L}_{CQ_{mk}}\\&+E_{\lambda_{CQ_{mk}}}+E_{V_{DCm}}+\mathcal{L}_{CV_m}+\mathcal{L}_{r_{Ck}}+\mathcal{L}_{r_{Cm}}+E_{\lambda r_{Ck}}\end{aligned} \tag{3.30}$$

3.2.5. Linearized system of equations

To achieve the minimization of the Lagrangian function (3.30), it is necessary to obtain a set of linearized equations using Newton method as given by (2.23). The vector of correction terms for the system variables and Lagrange multipliers $\Delta_{\mathbf{z}}^{C}(\boldsymbol{y},\boldsymbol{\lambda})$, the gradient vector $\nabla\mathcal{L}^{C}$ and the $\boldsymbol{W}^{\boldsymbol{C}}$ matrix associated to the VSC-HVDC system are,

$$\begin{aligned}\Delta_{\mathbf{z}}^{C}(\boldsymbol{y},\boldsymbol{\lambda})=\Big[&\Delta V_k\ \Delta\theta_k\ \Delta\lambda_{pk}\ \Delta\lambda_{qk}\,\Big|\,\Delta V_m\ \Delta\theta_m\ \Delta\lambda_{pm}\ \Delta\lambda_{qm}\Big|\\ &\Delta V_{Ck}\ \Delta\theta_{Ck}\,\Big|\,\Delta V_{Cm}\ \Delta\theta_{Cm}\,\Big|\,\Delta\lambda_{CD}\ \Delta\lambda_{CP_{km}}\ \Delta\lambda_{CQ_{km}}\ \Delta\lambda_{CQ_{mk}}\\ &\Delta V_{DCk}\ \Delta V_{DCm}\,\Big|\,\Delta M_{Ck}\ \Delta M_{Cm}\,\Big|\,\Delta\lambda_V\ \Delta\lambda_{tk}\ \Delta\lambda_{tm}\ \Delta\lambda_{r_{Ck}}\Big]\end{aligned} \tag{3.31}$$

$$\begin{aligned}g^{C}=\Bigg[&\frac{\partial\mathcal{L}_{km}^{C}}{\partial V_k}\ \frac{\partial\mathcal{L}_{km}^{C}}{\partial\theta_k}\ \frac{\partial\mathcal{L}_{km}^{C}}{\partial\lambda_{pk}}\ \frac{\partial\mathcal{L}_{km}^{C}}{\partial\lambda_{qk}}\,\Bigg|\,\frac{\partial\mathcal{L}_{km}^{C}}{\partial V_m}\ \frac{\partial\mathcal{L}_{km}^{C}}{\partial\theta_m}\ \frac{\partial\mathcal{L}_{km}^{C}}{\partial\lambda_{pm}}\ \frac{\partial\mathcal{L}_{km}^{C}}{\partial\lambda_{qm}}\Bigg|\\ &\frac{\partial\mathcal{L}_{km}^{C}}{\partial V_{Ck}}\ \frac{\partial\mathcal{L}_{km}^{C}}{\partial\theta_{Ck}}\,\Bigg|\,\frac{\partial\mathcal{L}_{km}^{C}}{\partial V_{Cm}}\ \frac{\partial\mathcal{L}_{km}^{C}}{\partial\theta_{Cm}}\,\Bigg|\,\frac{\partial\mathcal{L}_{km}^{C}}{\partial\lambda_{CD}}\ \frac{\partial\mathcal{L}_{km}^{C}}{\partial\lambda_{CP_{km}}}\ \frac{\partial\mathcal{L}_{km}^{C}}{\partial\lambda_{CQ_{km}}}\ \frac{\partial\mathcal{L}_{km}^{C}}{\partial\lambda_{CQ_{mk}}}\\ &\frac{\partial\mathcal{L}_{km}^{C}}{\partial V_{DCk}}\ \frac{\partial\mathcal{L}_{km}^{C}}{\partial V_{DCm}}\,\Bigg|\,\frac{\partial\mathcal{L}_{km}^{C}}{\partial M_{Ck}}\ \frac{\partial\mathcal{L}_{km}^{C}}{\partial M_{Cm}}\,\Bigg|\,\frac{\partial\mathcal{L}_{km}^{C}}{\partial\lambda_V}\ \frac{\partial\mathcal{L}_{km}^{C}}{\partial\lambda_{tk}}\ \frac{\partial\mathcal{L}_{km}^{C}}{\partial\lambda_{tm}}\ \frac{\partial\mathcal{L}_{km}^{C}}{\partial\lambda_{r_{Ck}}}\Bigg]\end{aligned} \tag{3.32}$$

$$\boldsymbol{W}^{\boldsymbol{C}}=\begin{bmatrix}\boldsymbol{W}_{1,1} & \mathbf{0} & \boldsymbol{W}_{1,3} & \boldsymbol{W}_{1,4} & 0 & \boldsymbol{W}_{1,6}\\ \mathbf{0} & \boldsymbol{W}_{2,2} & \boldsymbol{W}_{2,3} & \boldsymbol{W}_{2,4} & \boldsymbol{W}_{2,5} & \boldsymbol{W}_{2,6}\\ \boldsymbol{W}_{1,3}^{t} & \boldsymbol{W}_{2,3}^{t} & \boldsymbol{W}_{3,3} & \boldsymbol{W}_{3,4} & \boldsymbol{W}_{3,5} & \boldsymbol{W}_{3,6}\\ \boldsymbol{W}_{1,4}^{t} & \boldsymbol{W}_{2,4}^{t} & \boldsymbol{W}_{3,4}^{t} & \boldsymbol{W}_{4,4} & \boldsymbol{W}_{4,5} & 0\\ 0 & \boldsymbol{W}_{2,5}^{t} & \boldsymbol{W}_{3,5}^{t} & \boldsymbol{W}_{4,5}^{t} & \boldsymbol{W}_{5,5} & \boldsymbol{W}_{5,6}\\ 0 & \boldsymbol{W}_{2,6}^{t} & \boldsymbol{W}_{3,6}^{t} & 0 & \boldsymbol{W}_{5,6}^{t} & \boldsymbol{W}_{6,6}\end{bmatrix} \tag{3.33}$$

where the elements of submatrices $\boldsymbol{W}_{i,j}$ (i,j=1,…,6) containing the second derivatives of $\mathcal{L}_{km}^{C}$ are given in Appendix A.

Once (3.31)-(3.33) are placed into the vector of correction terms $\Delta\mathbf{z}$, gradient vector $\nabla\mathcal{L}$ and the matrix $\boldsymbol{W}$ of the entire network at the corresponding locations, a sparsity-oriented solution of the KKT conditions is carried out. If different VSC-HVDC operating modes are selected, $\Delta_{\mathbf{z}}^{C}$, $\nabla\mathcal{L}^{C}$ and $\boldsymbol{W}^{\boldsymbol{C}}$ are suitably modified to reflect the modification of $\mathcal{L}_{km}^{C}$ associated to such operating modes.

3.3. Study Cases

The OPF program including the VSC-HVDC model has been applied to the solution of a large number of networks and varying degrees of operational complexity. This section presents the computational results of two different networks to demonstrate the reliability of the proposed approach and developed program. The objective function adopted for minimization is the total cost of active power generation, defined by the quadratic form (2.5). Inequality constraints considered are voltage magnitudes of modulated *AC* voltage sources, the amplitude modulation index of each converter, the *DC* side uncontrolled

voltage, the active and reactive power generations, and nodal voltage magnitudes. Also, the last study case considers the apparent power ratings limits of the VSC-HVDC converters.

3.3.1. 11-Nodes network without apparent power rating limits

The two-area benchmark power system [Xu et al., 1998] is employed to demonstrate how the controller performs. The system consists of two identical areas connected through a relatively weak double-circuit tie line. Each step-up transformer has a reactance of j0.017 pu on a 100 MVA, 20/230 kV base and an off-nominal tap ratio of 1. The lines series impedance and total shunt susceptance are $\vec{Z}_s$=0.0001+j0.001 pu/km and b_c=0.00175 pu/km, respectively. Shunt capacitors are added to buses 7 and 9 to provide system voltage support. The reference voltage angle at node 1 is set to zero. The active power quadratic cost function and generation limits are the same for all generators. The coefficients of the quadratic cost function are a=60 \$/hr, b=3.4 \$/MWhr and c=0.004 \$/MW^{2}hr. Active and reactive power generation limits are $30 \le P_G \le 1200$ MWs and $-500 \le Q_G \le 500$ MVARs, respectively. Nodal voltage magnitude limits have been set to $0.95 \le V \le 1.05$ pu.

Under aforementioned base case conditions, a 321 MW power is transferred from Area 1 to Area 2 with a total cost of 17665.6 \$/hr. The original network has been modified, as shown in Fig. 3.3, to include a BtB VSC-HVDC system which is used to increase the active power flow through the inter-area link to 450 MW, and to set voltage magnitudes at nodes 8 and 8fa at 1 pu. The controller coupling transformer impedances are set at $\vec{Z}_{C8} = \vec{Z}_{C8fa} = 0.001 + j0.01$ pu. The lower and upper limits associated to the controller voltage magnitude sources are 0.97 pu and 1.04 pu, respectively. The amplitude modulation index limits and their initial conditions are $0.5 \le M_{Ci} \le 1.0$ and 0.9, respectively. The *DC* voltage is fixed at 3.0 pu.

Convergence to the optimal solution was obtained in 4 main iterations to a tolerance of 1x10^{-9}. All the inequality constraints are within limits, except voltage magnitudes at generator nodes which were suitably enforced by means of the multiplier method at their maximum limit. The resultant generated power, losses and total cost are shown in Table 3.1.

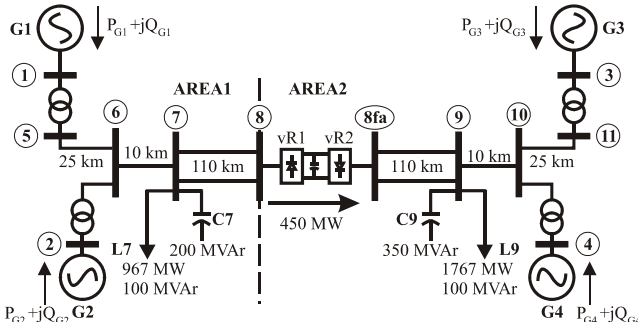

Fig. 3.3. IEEE two-area benchmark system with a BtB VSC-HVDC system.

The control settings were achieved with the VSC having values of $\vec{V}_{C8} = 1.0048\angle -41.63^o$ and $\vec{V}_{C8fa} = 1.0012\angle 11.13^o$ at nodes 8 and 8fa, respectively. The modulation indexes are M_{C8}=0.9474 and M_{C8fa}=0.9440. The VSC-HVDC injected 104.35 MVAR at node 8, and absorbed 22.35 MVAR at node 8fa, in order to maintain the nodal voltage magnitudes controlled at the set values. Owing to the increased active power

transfer between the two areas, a larger amount of active power generation will be required leading to an increase in active power losses. As expected, the optimal solution gives a total system cost higher than the original solution, with no controller.

Table 3.1. Power generation, losses and total cost given by the OPF

Case	OPF with VSC-HVDC		OPF without VSC-HVDC	
	Active (MW)	Reactive (MVAr)	Active (MW)	Reactive (MVAr)
Gen 1	711.78	140.26	642.24	96.91
Gen 2	753.82	254.85	677.16	175.83
Gen 3	659.96	100.84	720.94	113.13
Gen 4	695.48	178.89	763.27	185.01
Total Generation	2821.05	674.84	2803.61	570.88
Total Losses	87.05	1024.84	69.60	920.88
Total Cost ($/hr)	17808.1		17665.6	

3.3.2. 166-Nodes network without apparent power rating limits

To show how the OPF algorithm performs when a VSC-HVDC system is operating in a realistic power system, a network consisting of 166 nodes, 108 transmission lines and 128 transformers was used [Aboytes and Arroyo, 1986]. This network is actually part of a much larger interconnected system which consists of 160 power plants (76 hydro and 84 thermal) with 579 generating units, 2172 nodes, 2294 transmission lines and 768 transformers. The relevant part of the network is shown in Fig. 3.4 which shows the locations of the two VSC-HVDC links.

The OPF study for the base case, without VSC-HVDC links, gives an injected complex power at nodes n1 and n3 of $\vec{S}_{\mathrm{n1}} = 60.30 + j15\,\mathrm{MVA}$ and $\vec{S}_{\mathrm{n3}} = 73.09 - j8.66\,\mathrm{MVA}$, respectively. The voltage magnitude at n3 is 1.012 pu. Each VSC-HVDC replaced an existing transmission line. HVDC1 is used to control the injected power at node n1 at $\vec{S}_{\mathrm{n1}} = 90 + j15\,\mathrm{MVA}$, and to set a voltage magnitude of 1 pu at node n2. Similarly, HVDC2 is used to transfer 80 MW into node n3 and to set the voltage magnitudes at their *AC* terminals to 1 pu. The impedances of the coupling transformers and the limits of the controller voltage sources are $\vec{Z}_{Ci} = 0.001 + j0.1\,\mathrm{pu}$ and $0.97 \le V_{C_i} \le 1.04\,\mathrm{pu}$ (i=1,2,3,4); respectively. Voltages at the *DC* sides of converters C2 and C4 are specified at $V_{DC_{\mathrm{n2}}}^{spec} = V_{DC_{\mathrm{n4}}}^{spec} = 3\,\mathrm{pu}$, and the *DC* line resistance is 0.00334 pu. The *DC* voltage magnitude limits of converters C1 and C3 are $2.7 \le V_{CD} \le 4.9$. The modulation indexes are initialized at 0.8 and their limits are $0.5 \le M_C \le 1.0$.

The solution converged in 3 main iterations to a tolerance for the inner loop of $1\text{x}10^{-9}$. The controllers upheld their target values. Table 3.2 and Table 3.3 summarize the OPF results. In the latter table, the results correspond to the VSC-HVDC system final values.

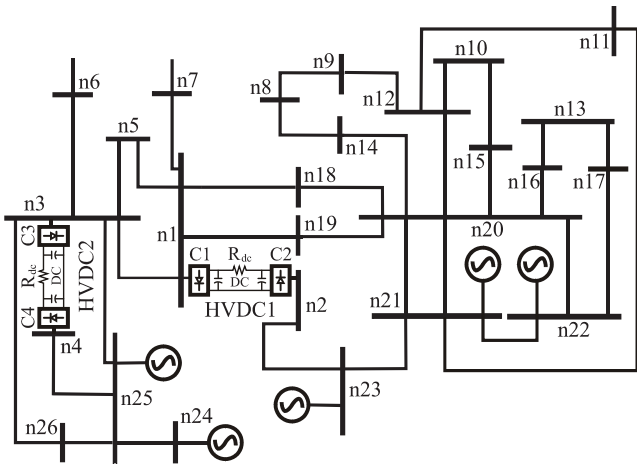

Fig. 3.4. 166 nodes power system with two VSC- HVDC links.

Table 3.2. OPF solution of 166 nodes system

Results	Without VSC-HVDC	With VSC-HVDC
Total Cost of Generation ($/hr)	293.734	293.800
Total Active Power Generation (MW)	2095.71	2096.37
Total Reactive Power Generation (MVAR)	505.52	563.997
Total Active Power Losses (MW)	19.91	20.57
Total Reactive Power Losses (MVAR)	-111.03	-52.57

Table 3.3. Final value of the VSC-HVDC links variables

VSC-HVDC variables	HVDC1		HVDC2	
	C1	C2	C3	C4
V_C (pu)	1.02	1.02	1.01	1.01
θ_C (deg.)	2.75	-4.45	0.63	-7.69
P_C (MW)	90.083	-90.113	80.064	-80.088
Q_C (MVARs)	23.297	29.082	10.460	9.039
Sc	93.050	94.690	80.744	80.597
V_{DC} (pu)	2.9990	3.0000	2.9991	3.0000
M_C	0.9634	0.9659	0.9507	0.9479
DC Link Current (pu)	0.300377		0.266960	
DC Link Losses	0.0301356		0.0238034	

3.3.3. 166-Nodes network considering apparent power rating limits

In order to carry out comparisons of results obtained with and without considering the VSC-HVDC power ratings, the system and simulation parameters shown in Section 3.3.2 are newly considered in this case. The VSC-HVDC systems have the same parameters, but now the apparent ratings of each converter are considered. Both voltage sources of the HVDC1 are 93 MVA rating, whilst both voltage sources of the HVDC2 are 80.1 MVA rating. These limits values were selected in order to produce the violation of each converter apparent rating, as it can be expected from the converter apparent power reported in Table 3.3.

For this case study the algorithm convergence was achieved at 7 main iterations, considering a tolerance in the inner loop of $1x10^{-9}$. Table 3.4 and Table 3.5 show a summary of results.

From Table 3.2 and Table 3.4 it is possible to observe a small increment of the total generation cost when apparent power ratings limits are considered. This effect is produced by the increment of the active power losses in the network. At the same time, the network active power losses are increased due to the power flow redistribution, along the transmission network to satisfy the converters apparent power limits. Note from Table 3.5 that the converters apparent powers are below the defined ratings, different to the results reported in Table 3.3 where apparent power limits of the converters are not considered.

It must be clear that in this case study the VSC-HVDC systems are operating at quite stressed conditions, since the active power flow, voltage magnitude and reactive power control settings hit by themselves the apparent power ratings limits. This is the reason the algorithm convergence was achieved after four more iterations than the previous case study of Section 3.3.2. It must be pointed out that if any active power flow, voltage magnitude or reactive power control setting of the VSC-HVDC systems is set at some higher value, the solution might be unfeasible.

Table 3.4. OPF solution of 166 nodes system with VSC-HVDC power ratings limits

Results	With MVA limits
Total Cost of Generation ($/hr)	293.91
Total Active Power Generation (MW)	2096.73
Total Reactive Power Generation (MVAR)	537.549
Total Active Power Losses (MW)	20.93
Total Reactive Power Losses (MVAR)	-78.9958

Table 3.5. Final value of the VSC-HVDC links variables considering power ratings limits

VSC-HVDC variables	HVDC1		HVDC2	
	C1	C2	C3	C4
V_C (pu)	1.03	1.01	0.99	0.99
θ_C (deg.)	2.61	-4.53	0.74	-7.70
P_C (MW)	90.081	-90.111	80.065	-80.089
Q_C (MVARs)	23.117	6.953	-2.375	1.352
Sc	93.00	90.40	80.10	80.10
V_{DC} (pu)	2.9990	3.0000	2.9991	3.0000
M_C	0.9736	0.9447	0.9385	0.9403
DC Link Current (pu)	0.299401		0.266467	
DC Link Losses (MW)	0.0301344		0.0238037	

3.4. Conclusions

The VSC-HVDC proposed model for OPF studies has been derived from first principles, and implemented in an existing OPF program. The controller variables are combined with the network unknown variables for a unified solution via the minimization of Lagrange functions using Newton method. A detailed description of how the VSC-HVDC and network inequality constraints are handled by the multipliers method is provided in this chapter. The efficiency of the algorithm has been illustrated by numerical examples. The

flexibility that the VSC-HVDC has for controlling active and reactive power flows and nodal voltage magnitudes offers great potential in solving many of the operational problems facing the electric utility industry. To this end, the proposed Newton OPF gives an answer to how to exploit the controller capabilities in order to supply the demand more economically, while keeping all the constraints imposed on the system within bounds.

Chapter 4

Global Transient Stability Constrained Optimal Power Flow Method

The theoretical bases for transient stability assessment and preventive control by means of a generic global approach are presented in this chapter. To investigate the system transient stability of the power system the TD analysis is formulated according to the Simultaneous Implicit model. To accomplish with this model, the system transient dynamics are mathematically represented by the classical model of the generator and the structure preserving model of the network, which is described by a set of differential-algebraic equations DAE. The DAE set is transformed into difference algebraic equations by applying the implicit trapezoidal rule, resulting in a set of non linear algebraic equations that can be readily solved through the Newton method.

The general formulation of the TSC-OPF problem is presented in terms of steady state, dynamic state and stability constraints. Steady state constraints are those corresponding to the conventional OPF, whilst the dynamic constraints are the difference algebraic equations set, which results of applying the trapezoidal rule to the DAE set that describes the power system dynamics. In this generic TSC-OPF model, the transient stability constraints are formulated according with the stability index based on the rotor angle limit. The general TSC-OPF algorithm is presented in order to set the fundamentals of the proposed stability control approaches.

4.1. Power system stability definition and classification

Power system stability has been recognized as an important problem for secure system operation since the 1920s [Kundur, 1994]. Thus the power system operation involves both stability and security.

Power system security is the ability of the power system to withstand sudden disturbances such as electric short circuits or non-anticipated loss of system components [Kundur et al., 2004]. Power system security involves a wide range of system operation aspects, which can be classified into the categories of static and dynamic phenomena [Pavella et al., 2000].

On the other hand, Power system stability is defined as the ability of an electric power system, for a given initial operating condition, to regain a state of operating equilibrium after being subjected to a physical disturbance, with most system variables bounded so that practically the entire system remains intact [Kundur et al., 2004]. Power system stability is classified into the dynamic part of security.

From a global viewpoint, power system stability is essentially a single problem, however, the various forms of instabilities that a power system may undergo cannot be properly understood and effectively dealt with by treating it as such [Kundur et al., 2004]. Therefore, the system stability has been classified according to the time span required to assess the system instability, the size of the disturbance in question and the physical nature of the resulting instability. The classification is illustrated in Fig. 4.1. The transient stability problem is focused in this research work.

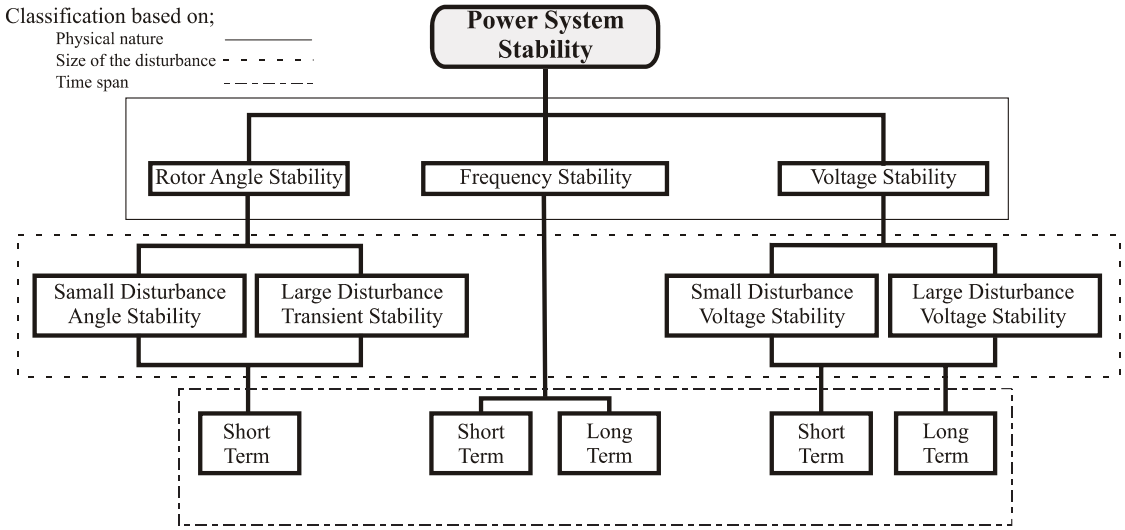

Fig. 4.1. Classification of power system stability.

4.2. Transient stability

The Transient Stability (TS) of a power system is defined as its ability to maintain synchronism when subjected to a severe disturbance, such as a short circuit on a transmission line. A transient instability usually appears in the form of aperiodic angular separation of the system machine rotor angles due to insufficient synchronizing torque.

The phenomenon of transient stability with fast nonlinear dynamics and disastrous practical consequences, makes it a problem that must be considered by engineers in charge of an electric power system. Therefore, transient stability analysis is an essential study in the operation and planning of electric power systems [Kundur, 1994]. If this study determines that a rotor angle transient instability takes place due to large electromechanical oscillations among generation units and lack of synchronizing torque on the system, control actions have to be taken to prevent partial or complete service interruption.

The transient stability properties of a power system mainly depend on both the initial operating state of the system and the severity of the disturbance. These stability properties can be determined by Time-Domain (TD) analysis, which is applicable for sophisticated mathematical models of electric components, and is feasible for large-scale power system analysis. The time frame of interest in TD analysis is usually from 3 to 5 seconds following the disturbance. It may be extended to 10–20 seconds for very large systems with dominant inter-area swings [Stott, 1979; Kundur et al., 2004].

The TD method is the reference for the transient stability study [Pavella et al., 2000] and is considered in this work. However, the TD method by itself does not provide useful information for transient stability quantitative assessment and control. Therefore, for the

purpose of efficiently assessing and controlling the system transient stability, the SIngle Machine Equivalent (SIME) method is considered in this work.

4.2.1. Mathematical formulation of the problem

An electric power system dynamic behavior can be mathematically represented by a set of differential equations constrained by a set of algebraic equations; this Differential Algebraic Equation (DAEs) model is given by (4.1)-(4.2) [Sauer and Pai, 1998], where $\boldsymbol{x_s}$ is a vector of the dynamic state variables, $\boldsymbol{y}$ is a vector of the algebraic variables (usually network complex nodal voltages), and $\boldsymbol{u}$ is a set of non-time varying system parameters.

$$\dot{\boldsymbol{x}}_{\boldsymbol{s}} = F(\boldsymbol{x}_s, \boldsymbol{y}, \boldsymbol{u}) \qquad F: \Re^{n+m+p} \rightarrow \Re^n \tag{4.1}$$

$$0 = g(\boldsymbol{x}_{\boldsymbol{s}}, \boldsymbol{y}, \boldsymbol{u}) \qquad g: \Re^{n+m+p} \rightarrow \Re^n \tag{4.2}$$

where $\boldsymbol{x}_s \in X \subset \Re^n$, $\boldsymbol{y} \in Y \subset \Re^m$ and $\boldsymbol{u} \in U \subset \Re^p$. Due to the fact that transmission network dynamics are much faster than dynamics of the equipment or loads, it is considered that the variables $\boldsymbol{y}$ change instantaneously with variations of the $\boldsymbol{x}_s$ states. Hence, only the dynamics of the equipment, e.g. generators, controls, FACTS devices, and load at buses, are explicitly modeled by the set of differential equations (4.1). The set of algebraic equations (4.2) express the mismatch power flow equations at each node of the network. As the power system can be viewed as an interconnection of several electric power plant components, particulars of each model are given below. All variables are given in per unit, unless otherwise specified.

4.2.2. Generator's classical model

The classical model of the generator is considered for transient stability studies in this work, since this model is accurate enough to describe the first swing instability phenomena [Kundur, 1994]. Fig. 4.2 shows the equivalent circuit of the generator's classical model.

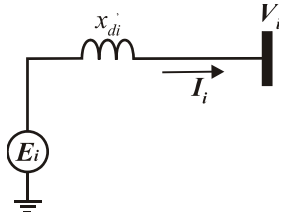

Fig. 4.2. Classical model of the synchronous generator.

The generator equivalent circuit is composed by an internal voltage source with constant magnitude E_i behind the transient reactance X'_d. $\boldsymbol{I}_i$ is the stator current for the i^{th} generator. The complex voltage $\boldsymbol{V}_i$ at the generator terminals is defined by (4.3) [Sauer and Pai, 1998].

$$\boldsymbol{V}_i = \boldsymbol{E}_i - jX'_{di}\boldsymbol{I}_i \tag{4.3}$$

The rotor dynamics are mathematically modelled by the swing equations [Kundur, 1994; Sauer and Pai, 1998]. For the i^{th} generator, these equations are,

$$\dot{\delta}_i^t = \omega_i^t - \omega_s \tag{4.4}$$

$$\dot{\omega}_i^t = \frac{\omega_s}{2H_i}\left(P_{mi}^{t0} - P_{ei}^t - D_i(\omega_i^t - \omega_s)\right) \tag{4.5}$$

where the superscripts t_0 and t indicate steady and transient state, respectively, H_i is the inertia constant in seconds (s), D_i is the damping constant, δ_i^t is the generator rotor angle in radians (rad), ω_s is the synchronous speed in rad/sec. $P_m^{t_0}$ represent the turbine mechanical injection, which is considered constant during the transient period. This power corresponds, without considering internal machine power losses, to that computed by conventional OPF analysis. Lastly, P_{ei}^t is the generator's active power delivered at its terminals, and associated with the internal voltage, as described by (4.6) [Sauer and Pai, 1998].

$$P_{ei}^t = \frac{E_i V_i^t}{X'_{di}} Sin(\delta_i^t - \theta_i^t) \tag{4.6}$$

where V_i^t and θ_i^t are the voltage magnitude and angle at the generator's terminal during the transient state. Similarly, the generator reactive output power is computed by (4.7) [Sauer and Pai, 1998].

$$Q_{ei}^t = \frac{E_i V_i^t}{X'_{di}} Cos(\theta_i^t - \delta_i^t) - \frac{(V_i^t)^2}{X'_{di}} \tag{4.7}$$

4.2.3. Load model

The classical constant impedance load model is considered to capture the transient system trajectories. The equivalent impedance values are computed at the i^{th} load node from the equilibrium point that defines the steady state operation of the power system [Sauer and Pai, 1998]. In this work, the equivalent load impedance is not explicitly computed, but its active and reactive power consumption during the transient state are computed as follows,

$$P_{lGi}^t = P_{Li}\left(\frac{V_i^t}{V_i^{t0}}\right)^2 \tag{4.8}$$

$$Q_{lBi}^t = Q_{Li}\left(\frac{V_i^t}{V_i^{t0}}\right)^2 \tag{4.9}$$

where P_{Li} and Q_{Li} are the nominal load at node i. V_i^{t0} is the nominal voltage measured at steady state. These quantities are computed from the OPF analysis of Chapter 2.

4.2.4. Network model for transient state

The network model describing the transient state of the system is composed by the power flow balance equations given by the following constraint set [Sauer and Pai, 1998],

$$P_{ei}^t - P_{lGi}^t - \sum_{j \in i} P_{inj\,ij}^t = 0 \tag{4.10}$$

$$Q_{ei}^t - Q_{lGi}^t - \sum_{j \in i} Q_{inj\,ij}^t = 0 \tag{4.11}$$

where $t \in T$ and i=1,2,…,N_b. T is the time integration interval to be considered in the Time Domain analysis and N_b is the number of system buses. The terms P_{lGi}^t and Q_{lGi}^t correspond to the active and reactive load powers, formulated by (4.8)-(4.9), respectively. P_{ei}^t and Q_{ei}^t

are the active an reactive electric output power of the generator, respectively described by (4.6) and (4.7). $P^t_{inj\,ij}$ and $Q^t_{inj\,ij}$ are the active and reactive power flows injected at node *i* at time *t* of the transient state, and are computed from [Sauer and Pai, 1998],

$$P^t_{inj\,ij} = V_i^t V_j^t \left(G_{ij} Cos(\theta_i^t - \theta_j^t) + B_{ij} Sin(\theta_i^t - \theta_j^t) \right) + \left(V_i^t\right)^2 G_{ii} \tag{4.12}$$

$$Q^t_{inj\,ij} = V_i^t V_j^t \left(G_{ij} Sin(\theta_i^t - \theta_j^t) - B_{ij} Cos(\theta_i^t - \theta_j^t) \right) - \left(V_i^t\right)^2 B_{ii} \tag{4.13}$$

where G_{ij} and B_{ij} are the equivalent conductance and susceptance of the transmission element connected between nodes *i* and *j*, respectively.

4.2.5. Structure preserving Newton-based solution method

Transient stability studies based on time-domain analysis consist of solving the DAE's mathematical model described by (4.1)-(4.2). There are several methods for solving this kind of mathematical model, but there are basically two approaches used in power system simulation packages: Simultaneous Implicit (SI) and Partitioned Explicit (PE) methods [Sauer and Pai, 1998].

The SI method can handle shift equations very well and is more stable than the PE method. These two reasons explain why the SI method is the most preferred approach to develop of commercial grade transient stability programs. The SI method aims to simultaneously solving the DAE's system. To make it possible, the differential set (4.1) is converted (discretized) into algebraic equations by using either the Euler's implicit method or the Implicit Trapezoidal rule. The resulting algebraic equations set is added to the nonlinear algebraic set (4.2), then both nonlinear algebraic sets are solved in a unified reference frame by using Newton method. In this work the SI method together with the Implicit Trapezoidal rule is used to carry out time-domain analysis considering the Structure Preserving Model of the power system, details are given below.

4.2.6. Structure preserving classical model

The structure preserving model is basically described by the general DAE's system given by (4.1)-(4.2). In power system analysis, this model has been widely used in structure preserving transient energy function and voltage collapse literature that uses energy functions [Sauer and Pai, 1998]. The schematic representation of this model is shown in Fig. 4.3.

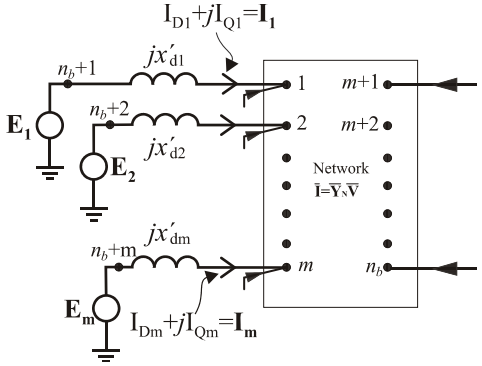

Fig. 4.3. Structure preserving model schematic representation.

In Fig. 4.3 the *nb* bus system is extended by the constant voltage behind the transient reactances at the generator buses n_g=1,2,..,*m.* The generator internal nodes are denoted by n_{gi} =*n+1*,…,*n+m*. In the mathematical representation of this model, the general differential equation set (4.1) is related to the generator swing equations (4.4)-(4.5). On the other hand, the algebraic set (4.2) is associated with the network transient state constraints (4.10)-(4.11). Under this context, the structure preserving model of the system is given by [Sauer and Pai, 1998],

$$\dot{\delta}_i^t = \omega_i^t - \omega_s \qquad t \in T,\ i=1,2,\ldots,n_g \qquad (4.14)$$

$$\dot{\omega}_i^t = \frac{\omega_s}{2H_i}\left(P_{mi}^{t0} - P_{ei}^t - D_i(\omega_i^t - \omega_s)\right) \qquad t \in T,\ i=1,2,\ldots,n_g \qquad (4.15)$$

$$P_{ei}^t - P_{lGi}^t - \sum_{j\in i} P_{inj\,ij}^t = 0 \qquad t \in T,\ i=1,2,\ldots,n_b \qquad (4.16)$$

$$Q_{ei}^t - Q_{lGi}^t - \sum_{j\in i} Q_{inj\,ij}^t = 0 \qquad t \in T,\ i=1,2,\ldots,n_b \qquad (4.17)$$

The Simultaneous Implicit method is used to solve (4.14)-(4.17), which requires applying the Implicit Trapezoidal rule to discretize the generator swing equations (4.14)-(4.15).

4.2.7. Discretization of the swing equations

Due to its numerical stability, the implicit trapezoidal rule is widely used to discretize differential equations involved in transient stability studies. This rule states that an ordinary differential equation of the form (4.1) can be represented at a single time integration step *t* of the integration interval *T* by the following algebraic function [Rafian et al., 1987],

$$\varphi(x_s^t, y^t, u) = \left(x_s^t - \frac{\Delta t}{2}F(x_s^t, y^t, u)\right) - \left(x_s^{t-\Delta t} + \frac{\Delta t}{2}F(x_s^{t-\Delta t}, y^{t-\Delta t}, u)\right), \qquad t \in T \qquad (4.18)$$

where Δt is the length of the integration step time. Generator swing equations are formulated as difference constraints according to (4.18). Considering the synchronous reference frame this set is included into the structure preserving model as follows,

$$\varphi_\delta(\cdot) = \left(\delta_i^t - \frac{\Delta t}{2}(\Delta\omega_i^t)\right) - \left(\delta_i^{t-\Delta t} + \frac{\Delta t}{2}(\Delta\omega_i^{t-\Delta t})\right), \quad \begin{matrix} t\in T \\ i=1,\ldots,n_g \end{matrix} \qquad (4.19)$$

$$\varphi_\omega(\cdot) = \left(\omega_i^t - \frac{\Delta t}{2M_i}\left(P_{mi}^{t0} - P_{ei}^t - D_i(\Delta\omega_i^t)\right)\right) - \left(\omega_i^{t-\Delta t} + \frac{\Delta t}{2M_i}\left(P_{mi}^{t0} - P_{ei}^{t-\Delta t} - D_i(\Delta\omega_i^{t-\Delta t})\right)\right), \quad \begin{matrix} t\in T \\ i=1,\ldots,n_g \end{matrix} \qquad (4.20)$$

$$\Delta P^t = P_{ei}^t - P_{lGi}^t - \sum_{j\in i} P_{inj\,ij}^t = 0 \qquad t \in T,\ i=1,2,\ldots,n_b \qquad (4.21)$$

$$\Delta Q^t = Q_{ei}^t - Q_{lGi}^t - \sum_{j\in i} Q_{inj\,ij}^t = 0 \qquad t \in T,\ i=1,2,\ldots,n_b \qquad (4.22)$$

where $M_i = \omega_s / 2H_i$ is the inertia coefficient for the *i-th* generator, $\Delta\omega = (\omega - \omega_s)$ is the rotor's speed deviation w.r.t. to the synchronous speed ω_s .

It must be noted that the structure preserving model is only composed by the nonlinear algebraic equation set (4.19)-(4.22). The solution of this set can be readily obtained by using Newton method, where the corresponding linearized system is formulated by (4.23).

$$\left[\begin{array}{cc|cc} \frac{d\Delta P^t}{d\boldsymbol{\theta}^t} & \boldsymbol{V}\frac{d\Delta P^t}{d\boldsymbol{V}^t} & \frac{d\Delta P^t}{d\boldsymbol{\delta}^t} & 0 \\ \frac{d\Delta Q^t}{d\boldsymbol{\theta}^t} & \boldsymbol{V}\frac{d\Delta Q^t}{d\boldsymbol{V}^t} & \frac{d\Delta Q^t}{d\boldsymbol{\delta}^t} & 0 \\ \hline 0 & 0 & \frac{d\varphi_\delta(\cdot)}{d\boldsymbol{\delta}^t} & \frac{d\varphi_\delta(\cdot)}{d\boldsymbol{\omega}^t} \\ \frac{d\varphi_\omega(\cdot)}{d\boldsymbol{\theta}^t} & \boldsymbol{V}^t\frac{d\varphi_\omega(\cdot)}{d\boldsymbol{V}^t} & \frac{d\varphi_\omega(\cdot)}{d\boldsymbol{\delta}^t} & \frac{d\varphi_\omega(\cdot)}{d\boldsymbol{\omega}^t} \end{array}\right]^k \left[\begin{array}{c} \Delta\boldsymbol{\theta}^t \\ \frac{\Delta\boldsymbol{V}^t}{\boldsymbol{V}^t} \\ \Delta\boldsymbol{\delta}^t \\ \Delta\boldsymbol{\omega}^t \end{array}\right]^k = -\left[\begin{array}{c} \Delta P^t \\ \Delta Q^t \\ \varphi_\delta(\cdot) \\ \varphi_\omega(\cdot) \end{array}\right]^k \quad ,t\in T \tag{4.23}$$

Where k indicates the iteration number of the Newton method, the system variables are updated according to:

$$[\boldsymbol{\theta}^t,\boldsymbol{V}^t,\boldsymbol{\delta}^t,\boldsymbol{\omega}^t]^{k+1}=[\Delta\boldsymbol{\theta}^t,\Delta\boldsymbol{V}^t,\Delta\boldsymbol{\delta}^t,\Delta\boldsymbol{\omega}^t]^k+[\boldsymbol{\theta}^t,\boldsymbol{V}^t,\boldsymbol{\delta}^t,\boldsymbol{\omega}^t]^k \quad ,t\in T \tag{4.24}$$

The repetitive solution of (4.23), yields at the k^{th} iteration the system dynamics for the single time step t of the whole integration interval T. The whole system dynamics defined in T are described by the solution set S, which is composed by the solution of (4.19) -(4.22) for each time step t.

4.2.8. Initial conditions for time-domain analysis

Initial conditions are necessary to carry out the solution of the equation set (4.19)-(4.22). System variables $\boldsymbol{x}_s$,$\boldsymbol{y}$, and $\boldsymbol{u}$ can be initialized based on the steady state operating point obtained from a power flow analysis. It is also possible to initialize these variables by using the optimum steady state operating point given by OPF analysis, as considered in this work. Here, the network dynamic state complex voltages $\boldsymbol{V}^t\angle\boldsymbol{\theta}^t$ are initialized with the complex voltage steady state profile $\boldsymbol{V}^{t_0}\angle\boldsymbol{\theta}^{t_0}$ obtained by OPF analysis. The mechanical power of generators $\boldsymbol{P}_m$ is scheduled at the values computed by this same analysis. The magnitude of each generator internal complex voltage E_i and rotor angle δ_i^t are initialized from the simultaneous solution of (4.25)-(4.26) [Gan et al., 2000].

$$E_iV_i^{t_0}Sin(\delta_i^{t_0}-\theta_i^{t_0})-X'_{di}P_{mi}^{t_0}=0 \tag{4.25}$$

$$E_iV_i^{t_0}Cos(\theta_i^{t_0}-\delta_i^{t_0})-\left(V_i^{t_0}\right)^2-X'_{di}Q_{gi}^{t_0}=0 \tag{4.26}$$

The rotor speed ω_i^t is initialize as indicated by (4.27).

$$\omega_i^{t_0}=\omega_s \tag{4.27}$$

where $\delta_i^{t_0}$ and $\omega_i^{t_0}$ represent the steady state value of δ_i^t and ω_i^t, respectively. $V_i^{t_0}$ and $\theta_i^{t_0}$ are the steady state voltage magnitude and angle, respectively, at the i^{th} generator terminals.

4.3. Transient Stability-Constrained Optimal Power Flow conventional approach

The aim of the transient stability preventive control approach described in this section consists of formulating the generation rescheduling as an optimization problem, where the conventional OPF model (2.1)-(2.4) is extended to include the set of differential-algebraic equations (4.14)-(4.17) that describes system dynamics subjected to a credible disturbance, along with transient stability limits. When the solution of this model is carried out in a unified reference frame, the optimization procedure is called global Transient Stability-Constrained Optimal Power Flow (TSC-OPF) approach [Ruiz-Vega and Pavella, 2003]. The global TSC-OPF approach yields the values of control variables, steady and transient state variables, which satisfy all the imposed static and dynamic security constraints while minimizing the specified objective function. This solution ensures that the synchronous generators maintain stability in response to a specified credible contingency.

4.3.1. General formulation

For simplicity of notation, assuming that there is only one contingency in the security analysis, the general formulation of the Transient Stability-Constrained Optimal Power Flow can be expressed, from the time t_0 of the inception of the disturbance to the clearing time t_{cl}, and from this time to the end of the study time period t_{end}, $T = [t_0, t_{cl}) \cup (t_{cl}, t_{end}]$, as follows [La Scala et al., 1998; Gan et al., 2000]:

$$\min \; f(\boldsymbol{u}) \tag{4.28}$$

subject to

Prefault steady state constraints:

$$G^{t_0}\left(\boldsymbol{y}^{t_0}, \boldsymbol{u}\right) = 0, \;\; I^{t_0}\left(\boldsymbol{x}^{t_0}\right) = 0, \;\; H^{t_0}\left(\boldsymbol{y}^{t_0}, \boldsymbol{u}\right) \le 0, \quad \underline{\boldsymbol{u}} \le \boldsymbol{u} \le \overline{\boldsymbol{u}} \tag{4.29}$$

Dynamic constraints:

$$\dot{\boldsymbol{x}}(t) - F\left(\boldsymbol{x}(t), \boldsymbol{y}(t)\right) = 0, \;\; \boldsymbol{x}(t_0) = \boldsymbol{x}, \;\; \boldsymbol{y}(t_0) = \boldsymbol{y}, \quad t \in T \tag{4.30}$$

$$G\left(\boldsymbol{x}(t), \boldsymbol{y}(t), \boldsymbol{u}\right) = 0, \quad t \in T \tag{4.31}$$

Transient stability constraints:

$$H\left(\boldsymbol{x}(t), \boldsymbol{y}(t), \boldsymbol{u}\right) \le 0, \;\; t \in (t_{cl}, t_{end}] \tag{4.32}$$

where $f(\cdot)$ is the objective function; $\boldsymbol{u}$ is a vector of control variables with upper bound $\overline{\boldsymbol{u}}$ and lower bound $\underline{\boldsymbol{u}}$; $\boldsymbol{x}(t)$ and $\boldsymbol{y}(t)$ are the power system state and algebraic variables during the transient period, while $\boldsymbol{y}^{t_0}$ and $\boldsymbol{x}^{t_0}$ are variables at the initial prefault steady state, as indicated by superscript t_0. $G^{t_0}(\cdot)$ and $I^{t_0}(\cdot)$ are equality constraints representing the power flow mismatch equations and the initial conditions equations for state variables, respectively, whilst $H^{t_0}(\cdot)$ are inequality constraints associated with the system physical and operation limits. $F(\cdot)$ are functions describing the power plant component dynamics, $G(\cdot)$ are equality constraints representing the network power balance equations that must

be satisfied at each time step and $H(\cdot)$ are inequality constraints associated with transient stability limits.

The TSC-OPF formulated by (4.28)-(4.32) is a nonlinear optimization problem with differential and algebraic equation constraints. Conventional optimization techniques can not directly handle with differential equations so, in order to be able to solve this problem, the set of differential equations (4.30) are converted into difference (algebraic) equations by a discretizing scheme [La Scala et al., 1998; Gan et al., 2000]. Here, trapezoidal rule is applied to convert the dynamic constraint (4.30) as follows [Rafian et al., 1987]:

$$\varphi(\boldsymbol{x}(t),\boldsymbol{y}(t),\boldsymbol{u})=\varphi_t(\boldsymbol{x}(t),\boldsymbol{y}(t),\boldsymbol{u})-\varphi_h(\boldsymbol{x}(t-\Delta t),\boldsymbol{y}(t-\Delta t),\boldsymbol{u})=0, t\in T \tag{4.33}$$

where Δt is the integration time step, $\varphi(\cdot)$ represents a set of difference equations of (4.30), and terms $\varphi_t(\cdot)$ and $\varphi_h(\cdot)$ are defined by,

$$\varphi_t(\boldsymbol{x}(t),\boldsymbol{y}(t),\boldsymbol{u}) = \boldsymbol{x}(t) - \frac{\Delta t}{2} F(\boldsymbol{x}(t),\boldsymbol{y}(t),\boldsymbol{u}) \tag{4.34}$$

$$\varphi_h(\boldsymbol{x}(t-\Delta t),\boldsymbol{y}(t-\Delta t),\boldsymbol{u})=\boldsymbol{x}(t-\Delta t)+\frac{\Delta t}{2}F(\boldsymbol{x}(t-\Delta t),\boldsymbol{y}(t-\Delta t),\boldsymbol{u}) \tag{4.35}$$

Now the optimization problem described by the general equations (4.28)-(4.29) and (4.31)-(4.35), can be solved via a conventional optimization nonlinear technique. It must be pointed out that the discretization scheme results in a huge increasing of the number of variables involved in the optimization model.

In order to present a more explicit structure of the TSC-OPF mathematical model, the previous general formulation is developed according to the specific optimization model considered in this work. For the sake of simplicity, the classical model of the generator is considered. The generator internal power losses are ignored, and therefore at steady state the scheduled mechanical input power P_m of the generators equals the electric active output power P_e. The explicit TSC-OPF formulation is given, in polar coordinates, as follows.

4.3.2. Objective function

The objective function is the minimization of the total power generation cost, described by [Huneault and Galiana, 2009],

$$f(\cdot)=\sum_{i=1}^{N_g} a_i+b_i\,(P_{m\,i}^{t_0})+c_i\,(P_{m\,i}^{t_0})^2 \tag{4.36}$$

where a_i, b_i and c_i are the cost curve coefficients for the generation bus i. N_g is the number of generators, whose individual scheduled mechanical power is P_{mi}. Superscript t_0 means that these values correspond to the initial steady state.

4.3.3. Pre-fault steady state constraints

Similarly to conventional OPF, the system steady state is subjected to the sets of constraints given below.

The power balance at each bus must be satisfied according to the following constraint set [Acha et al., 2004],

$$G^{t_0}(\cdot)=\left\{\begin{matrix} P_{mi}^{t_0}-P_{li}^{t_0}-\sum_{j\in i}P_{inj\,i\,j}^{t_0}=0, \\ Q_{g\,i}^{t_0}-Q_{li}^{t_0}-\sum_{j\in i}Q_{inj\,i\,j}^{t_0}=0 \end{matrix}\right\},\ i=1,2,..,N_b \tag{4.37}$$

where N_b is the number of buses, and $Q_{g\,i}$ is the scheduled reactive power at bus *i*. The nodal active and reactive constant power loads are represented by P_{li} and Q_{li}, respectively. $\sum_{j\in i}$ is the set of nodes adjacent to node *i*, whilst $P_{inj\,i\,j}^{t_0}$ and $Q_{inj\,i\,j}^{t_0}$ are active and reactive power flows injected at bus *i*, given by [Acha et al., 2004],

$$P_{inj\,ij}^{t_0}=V_i^{t_0}V_j^{t_0}\left(G_{ij}Cos(\theta_i^{t_0}-\theta_j^{t_0})+B_{ij}Sin(\theta_i^{t_0}-\theta_j^{t_0})\right)+\left(V_i^{t_0}\right)^2G_{ii} \tag{4.38}$$

$$Q_{inj\,ij}^{t_0}=V_i^{t_0}V_j^{t_0}\left(G_{ij}Sin(\theta_i^{t_0}-\theta_j^{t_0})-B_{ij}Cos(\theta_i^{t_0}-\theta_j^{t_0})\right)-\left(V_i^{t_0}\right)^2B_{ii} \tag{4.39}$$

where V_k and θ_k are the voltage magnitude and angle at node *k* (*k=i,j*). $G_{ij}+jB_{ij}$ is the transfer admittance between bus *i* and *j*.

The constant voltage E_i behind the direct axis transient reactance $X_{di}^{'}$, as well as the initial conditions $\delta_i^{t_0}$ and $\omega_i^{t_0}$ for the rotor angle and speed, respectively, are obtained by means of the following constraint set [Sauer and Pai, 1998; Gan et al., 2000],

$$I^{t_0}(\cdot)=\left\{\begin{matrix} E_iV_i^{t_0}Sin(\delta_i^{t_0}-\theta_i^{t_0})-X_{d\,i}^{'}P_{mi}^{t_0}=0, \\ E_iV_i^{t_0}Cos(\theta_i^{t_0}-\delta_i^{t_0})-\left(V_i^{t_0}\right)^2-X_{di}^{'}Q_{gi}^{t_0}=0, \\ \omega_i^{t_0}=\omega_s \end{matrix}\right\},\ i=1,2,..,N_g \tag{4.40}$$

where V_i and θ_i are the voltage magnitude and angle at the i^{th} generation bus.

Physical and operating limits constrain the practical steady state operation of power systems. Some of these limits are mathematically described by [Acha et al., 2004],

$$H^{t_0}(\cdot)=\left\{\begin{matrix} \underline{Q}_{gi}^{t_0}\le Q_{gi}^{t_0}\le\overline{Q}_{gi}^{t_0}, \\ \underline{V}_j^{t_0}\le V_j^{t_0}\le\overline{V}_j^{t_0} \end{matrix}\right\}\begin{matrix} i=1,2,..,N_g, \\ j=1,2,..,N_b \end{matrix} \tag{4.41}$$

For preventive transient stability control, one of the most important control variables is the generator scheduled mechanical power input. This control variable is bound by power plant design limits, given by [Acha et al., 2004],

$$U=\left\{\underline{P}_{mi}^{t_0}\le P_{mi}^{t_0}\le\overline{P}_{mi}^{t_0}\right\},i=1,2,..,N_g \tag{4.42}$$

4.3.4. Dynamic constraints

The following equations comprise the dynamic state constraint sets,

The power flow mismatch equations regarding the transient state are modeled by the following constraint set [Sauer and Pai, 1998],

$$G(\cdot)=\left\{\begin{matrix} P_{ei}^{t}-P_{lG\,i}^{t}-\sum_{j\in i}P_{inj\,i\,j}^{t}=0, \\ Q_{ei}^{t}-Q_{lB\,i}^{t}-\sum_{j\in i}Q_{inj\,i\,j}^{t}=0 \end{matrix}\right\}, \begin{matrix} t\in T \\ i=1,2,..,N_b \end{matrix} \tag{4.43}$$

where terms P_{lGi} and Q_{lBi} correspond to the active and reactive load powers, formulated by (4.44). P_{ei} and Q_{ei} are the active and reactive electric power output of the generator, respectively, described by (4.45). $P_{inj\,i\,j}^{t}$ and $Q_{inj\,i\,j}^{t}$ are active and reactive power flows injected at node *i* at each time step of the transient state, given by (4.46)-(4.47) [Sauer and Pai, 1998].

$$P_{lGi}^{t}=P_{li}^{t_0}\left(\frac{V_i^t}{V_i^{t_0}}\right)^2;\ Q_{lBi}^{t}=Q_{li}^{t_0}\left(\frac{V_i^t}{V_i^{t_0}}\right)^2 \tag{4.44}$$

$$P_{ei}^{t}=\frac{E_i V_i^t}{X_{di}^{'}}Sin(\delta_i^t-\theta_i^t);\ Q_{ei}=\frac{E_i V_i^t}{X_{di}^{'}}Cos(\theta_i^t-\delta_i^t)-\frac{\left(V_i^t\right)^2}{X_{di}^{'}} \tag{4.45}$$

$$P_{inj\,ij}^{t}=V_i^t V_j^t\left(G_{ij}Cos(\theta_i^t-\theta_j^t)+B_{ij}Sin(\theta_i^t-\theta_j^t)\right)+\left(V_i^t\right)^2 G_{ii} \tag{4.46}$$

$$Q_{inj\,ij}^{t}=V_i^t V_j^t\left(G_{ij}Sin(\theta_i^t-\theta_j^t)-B_{ij}Cos(\theta_i^t-\theta_j^t)\right)-\left(V_i^t\right)^2 B_{ii} \tag{4.47}$$

where δ_i is the state variable that represents the rotor angle of the generator at time *t*.

In addition to the power flow mismatch equations, the generator swing equations must be formulated as difference constraints according to (4.33). Considering the synchronous reference frame this set is given by [La Scala et al., 1998; Gan et al., 2000; Yuan et al., 2003],

$$\varphi(\cdot)=\left\{\begin{matrix} \delta_i^t-\delta_i^{t-\Delta t}-\frac{\Delta t}{2}\left(\Delta\omega_i^t+\Delta\omega_i^{t-\Delta t}\right), \\ \omega_i^t-\omega_i^{t-\Delta t}-\frac{\Delta t}{2M_i}\left(\left[P_{mi}^{t_0}-P_{ei}^{t}-D_i(\Delta\omega_i^t)\right]+\left[P_{mi}^{t_0}-P_{ei}^{t-\Delta t}-D_i(\Delta\omega_i^{t-\Delta t})\right]\right) \end{matrix}\right\}\begin{matrix} ,t\in T, \\ i=1,2,..,N_g \end{matrix} \tag{4.48}$$

where M_i is the moment of inertia (s^2/rad) and D_i represents the constant damping for the *i-th* generator. ω_i is the state variable that represents the rotor speed of the generator at time *t*.

4.3.5. Transient stability constraints

Transient stability constraints aim to represent the system transient stability boundary, such that the steady state operating point computed by TSC-OPF analysis lies inside this boundary. There are two main transient stability criterions used in the literature to represent stability constrains in global transient stability approaches; the first criterion is the dot product [La Scala et al., 1998] and the second is the rotor angle limit index [Gan et al., 2000].

The dot product criterion states that system stability is ensured as long as the dot product is less than zero in the whole study integration interval. Hence, the number of stability constraints formulated into the TSC-OPF model equals the number of integration time steps included into the optimization process.

The rotor angle stability index states that system stability is guaranteed if the angular deviation of each generator with respect to the center of inertia (COI) is less than a pre-specified threshold in the whole study integration interval. The rotor angle stability index can be formulated as a set of stability constraints $H(\cdot)$, given by [Gan et al., 2000]:

$$H(\cdot)=\overline{\delta}_i^t=\delta_i^t-\frac{\sum_{k=1}^{N_g}H_k\delta_k^t}{\sum_{k=1}^{N_g}H_k}\leq 100^\circ,\ t\in T;i=1,2,...,N_g \tag{4.49}$$

where N_g is the number of generators, H_k is the inertia constant (s) of the k^{th} generator and $\overline{\delta}_i^t$ is the i^{th} generator rotor angle with respect to the center of inertia (COI). According to (4.49), the number of stability constraints to be considered in the TSC-OPF model increases, and equals the number of integration time steps included into the optimization process times the number of generators N_g.

4.3.6. Generic algorithm for TSC-OPF global approaches

Preventive transient stability control global approaches, in its basic version, are comprised of three main components; conventional OPF (Chapters 2 and 3), time-domain simulation (Section 4.2) and TSC-OPF (Section 4.3) analysis, which interact as described below and illustrated in Fig. 4.4.

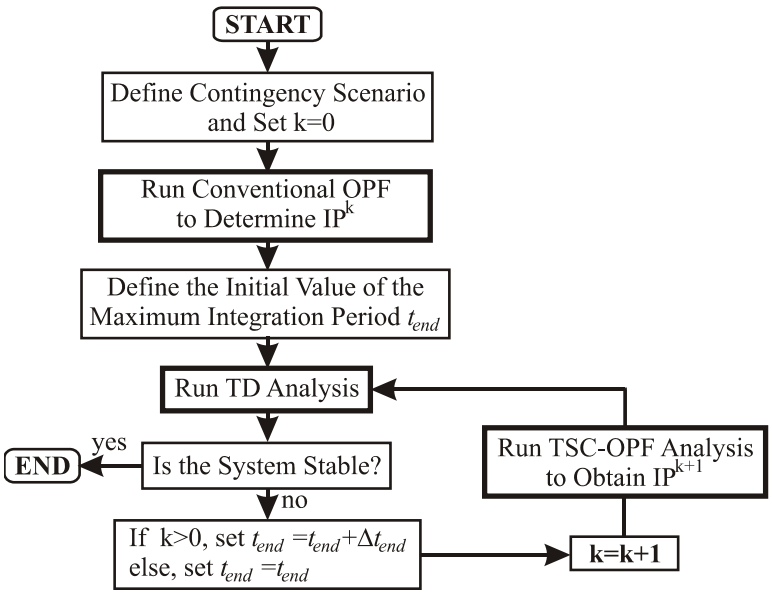

Fig. 4.4. Transient stability preventive control flow chart.

The conventional OPF is executed to determine an optimum initial steady state operating point IP^0. Then, it is convenient to run a time-domain analysis to verify if the credible contingency scenario to be considered into the TSC-OPF analysis makes the system transiently unstable. If this is the case, the TSC-OPF analysis is carried out considering the dynamic constraints that represent the system dynamics during the whole

time integration interval $T = [t_0, t_{cl}) \cup (t_{cl}, t_{end}]^k$, along with the transient stability constraints. The optimum steady state operating point IP^k given by this analysis might preventively ensure the system stability, but in order to make it sure, its transient stability is assessed using this point as an initial condition to carry out a new time-domain analysis. In this new time-domain analysis the system might hits stability limits after t_{end} (be unstable). This is because of the TSC-OPF analysis enforces stability constraints of the system dynamics within the time integration period *T*, thereafter the system trajectories (dynamics) could result unstable. If this is the case, the time integration period *T* is updated to a higher value of t_{end}, then the preventive stability control procedure goes to the next TSC-OPF analysis. This iterative procedure is carried out until the TSC-OPF analysis yields an optimum steady state operating point that ensures the system transiently stable, which is corroborated by TD analysis.

The objective function and steady state constraints involved in the TSC-OPF model are those considered in the conventional OPF model, whose solution procedure through the Newton-Based approach was explained in Chapter 2. Bearing this in mind, the Newton method can be readily applied to carry out the solution of the TSC-OPF model by representing the first and second derivatives of Lagrangian terms associated to the dynamic constraints into the linear system of equations given by (2.23), the first and second derivatives of Lagrangian terms associated to the dynamic constraints. It must be noted that these constraints are all equality constraints. On the other hand, the transient stability rotor index is formulated as an inequality constraint on variables (4.49), which can be handled by means of the Lagrangian Multiplier method explained in Section 2.2.4.

4.4. Conclusions

This Chapter presents theoretical bases for transient stability assessment and preventive control. Here, the Time Domain analysis is formulated in terms of power flow injections in polar form. In addition, the Time Domain model is expressed according to the Simultaneous Implicit model, which considers the Structure Preserving Model.

The theoretical information of global TSC-OPF is presented with the purpose of state the main reference frame of the proposed approaches derived from this research work.

It must be pointed out that all the previous models have been implemented in C++ computational programs using sparsity techniques. Results obtained by using these developed computational tools are presented implicitly in results obtained by the proposed transient stability control approaches, which are presented in following chapters.

Chapter 5

Transient Stability Constrained OPF-OMIB Based Global Approaches

This chapter deals with the SIME method and the proposed transient stability preventive control approaches.

Based on the assumption that the mechanism of loss of synchronism in a power system originates from the irrevocable separation of its machines into two groups, the SIME SIngle Machine Equivalent (SIME) method reduces the trajectories of a multi-machine system to the trajectory of a One Machine Infinite Bus (OMIB) equivalent [Pavella et al., 2000]. This reduced model makes it easy to carry out the transient stability preventive control because it is only necessary to stabilize one single trajectory, which represents the whole system, instead of each machine's trajectory. Based on this idea, it is proposed in this chapter that the OMIB equivalent derived by SIME can be used to carry out the transient stabilization process by a global TSC-OPF.

5.1. The SIME method

The SIngle Machine Equivalent (SIME) method belongs to the general class of transient stability methods which relies on a one-machine infinite bus (OMIB) equivalent. At difference with other method based on OMIB equivalents, SIME method uses the concept of generalized OMIB equivalent, which relaxes the coherency assumption among machines and considers detailed power system models. More precisely, it is a hybrid temporal-direct method, since it relies on the multi-machine system evolution with the time and the equal area criterion [Pavella et al., 2000].

There are two versions of the method, Emergency and Preventive SIME. The first uses real-time measurements collected on the system power plants, which are used by SIME to control the power system after a disturbance inception, so as to prevent loss of synchronism. In the preventive version, prior to the disturbance occurrence, the temporal information of the multi-machine power system is provided by a Time-Domain (TD) program [Pavella et al., 2000]. Here the preventive SIME is considered, and it is simply called as SIME.

The salient parameters of SIME method are; the determination of a One Machine Equivalent that represent a multi-machine system, the assessment of the very moment at which the system (in)stability occurs, and the computation of stability margins. These salient parameters have been accurately used to derive a preventive transient stability control sequential approach [Pavella et al., 2000; Ruiz-Vega and Pavella, 2003]. In this work, all information provided by SIME is used to derive two transient stability control global approaches based on a global formulation of the problem, and to reduce the computational burden associated to address the problem of computing a transiently stable optimal equilibrium point.

5.1.1. SIME foundations

The SIME method relies on the observation that the loss of synchronism of a multi-machine system originates from the irrevocable separation of system machines into two groups: one composed of the Critical Machines (*CMs*) responsible for the loss of synchronism, the other of the Non-critical Machines (*NMs)* [Pavella et al., 2000]. Based on time-domain (TD) simulations, SIME uses the physical parameters and time varying data of *CMs* and *NMs* to generate an OMIB equivalent system.

The transformation of the multi-machine system to an OMIB equivalent system is performed at each time step of the post-fault transient stability simulation by three main steps: i) Decomposition of the system machines into two groups of machines: *CMs* and *NMs*, ii) Representation of the two groups of machines by two single machines, and then by an OMIB equivalent, iii) Finally, the assessment of the transient stability condition of the multi-machine system by the Equal Area Criterion (EAC) on the OMIB equivalent system. More details about these steps are given in the following sections.

5.1.2. Identification of critical machines

The critical machines are those which cause the system loss of synchronism. To identify them, SIME drives the time domain transient stability program first in the during-fault, then in the post-fault configuration [Ernst et al., 2001]. To accomplish this task, at each time step of the post fault simulation, SIME sorts the machines according to their rotor angles, identifies the very first largest rotor angular distances between adjacent machines, and considers as candidate *CMs* those which are above each one of the (say, 5) largest distances, whilst the remaining machines are considered as candidate *NMs*. The procedure is carried out until a candidate group of *CMs* and corresponding OMIB reach the unstable conditions defined in Section 5.1.4. Each candidate OMIBs is uniquely represented by its parameters, which are derived from temporal information given by the TD simulation.

5.1.3. OMIB structure and time-varying parameters

Several decomposition patterns of the system machines into two candidate groups of critical and non-critical machines are constructed based on the previous *CMs* identification procedure [Pavella et al., 2000]. Each candidate group of machines is replaced by a single equivalent machine, whose equivalent angle and speed parameters are computed by aggregation as,

$$\delta_C(t)=(M_C)^{-1}\sum_{k\in C}\delta_k(t)M_k \tag{5.1}$$

$$\omega_C(t)=M_C^{-1}\sum_{k\in C}\omega_k(t)M_k \tag{5.2}$$

$$\delta_N(t)=(M_N)^{-1}\sum_{j\in N}\delta_j(t)M_j \tag{5.3}$$

$$\omega_N(t)=M_N^{-1}\sum_{j\in N}\omega_j(t)M_j \tag{5.4}$$

where the subscripts C and N refer to the group of critical and non-critical machines, respectively. The equivalent inertia coefficient of each candidate group of machines is given by,

$$M_C=\sum_{k\in C}M_k \tag{5.5}$$

$$M_N=\sum_{j\in N}M_j \tag{5.6}$$

where $k\in C$ and $j\in N$ defines the critical and non-critical machines of a candidate group. $M_i(i=k,j)$ is the moment of inertia of the i^{th} generator.

A candidate OMIB's equivalent structure is computed from each one of the defined decomposition patterns, and its parameters are calculated from the corresponding individual machines parameters by [Pavella et al., 2000],

$$\delta(t)=\delta_C(t)-\delta_N(t) \tag{5.7}$$

$$\omega(t)=\omega_C(t)-\omega_N(t) \tag{5.8}$$

Lastly, the candidate OMIB equivalent inertia coefficient M, electrical power P_{ei} and mechanical power P_m parameters are computed by,

$$M=\frac{M_C M_N}{M_C+M_N} \tag{5.9}$$

$$P_e(t)=M\left[M_C^{-1}\sum_{k\in C}P_{ek}(t)-M_N^{-1}\sum_{j\in N}P_{ej}(t)\right] \tag{5.10}$$

$$P_m(t)=M\left[M_C^{-1}\sum_{k\in C}P_{mk}(t)-M_N^{-1}\sum_{j\in N}P_{mj}(t)\right] \tag{5.11}$$

Each candidate OMIB is verified to be the critical OMIB according with the unstable condition given in the following section.

5.1.4. Stability conditions and margins

The severity of a fault scenario can be assessed in terms of the stability margin, which is stated by the EAC criterion as the excess of the decelerating over the accelerating area of the $\delta-P$ plane:

$$\eta = A_{dec} - A_{acc} \tag{5.12}$$

Accordingly, the OMIB equivalent system, and hence the multi-machine system, is stable if $\eta>0$, and unstable if $\eta<0$. The stability margin η is computed in accordance with the following procedure.

From the whole set of candidate OMIBs, the first candidate that satisfies the instability condition is declared as the critical OMIB equivalent or simply the OMIB. This condition is fulfilled at the time to instability t_u where the electrical power curve $P_e(t)$ and the mechanical power curve $P_m(t)$ intersect each other. This condition is formulated mathematically by (5.13) and, once it is satisfied, SIME stops the TD simulation and computes the OMIB unstable margin as given by (5.14), where $\omega(t_u)$ is the rotor speed at t_u.

$$P_a(t_u) = P_m(t_u) - P_e(t_u) = 0 \;;\; \dot{P}_a(t_u) > 0 \tag{5.13}$$

$$\eta_u = -M\left(\omega(t_u)\right)^2 \big/ 2 \tag{5.14}$$

Since the OMIB equivalent system is obtained from a group of critical machines, it can only be derived for unstable cases. However, the OMIB stable condition (η>0) can be established by continuation of the less unstable OMIB equivalent [Pavella et al., 2000]. In this case, the OMIB equivalent is stable if the $P_e(t)$ curve returns before crossing the $P_m(t)$ curve at time to stability t_r and the return angle $\delta(t_r)$, where OMIB rotor speed $\omega(t_r)$=0, as stated by (5.15).

$$\omega(t_r) = 0 \;;\; P_a(t_r) = P_m(t_r) - P_e(t_r) < 0 \tag{5.15}$$

Once conditions (5.15) have been met, the stable margin is computed by (5.16), where $\delta(t_u)$ is the rotor angle at t_u obtained from the less unstable case, and $P_a(t_r)$ is the accelerating power at t_r.

$$\eta_{st} = \left|P_a(t_r)\right|\left(\delta(t_u) - \delta(t_r)\right)\big/ 2 \tag{5.16}$$

Due to the fact that stability conditions are tested at each time step of the TD simulation, once conditions (5.13) or (5.15) are satisfied, the simulation can be stopped, unless multi-swing instability phenomena are of interest. In this latter case, only conditions (5.15) are verified for the whole study time period *T*, which is usually set to a span of 10 to 20 seconds [Pavella et al., 2000; Kundur et al., 2004].

5.1.5. SIME sensitivity analysis

SIME sensitivity analysis provides a quantitative measure of the OMIB's stability margin η changes with respect to variations in a selected sensitivity parameter p_s, such as clearing time or an OMIB's parameter. Based on this analysis it is possible to set guidelines to drive the system dynamics toward a desired behavior, as proposed in the preventive transient stability control sequential approach [Pavella et al., 2000; Ruiz-Vega and Pavella, 2003].

It has been observed through numerous examples that there is a quasi-linear relationship between changes of η_u and variations of the fault clearing time t_{cl} or the OMIB mechanical power $P_m(t_0)$ [Pavella et al., 2000; Ruiz-Vega and Pavella, 2003], in this case $p_s = t_{cl}$ or $p_s = P_m(t_0)$.

Taking advantage of the quasi-linear relationship of η *vs* p_s, it is possible to make an accurate prediction of the value that p_s must have to achieve the system transient stability limit. This is carry out by performing successive linear extra- (inter-) polations

using the OMIB's parameters and stability margins values of two successive SIME simulations. The abovementioned stability limit search conventionally requires few linear extra- (inter-) polations. Arguably, its efficiency could be influenced by the choice of the perturbation length Δp_s on the sensitivity parameter p_s, but not its accuracy [Pavella et al., 2000].

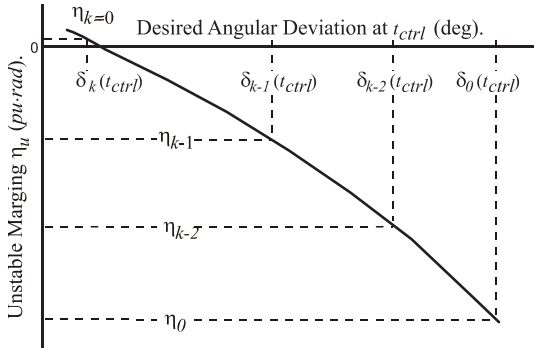

Fig. 5.1. Sensitivities behavior of OMIB stability margin η w.r.t. changes in $\delta(t_{crl})$.

Fig. 5.1 presents the sensitivity behavior of OMIB stability margin η, for a fixed fault clearing time t_{cl}, with respect to changes of the OMIB rotor angle deviation $\delta(t_{crl})$ at a given selected time step t_{ctrl}. It must be pointed out that t_{crl} is a fixed time at which the OMIB angular deviation δ is measured, and could be selected along the whole study time period T=[t_0,t_{end}], lasting from the initial simulation time step t_0 to the end of the study time period t_{end}. The behavior of $\eta \, vs \, \delta(t_{ctrl})$ is also shown to be quasi-linear in this figure. This relationship suggests that the system transient stability limit can be computed as a function of $p_s=\delta(t_{ctrl})$, by using the sensitivity $S_k(t_{ctrl})=\left.\frac{\Delta\eta}{\Delta p_s}\right|_{(t_{ctrl})}$ into a linear extra- (inter-) polations process.

In the successive extra- (inter-) polations process, the margin's sensitivity $S_k(t_{ctrl})$ is analytically represented by the slope of the linear function joining two successive points $\left(\eta_{k-1}, \delta_{(k-1)}(t_{ctrl})\right)$ and $\left(\eta_{k-2}, \delta_{(k-2)}(t_{ctrl})\right)$ computed by two successive SIME analysis. However, the following considerations should be taken into account in the computation of these points to assure that the sensitivity analysis is valid:

Both different angular deviations $\delta_{(k-1)}(t_{crl})$ and $\delta_{(k-2)}(t_{crl})$ are measured on two different equivalent trajectories $\delta_{(k-1)}$ and $\delta_{(k-2)}$, respectively, but at the same specified time step t_{ctrl} (see Fig. 5.2).

Equivalent trajectories $\delta_{(k-1)}$ and $\delta_{(k-2)}$ are uniquely defined by their respective initial operating points IP^{k-1} and IP^{k-2}, which also characterize the pre-disturbance state of the multi-machine system represented by these trajectories (see Fig. 5.2).

Equivalent trajectories $\delta_{(k-1)}$ and $\delta_{(k-2)}$ must to correspond to OMIBs that have the same *m*-swing structure: they are composed by the same groups of critical and non-critical

machines, and satisfy the condition of instability in the same *m*-swing instability. This means that the OMIBs assessed at the (*k-1*) and (*k-2*) SIME simulations have the same value of the equivalent inertia coefficient *M*, $M_{(k-1)} = M_{(k-2)}$.

Despite both OMIBs associated to $\delta_{(k-1)}$ and $\delta_{(k-2)}$ have the same *m*-swing structure, they are also uniquely defined by the two different steady state operating points IP^{k-1} and IP^{k-2}. This implies that the set of time-varying parameters along with the stability margin η associated to each OMIB have different values each other. Otherwise, both OMIBs dynamic responses given by trajectories $\delta_{(k-1)}$ and $\delta_{(k-2)}$ will be equal, such that the computation of the margin's sensitivity could yield indeterminate values since both $\Delta\eta$ and Δp_s would tend to zero.

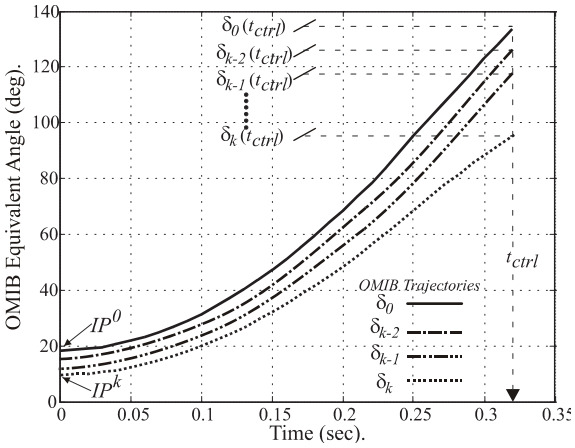

Fig. 5.2. OMIB angular trajectories and its deviation at t_{ctrl}.

The value of the margin sensitivity $S_k(t_{ctrl})$ at the k^{th} successive linear extra- (inter-) polation is then calculated as:

$$S_k(t_{ctrl}) = \left.\frac{\Delta\eta}{\Delta\delta}\right|_{t_{ctrl}} = \frac{\eta_{k-2} - \eta_{k-1}}{\delta_{(k-2)}(t_{ctrl}) - \delta_{(k-1)}(t_{ctrl})} \tag{5.17}$$

Based on (5.17), the desired value of the OMIB's rotor angle deviation $\delta_{sh\,k}(t_{ctrl})$ that might yield a null stability margin η_k =0 is given by:

$$\delta_{sh\,k}(t_{ctrl}) = \delta_{(k-1)}(t_{ctrl}) - \frac{\eta_{(k-1)}\left(\delta_{(k-1)}(t_{ctrl})\right)}{S_k(t_{ctrl})} \tag{5.18}$$

The points $\left(\eta, \delta(t_{ctrl})\right)$ can be predicted by using (5.17) and (5.18) in proposed TSC-OPF approach given in Section 5.5.

5.2. Approach I: OMIB reference trajectory TSC-OPF

This section presents the formulation of a new transient stability constraint. This constraint uses the OMIB equivalent constructed by SIME from the multi-machine system parameters. Based on this constraint the Approach I: OMIB reference trajectory TSC-OPF approach is performed. The proposed transient stability constraint is carried out from the observations given below.

5.2.1. Approach I: Stability constraint formulation

For any given unstable contingency scenario and Initial steady state operating Point (*IP*), the stabilization process aims to modify this point by considering stability limits that bound rotor angular deviations to maintain the system synchronism.

From the *IP* and contingency scenario, SIME simulations are carried out to compute the unstable and stable (critical) equivalent trajectories, considering the original fault clearing time t_{cl} and the computed critical clearing time (*CCT*), respectively, for the same OMIB composition. Recall that for the critical clearing time the system has a small positive stability margin. Based on transient stability concepts, the transient evolution of the unstable trajectory is always above the corresponding critical trajectory after clearing time, as shown in Fig. 5.3, where $\delta_{CT}(t_u)$ and $\delta_{UT}(t_u)$ are the rotor angles at to instability t_u on the stable and unstable trajectories, respectively.

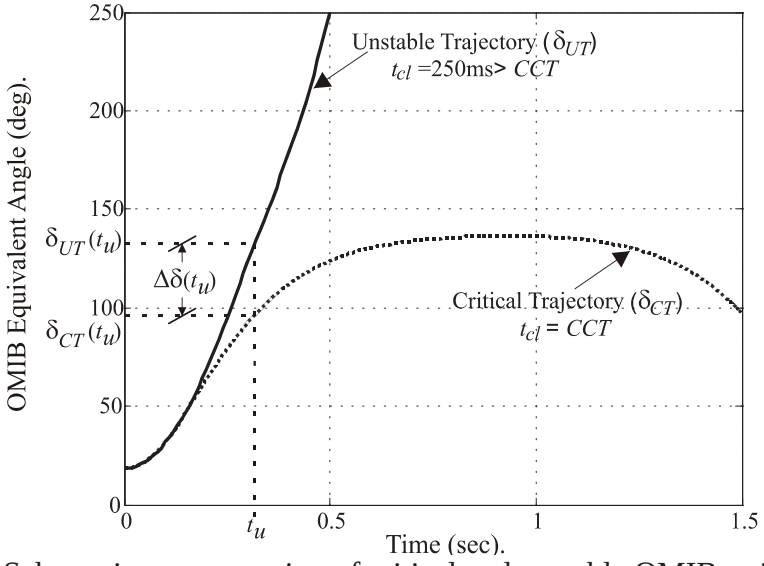

Fig. 5.3. Schematic representation of critical and unstable OMIB trajectories.

To reduce the instability degree, it is proposed that the stabilization process must be carried out at t_u, which is the time where the OMIB is identified. At this time, the stability of the OMIB will be guaranteed as long as its angular trajectory is bounded by the critical trajectory. Bearing this in mind, it is proposed to set the unstable trajectory deviation $\delta_{UT}(t_u)$ at the value of the critical trajectory $\delta_{CT}(t_u)$, such that the difference $\delta_{UT}(t_u)$ - $\delta_{CT}(t_u)$ must tend to zero. Based on this idea the transient stability constraint is set as

$$H(\delta_{CT}(t_u), \delta_{UT}(t_u)) = \Delta\delta(t_u) - T_h \leq 0 \tag{5.19}$$

where T_h is a desired deviation threshold (e.g. $1e^{-4}$), and $\Delta\delta(t_u) = abs(\delta_{UT}(t_u) - \delta_{CT}(t_u))$. $\delta_{CT}(t_u)$ is a scalar value corresponding to the angular deviation of the critical trajectory at t_u. The value $\delta_{CT}(t_u)$ is maintained fixed during the solution of the optimization process. On the other hand, $\delta_{UT}(t_u)$ is a function of the *CMs* and *NMs* variables described by (5.7), such that the rotor angles of the machines associated to both groups are variables during the optimization process to satisfy (5.19). The single explicit constraint (5.19) replaces the set of stability constraints represented by either (4.32) or (4.49).

5.2.2. OMIB reference trajectory stability constraint advantages

The simple inclusion of the proposed constraint (5.19) into the TSC-OPF model derives the following advantages w.r.t. the dot product criterion and the rotor angle stability index: 1) The control is performed in one equivalent trajectory at one single time step t_u, instead of controlling Ng trajectories at each time step as proposed in other formulations [Gan et al., 2000; Yuan et al., 2003; Xia and Chan, 2006]; 2) The rotor angle limits are not confined to a fixed value as proposed in [Gan et al., 2000]; 3) The time integration period in which the transient stability constraints must be included in the optimization process is defined from t_0 to t_u (i.e. $T = [t_0, t_{cl}) \cup (t_{cl}, t_u]$), such that the problem dimension is objectively defined, instead of selecting an arbitrary upper integration interval t_{end}, as proposed in [Gan et al., 2000; Yuan et al., 2003; Xia and Chan, 2006; La Scala et al., 1998]; 4) The generation re-dispatch is performed by the TSC-OPF.

Aforementioned advantages of the new proposed approach in the reduction of the programming problem size and complexity, with respect to the ones of approaches presented in [Gan et al., 2000] and [La Scala et al., 1998], are explicitly displayed in Table 5.1, where a direct size comparison between the different approaches is performed.

Table 5.1. Size comparison between the Approach I and other approaches

	Gan et al., 2000	**La Scala et al., 1998**	**Approach I**
Upper integration period t_{end}	Arbitrary t_{end}	Arbitrary t_{end}	**Not arbitrary t_u**
Number of integration steps	Arbitrary $N_{sa}=(t_{end} - t_0)/\Delta t$	Arbitrary $N_{sa}= (t_{end} - t_0)/\Delta t$	**Not arbitrary $N_{sb} = (t_u - t_0)/\Delta t$**
Number of transient stability constraints	$N_g * N_{sa}$	N_{sa}	**1**
Number of dynamic constraints	$(2Nb+2Ng)*N_{sa}$	$(2Nb+2Ng)*N_{sa}$	$\mathbf{(2Nb+2Ng)*N_{sb}}$
Heuristic stability criterion	Yes	No	**No**

It must be pointed out that the same number of prefault steady state constraints of Section 4.3.3 is employed in the formulation of all approaches reported in this table. However, the number of transient stability constraints of equation (4.32) is reduced to a single constraint in the new proposed approach, whilst it depends on the upper integration interval t_{end} in [Gan et al., 2000; La Scala et al., 1998], and is at least equal to the number of integration steps N_{sa} in [La Scala et al., 1998], or as large as N_{sa} times the number of generators N_g as in [Gan et al., 2000].

In addition, the proposed approach avoids arbitrariness of t_{end} of [Gan et al., 2000; La Scala et al., 1998] by setting $t_{end} = t_u$. This usually decreases the number of integration time steps to the minimum number of steps required to assess instability, objectively determined by SIME (normally, $t_u < t_{end}$ thus $N_{sb} < N_{sa}$) and therefore reduces the number of dynamic constraints of Section 4.3.4.

The stability of the system operating at the initial *IP* is improved once the TSC-OPF model formulated by (4.36)-(4.48) and (5.19) is solved, which yields a new steady state operating point. However, the complete contingency stabilization may not be achieved because the critical trajectory accurately describes the maximum angular deviations for the

initial equilibrium point *IP*, and not for the new equilibrium point (and additionally due to the nonlinearity of the problem). To verify that the new operating point is transiently stable, a stability analysis must be executed. As long as the system is not stable, it is necessary to compute the critical trajectory for the new operating point in order to update the stability inequality constraint (5.19) that must be considered in the next TSC-OPF analysis.

5.2.3. OMIB reference trajectory TSC-OPF algorithm

The proposed algorithm for preventive transient stability control readily derives from the foregoing discussion and is summarized below.

Step 1.- Run a conventional OPF to obtain an Initial operating Point (*IP*).

Step 2.-For the *IP* and given fault scenario, run a SIME simulation of the multi-machine system to analyze the transient stability of the OMIB equivalent system. If the stability condition is met, go to Step 8, or else determine the time t_u where the instability condition is met and go to Step 3.

Step 3.- On the Unstable Trajectory obtained in Step 2 determine the OMIB rotor angle deviation at t_u, $\delta_{UT}(t_u)$, then go to Step 4.

Step 4.- For the *IP* and fault scenario given in Step 2, run SIME to compute the critical clearing time *CCT* and the OMIB equivalent critical trajectory δ_{CT}. Find out the OMIB rotor angle deviation at t_u, $\delta_{CT}(t_u)$.

Step 5.- Formulate the transient stability constraint $H(\delta_{CT}(t_u), \delta_{UT}(t_u))$ given by (5.19)

Step 6.- Compute a new steady state operating point by solving the optimization problem described by (4.36)-(4.48) and (5.19) for the time integration interval $T=[t_0,t_{cl})\cup(t_{cl},t_u]$.

Step 7.- Replace the *IP* with the new operating point computed in Step 6, and go to Step 2.

Step 8.- The *IP* is the transiently stable operating point sought, such that the transient stability control has been achieved. **END.**

This proposed algorithm is applied for the purpose of present numerical examples, as given below.

5.3. OMIB reference trajectory TSC-OPF results

In order to illustrate numerically the prowess of the proposed approach to control the transient stability, the 3-machine 9-bus IEEE system [Sauer and Pai, 1998] and the 10-machine 39-bus New England system [Pai, 1989] are considered in the numerical examples, their corresponding data and one-line diagram are respectively shown in appendix B and C. It must be pointed out that these systems have been also used by other authors to exemplify their proposals [Gan et al., 2000; Nguyen and Pai, 2003]. The classical generator model is considered in both cases presented in this section. However, it is important to notice that the use of a simplified model is not a constraint imposed either by the approach, i.e. the TSC-OPF formulation [Gan et al., 2000] or SIME [Pavella et al., 2000], which may deal with any power system component model. All loads are modeled as constant powers in the steady-state stage and as constant impedances in the dynamic stage of the TSC-OPF. In all simulations transient period of simulation is t_u with integration time step of $0.01s$.

The design of the examples and the stability control results are given below.

5.3.1. Approach I: Three-Machine Nine-Bus system Results

For this system, the steady state voltage magnitude limits in pu for generation and load nodes are $1.00 \leq Vg \leq 1.06$ and $0.97 \leq Vg \leq 1.05$, respectively. The cost functions for generators and their ratings are given in Table 5.2. Taking into account these parameters and system's data given in Appendix B, the optimum initial operating point IP^0 is computed by a conventional OPF analysis (Step 1), and is shown in Table 5.3.

Table 5.2. Cost curves for 9-bus system

Node	**A** $\left(\frac{\$}{\text{hr}}\right)$	**B** $\left(\frac{\text{MVA}_\text{B}\$}{\text{MWhr}}\right)$	**C** $\left(\frac{\text{MVA}_\text{B}^2\$}{\text{MW}^2\text{hr}}\right)$	**Rating** (MW)
1	0.1	3.0	2.0	200
2	0.1	2.0	0.8	200
3	0.1	3.0	0.9	200

Table 5.3. Initial steady state operating point IP^0

Node	$\boldsymbol{V}$ (pu)	$\boldsymbol{\theta}$ (deg)	$\boldsymbol{P}_{m_{IP}}$ (MW)	$\boldsymbol{Q}_{g_{IP}}$ (MVAR)
1	1.05	0.000	50.19	23.66
2	1.05	11.104	171.60	13.05
3	1.04	7.153	98.62	-15.50
4	1.04	-1.510	0.00	0.00
5	1.01	-2.753	0.00	0.00
6	1.03	-2.389	0.00	0.00
7	1.05	5.536	0.00	0.00
8	1.04	2.778	0.00	0.00
9	1.05	4.120	0.00	0.00
Total Generation Cost			11.931 (*$/hr*)	

It is considered that the system operating in this first IP^0 is subjected to the contingency scenario defined by a solid three-phase fault, incepted at t_0=*0ms* at Node 7 and cleared at t_{cl}=*250ms* by tripping the line connecting the nodes 5-7. According to the proposed stabilization procedure, the next step is to carry out SIME analysis to assess the severity of the contingency scenario (Step 2). This analysis determines an unstable OMIB equivalent, where generators G2 and G3 are the critical machines, whilst G1 is a non critical machine. The OMIB instability condition was satisfied at t_{u1}=32*0ms* with an unstable angle of $\delta(t_{u1})$=133.797° and an unstable margin of η_{u1}=-1.592*pu·rad* (Step 3). The corresponding unstable trajectory is shown in Fig. 5.3.

Fig. 5.4 shows the contingency severity in terms of the excess of the accelerating area over the decelerating area in the δ-P plane. In order to find the critical stable trajectory, the extrapolation-based critical clearing time search is executed for the current IP^0, giving a value of CCT=138*ms*. Then, considering the composition of the previous unstable OMIB equivalent, the critical stable trajectory is calculated to assess its angular deviation at t_{u1}, which is $\delta_{CT}(t_{u1})$=96.790^o (Step 4). The angular deviations between the unstable and critical stable trajectories at t_{u1} is $\Delta\delta(t_{u1})$=37.01^o, as shown in Fig. 5.3, and then the transient stability constraint (5.19) is formulated (Step 5).

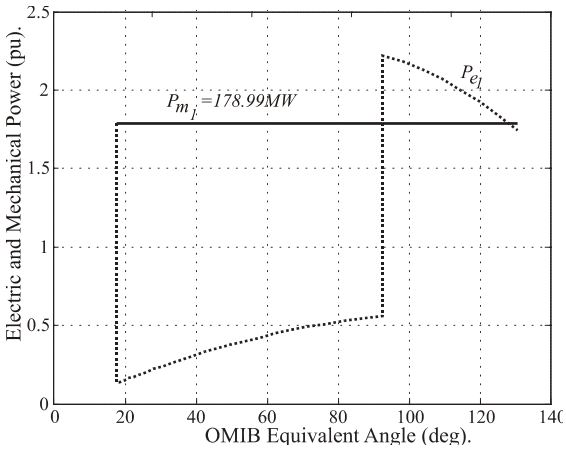

Fig. 5.4. $\delta - P$ Plane for the initial operating point.

Using these previous results, the proposed TSC-OPF approach is solved for the integration interval $T=[0,320ms]$. The solution of this optimization problem yields a second steady state point that satisfies static constraints, as given in Table 5.4 (Step 6).

Table 5.4. Second steady state operating point

Node	$\boldsymbol{V}$ (pu)	$\boldsymbol{\theta}$ (deg)	$\boldsymbol{P}_{m_{IP}}$ (MW)	$\boldsymbol{Q}_{g_{IP}}$ (MVAR)
1	1.02	0.000	85.87	2.53
2	1.06	5.057	130.83	16.74
3	1.05	4.024	102.21	-7.06
4	1.02	-2.725	0.00	0.00
5	1.00	-5.213	0.00	0.00
6	1.02	-4.348	0.00	0.00
7	1.05	0.832	0.00	0.00
8	1.04	-1.309	0.00	0.00
9	1.05	0.894	0.00	0.00
Total Generation Cost			12.343 (*$/hr*)	

The stabilization procedure goes to the next iteration considering the second steady state point as the new operating point of interest (Step 7). For this case, SIME analysis yields an unstable OMIB equivalent with the same composition of machines, i.e. G1 as *NM*, G2 and G3 as *CM*s, but satisfying the instability condition at $t_{u2}=710ms$. At this time, the unstable angle and stability margin are $\delta_{UT}(t_{u2})=145.646^{o}$ and $\eta_{u2}=-0.004$ $pu\cdot rad$, respectively. It must be observed that the unstable margin was reduced in 99.75 % with respect to the first iteration. The computation of the critical clearing time for this new initial operating point yields $CCT=249ms$, where the critical trajectory has $\delta_{CT}(t_{u2})=142.437^{o}$ at t_{u2}.

Based on previous SIME results, a TSC-OPF solution is now computed considering the integration interval $\boldsymbol{T}=[0,710ms]$, obtaining the third steady state point shown in Table 5.5. It must be pointed out that the mechanical power re-dispatching, w.r.t. the *IP* of Table 5.3, does not obey the criterion of always decreasing mechanical power in selected *CM* to

stabilize the system; the mechanical power of some *CM* could even be increased, in some cases, to find a more economical security re-dispatch, as in case of generator G3.

Table 5.5. Third steady state operating point

Node	V (pu)	θ (deg)	$P_{m_{IP}}$ (MW)	$Q_{g_{IP}}$ (MVAR)
1	1.06	0.000	86.42	23.45
2	1.05	5.321	128.07	3.86
3	1.04	4.607	104.30	-18.50
4	1.05	-2.567	0.00	0.00
5	1.02	-4.914	0.00	0.00
6	1.04	-4.011	0.00	0.00
7	1.05	1.156	0.00	0.00
8	1.04	-0.913	0.00	0.00
9	1.05	1.392	0.00	0.00
Total Generation Cost			12.367 (*$/hr*)	

The third steady state point is considered as the new operating point for SIME analysis in the procedure's second iteration. In this analysis, stable condition (5.15) is satisfied (see Fig. 5.5), and the stabilization procedure ends, after two iterations.

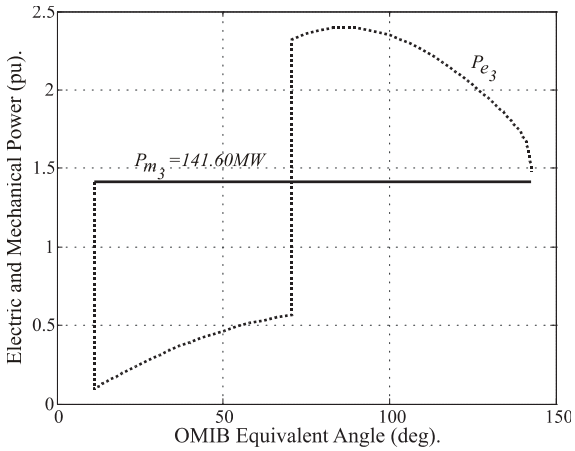

Fig. 5.5. $\delta - P$ Plane for the third operating point.

In this case, the stable stability margin is almost zero, and the OMIB equivalent stable trajectory is bound by the critical stable trajectory, as shown in Fig. 5.6. Lastly, the multi-machine swing curves are stable for the contingency scenario due to this transiently stable third steady state point satisfies static and dynamic security constraints, as shown in Fig. 5.7.

The clearing time used in this example (250 *ms*) is long in order to show that the proposed approach is able to stabilize the system in these demanding conditions. In the next section, the approach is tested using a more realistic clearing time.

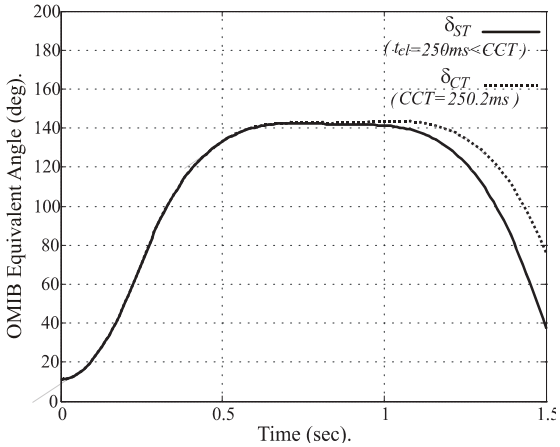

Fig. 5.6. Stable and critically stable OMIB trajectories at the third operating point.

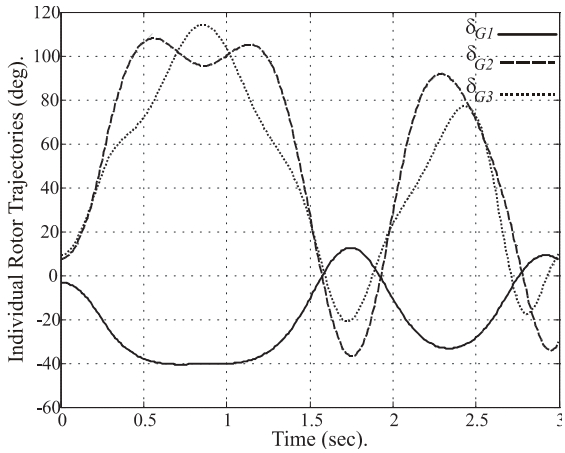

Fig. 5.7. Rotor angle trajectories at the third operating point.

5.3.2. Approach I: New England system Results

The data of this system were taken from [Pai, 1989], whilst generator ratings and quadratic generation cost curves are as reported [Nguyen and Pai, 2003], these data are shown in Appendix C. The active power load at bus 30 has been considered of 680 MW instead of the 628 MW given in Table C.IV. The steady state voltage magnitude limits in pu for generation and load nodes are $0.95 \leq V_g \leq 1.09$ and $0.95 \leq V_l \leq 1.09$. The initial operating point IP^1 computed by the OPF provides the optimum power dispatch given in Table 5.6.

Table 5.6. Initial OPF dispatch

Node	$\boldsymbol{P}_{m_{IP}}$ (MW)	$\boldsymbol{Q}_{g_{IP}}$ (MVAR)	**Node**	$\boldsymbol{P}_{m_{IP}}$ (MW)	$\boldsymbol{Q}_{g_{IP}}$ (MVAR)
30	244.03	-75.44	35	654.87	159.71
31	569.82	426.47	36	562.54	116.61
32	645.97	193.63	37	538.12	39.89
33	635.24	106.69	38	835.07	16.88
34	512.12	137.30	39	981.84	48.48
Total Generation Cost			61,558.0 (*$/hr*)		

Under those initial operating conditions, 92 contingences were ranked using SIME according to their corresponding *CCT*. This ranking shows that the most severe contingency is a solid three-phase fault applied at $t_0 = 0\,ms$ at Node 29 of the system, which is cleared by opening the line that connects nodes 28-29, with a *CCT*=62*ms*. We consider that the system protections operating time is t_{cl}*=100ms*, such that the system is transiently unstable for this most severe contingency scenario, and the proposed approach is applied to enhance the system stability under this contingency.

The first SIME analysis of the stabilization process is carried out to assess the OMIB equivalent. From the multi-machine system swing curves, drawn w.r.t. COA in Fig. 5.8, SIME analysis determines the time to instability t_{u1}*=430ms* and identifies generator at node 38 as the single *CM*. The unstable OMIB angular trajectory is also shown in Fig. 5.8, where the unstable angle and stability margin at t_{u1} are $\delta_{UT}(t_{u1})$*=113.784*° and η_{u1}*=-0.929pu ·rad*, respectively.

As already mentioned, for the initial power dispatch and contingency scenario, the system has a *CCT=62ms*, such that the OMIB critical trajectory has an angular deviation of $\delta_{CT}(t_{u1})$*=87.256*°, as shown in Fig. 5.8. Consequently, the stability constraint (5.19) is formulated and included into the TSC-OPF analysis, which yields an operating point IP^2 with a corresponding power dispatch shown in Table 5.7. For this IP^2 the multi-machine system is again subjected to the contingency scenario, but it is now transiently stable. The stable swing curves are shown with respect to COA in Fig. 5.9.

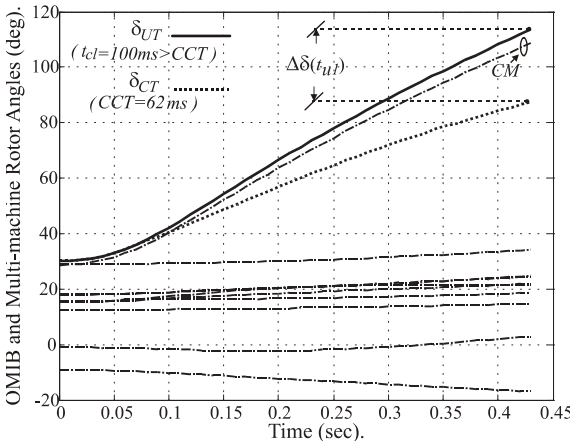

Fig. 5.8. Multi-machine and OMIB rotor angle trajectories for IP_1.

Table 5.7. TSC-OPF power dispatch for IP^2

Node	$\boldsymbol{P}_{m_{IP}}$ (MW)	$\boldsymbol{Q}_{g_{IP}}$ (MVAR)	**Node**	$\boldsymbol{P}_{m_{IP}}$ (MW)	$\boldsymbol{Q}_{g_{IP}}$ (MVAR)
30	249.51	-92.41	35	665.94	165.60
31	580.70	438.57	36	572.81	118.48
32	657.30	183.21	37	547.90	23.98
33	646.60	98.28	38	728.87	-4.35
34	520.37	150.54	39	1006.42	66.46
Total Generation Cost			61,660.8 (*$/hr*)		

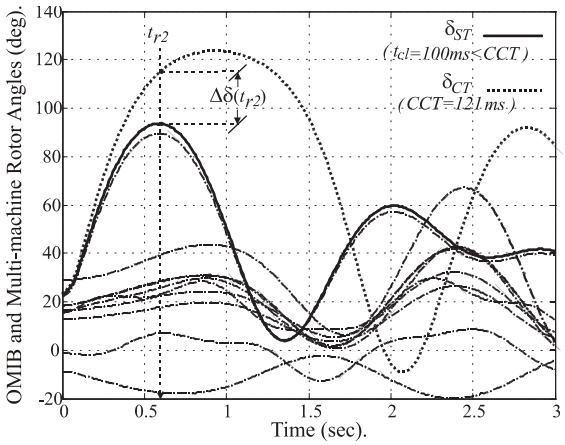

Fig. 5.9. Multi-machine and OMIB stable rotor angle trajectories for IP^2.

At Step 2, once stability condition (5.15) has been satisfied at time to stability t_r (for IP_2, t_{r2}=*590ms*), a last *CCT* computation might be carried out with SIME to assess how far the new system *CCT* is from the time of response of system protections.

In this case, the *CCT* is *121ms* for IP^2, i.e. *21ms* larger than the time response of system protections (*100ms*). This means that the contingency scenario has been over-stabilized. In order to get a transiently stable operating point nearer the stability boundary than IP^2, we formulate (5.19) at time t_r to decrease the angular deviation between the critical and stable trajectories, (δ_{CT}) and (δ_{ST}), both shown for IP^2 in Fig. 5.9, where $\delta_{ST}(t_{r2})=93.593^{\circ}$ and $\delta_{CT}(t_{r2})=113.784^{\circ}$. Therefore, the proposed stability constraint (5.19) and stabilization procedure are now a function of t_r, $\delta_{CT}(t_{r2})$ and $\delta_{ST}(t_{r2})$. At Step 5 the optimization process is carried out to obtain IP^3, whose power dispatch is displayed in Table 5.8.

Table 5.8. TSC-OPF power dispatch for IP^3

Node	$\boldsymbol{P}_{m_{IP}}$ (MW)	$\boldsymbol{Q}_{g_{IP}}$ (MVAR)	**Node**	$\boldsymbol{P}_{m_{IP}}$ (MW)	$\boldsymbol{Q}_{g_{IP}}$ (MVAR)
30	247.25	-99.93	35	66130	163.41
31	575.75	437.67	36	568.52	117.75
32	652.19	181.52	37	543.99	31.00
33	641.89	84.07	38	776.52	6.83
34	516.91	163.26	39	993.46	71.09
Total Generation Cost			61,589.6 (*$/hr*)		

The system operating at IP^3 and subjected to the contingency scenario is again unstable, and the instability condition is satisfied at t_{u3}=*710ms,* where the generator connected to node 38 remains as the single *CM*. At t_{u3} the angular deviation of the unstable trajectory is $\delta_{UT}(t_{u3})=112.722^{\circ}$ and the stability margin is η_{u3}=*-0.132 pu·rad* . For IP^3 the critical clearing time is *CCT=95ms*, such that the OMIB critical trajectory has an angular deviation of $\delta_{CT}(t_{u3})=114.151^{\circ}$. Consequently, the stability constraint (5.19) is newly formulated and included into the next optimization process, which yields the operating point IP^4 with a corresponding power dispatch shown in Table 5.9.

Table 5.9. TSC-OPF power dispatch for IP^4

Node	$P_{m_{IP}}$ (MW)	$Q_{g_{IP}}$ (MVAR)	Node	$P_{m_{IP}}$ (MW)	$Q_{g_{IP}}$ (MVAR)
30	247.89	-90.02	35	662.66	163.84
31	576.89	437.71	36	569.79	117.93
32	653.41	181.18	37	545.22	22.53
33	643.31	94.52	38	765.65	4.18
34	517.81	152.89	39	994.87	69.87
Total Generation Cost			61,602.1(*$/hr*)		

For IP^4 the contingency scenario has now *CCT=101ms*, which is very close to the time of the protections' response (*100ms*), the stabilization procedure ends. The stable swing curves are shown with respect to COA in Fig. 5.10, where generator connected to node 38 is still the most advanced one. It is observed that, in order to stabilize the harmful contingency scenario, the initial mechanical power of the critical generator connected to node 38 has been reduced in 8.3 %.

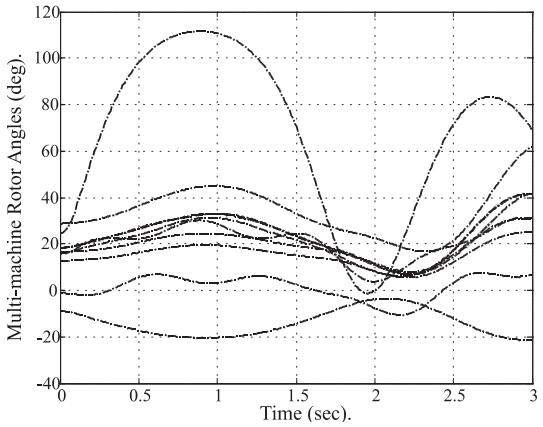

Fig. 5.10. Multi-machine rotor angle trajectories for IP^4.

5.4. Approach I: Comparison to other approaches

This section presents numerical comparisons of the results of the proposed approach with the ones of approaches reported by other authors considering the same systems analyzed in the last sections.

5.4.1. Approach I: Three-Machine, Nine-Bus system results comparison

System data are as given in Section 5.3.1, except the fuel cost parameters and rating of generators which are given in Table 5.10 [Nguyen and Pai, 2003]. The contingency scenario is defined by a solid three phase to ground fault at bus 7 applied at *t=0*, which is cleared by tripping line 7-5 at t_{cl}*=350 ms* with a *CCT*=291 *ms*.

Table 5.10. Cost curves for 9-bus system. Adopted from [Nguyen and Pai,2003].

Node	A $\left(\frac{\$}{\text{hr}}\right)$	B $\left(\frac{\$}{\text{MWhr}}\right)$	C $\left(\frac{\$}{\text{MW}^2\text{hr}}\right)$	Rating (MW)
1	140	2.0	0.006	200
2	120	1.5	0.0075	150
3	80	1.8	0.0070	100

Comparisons of power dispatches associated to the OPF base case and the final transiently stable operating point are given in Table 5.11 and Table 5.12, respectively. A trajectory sensitivity method is used in [Nguyen and Pai, 2003], whilst a differential evolution algorithm is used in [Cai et al., 2008], to reschedule power generation to ensure system stability. These comparisons show the effectiveness of the proposed approach because its solution yields a more economical generation cost than those reported in [Nguyen and Pai, 2003] and [Cai et al., 2008]. The reason of this result, despite the fact that [Cai et al., 2008] uses a global search method, is that the SIME stability criterion is able to avoid system's over-stabilization, as shown by comparing its final *CCT* (350.1 *ms*) w.r.t. that reported in [Cai et al., 2008] (398 *ms*, which is 13% above of the specified clearing time).

Table 5.11. Comparison of power dispatches for OPF base case of 9-bus system

Node	OPF Dispatch (MVA)		
	Nguyen and Pai, 2003	Cai et al., 2008	Approach I
1	106.19+j24.26	105.94+j17.14	**105.93+j17.28**
2	112.96+j0.37	113.04+j4.92	**113.05+j4.76**
3	99.20-j11.62	99.29-j15.31	**99.24-j15.53**
Cost (*$/hr*)	1132.59	1132.30	**1132.18**

Table 5.12. Comparison of transient stable power dispatches of 9-bus system

Node	OPF Dispatch (MVA)		
	Nguyen and Pai, 2003	Cai et al., 2008	Approach I
1	170.20+j27.31	130.94-j9.63	**121.55+j17.07**
2	48.94-j0.08	94.46+j9.22	**99.79+j4.00**
3	98.74-j9.86	93.09+j24.77	**96.57-j15.66**
Cost (*$/hr*)	1191.56	1140.06	**1135.2**

5.4.2. Approach I: New England system results comparison

In this section, the stabilization of the contingency scenario is defined by a solid three phase to ground fault at bus 29 applied at *t=0*, and cleared by tripping line 26-29 at t_{cl}*=100 ms*, which is longer than the initial system critical clearing time, and t_u=0.5s. System data are given in 5.3.2, but considering the original load data presented in Table C.IV of Appendix C. The results obtained by the current proposal are compared with those reported in [Layden and Jeyasurya, 2004]. The total cost and *CCT*s obtained by both TSC-OPF approaches are reported in Table 5.13.

Table 5.13. Comparison results for New England test system

Approach	Generation Cost (*$/hr*)	*CCT* (*ms*)
Approach I	60,916.8	107.1
Layden and Jeyasurya, 2004	61, 148.0	159.0

The proposed approach obtains the lowest cost and guarantees system stability with a *CCT* only 7% above the specified clearing time. On the other hand, a less economic and very conservative operation is reported in [Layden and Jeyasurya, 2004]. This is because the adopted transient stability constraint, based on the angular deviation of each generator w.r.t. the COI, results in an unnecessary large stability margin for this fault; i.e. the *CCT* is 59% above the specified clearing time. In addition (see Table 5.1), if t_{end} is arbitrarily defined for this system as 1.5*s*, and SIME finds t_u=0.5s, the number of dynamic plus stability constraints employed in the proposed formulation and in [Layden and Jeyasurya, 2004], for a time step Δt=0.01, are 4901 and 14850, respectively. These quantities of dynamic plus stability constraints clearly suggest that the proposed Approach I reduce the TSC-OPF problem size in a 70% w.r.t. that approach reported in [Layden and Jeyasurya, 2004]

5.5. Approach II: TSC-OPF using SIME sensitivity analysis

In Section 5.2.1 it was shown that for a given unstable scenario and a selected controlling time step t_{ctrl} along of the integration interval *T*, the multi-machine system stability can be enhanced by reducing at t_{ctrl} the angular deviation $\delta_{UT}(t_{ctrl})$ of its unstable OMIB equivalent angular trajectory δ_{UT} w.r.t the critical stable trajectory deviation $\delta_{CT}(t_{ctrl})$, where both angular deviations are measured at the same controlling time t_{ctrl}. In other words, the multi-machine system represented by its unstable OMIB equivalent becomes more stable when at t_{ctrl} the angular excursion of its unstable OMIB equivalent $\delta_{CT}(t_{ctrl})$ is set to a lower reference value, as stated by constraint (5.19).

The aforementioned observation and the SIME sensitivity analysis of Section 5.1.5 are then considered to derive the so called TSC-OPF using SIME sensitivity analysis approach.

5.5.1. Approach II: Stability constraint formulation

The quasi-linear relationship between different points (η,$\delta(t_{ctrl})$) shown by the SIME sensitivity analysis (see Fig. 5.1), is used to predict the maximum value that the OMIB's angular trajectory deviation $\delta_{sh}(t_{ctrl})$ must have at a selected controlling time t_{ctrl}, so as to make its corresponding multi-machine system transiently stable (η_{sh}>0) for a specified unstable contingency scenario.

This quasi-linear relationship between different points (η,$\delta(t_{ctrl})$) implies the comparison among different stability margins η, which must be computed for the same multi-machine system operating at different steady state operating points *IP*, and from which the multi-machine system dynamics are uniquely represented by OMIBs having the same *m*-swing structure (see Section 5.1.5). Under these considerations, it is possible to perform the sensitivity computation of η in terms of $\delta(t_{ctrl})$, where the OMIB equivalent deviation $\delta(t_{ctrl})$ is assessed at any selected time step $t_{ctrl} \in T = [t_0, t_u]$ along the OMIB angle trajectories considered in the calculation.

Due to the OMIB's trajectories are uniquely defined by the initial operating point, their computation can be interpreted as the solution of an initial-value problem, where $\delta(t_0)= IP$ is the initial condition. The OMIB stable equivalent trajectory for this reason, could be used to define the stability index at any selected time step of the trajectory $t_{ctrl} \in T = [t_0, t_u]$, since it bounds at all times (see Fig. 5.2) other OMIB trajectories (for the same composition and m-swing) and therefore its stability properties, which define the transient stability properties of the multi-machine system, are independent of the selected controlling time t_{ctrl}. This important characteristic makes it possible to define the selected controlling time step as $t_{ctrl}=t_0$ in order to compute the margin's sensitivity and set up the stability constraint. In this way, the value of $\delta_{sh\,k}(t_0)$ that might yield a null stability margin η_k =0 is in accordance with (5.18) given by,

$$\delta_{sh\,k}(t_0) = \delta_{(k-1)}(t_0) - \frac{\eta_{(k-1)}\left(\delta_{(k-1)}(t_0)\right)}{S_k(t_0)} \tag{5.20}$$

Based on (5.20), the transient stability constraint (5.19) can be reformulated as,

$$H(\delta_{sh\,k}(t_0), \delta_{UT}(t_0)) = abs(\delta_{UT}(t_0) - \delta_{sh\,k}(t_0)) - T_h \leq 0 \tag{5.21}$$

where T_h is a desired deviation threshold (e.g. $1e^{-4}$), $\delta_{sh\,k}(t_0)$ is a scalar value assessed by (5.21). This value is maintained fixed during the solution of the optimization process. On the other hand, $\delta_{UT}(t_0)$ is a function of the *CMs* and *NMs* variables described by (5.7), such that the initial condition of the machines rotor angles associated to both groups are variables during the optimization process to satisfy (5.21).

It has been found that the length of the time domain simulation required to be considered to form the set of dynamic constraints depends on the controlling time t_{ctrl}. By imposing the stability constraint at $t_{ctrl}=t_0$, the TSC-OPF model becomes only a function of initial steady-state variables, so dynamic constraints (4.43)-(4.48) related to the time-domain simulation are no longer required to be included in the TSC-OPF formulation. Hence, the proposed TSC-OPF model is fully described by the objective function (4.36), steady-state constraints (4.37)-(4.42) and the single stability constraint (5.21).

The stability margin of the multi-machine system operating point IP^0, computed at iteration $n=0$ of the stabilization process, is improved once the new proposed TSC-OPF model is solved, which yields a new, more stable, steady state operating point $IP^{n=k}$. It must be pointed out that contingency stabilization may not be achieved because the value of $\delta_{sh}(t_0)$ is obtained by considering that the margin's sensitivity has a strictly linear behavior. Hence, to verify that the new steady-state operating point $IP^{n=k}$ is transiently stable, SIME stability analysis must be performed. As long as the system is unstable, it is necessary to compute a new value of $\delta_{sh}(t_0)$ in order to update the stability constraint (5.21) that must be considered in the next TSC-OPF iteration, details of this fact are given below.

5.5.2. Assembling the transient stability constraint

It must be pointed out that (5.21) has to be firstly assembled before including it into the TSC-OPF problem. Hence, two successive points $\left(\eta_{k-1}, \delta_{(k-1)}(t_0)\right)$ and $\left(\eta_{k-2}, \delta_{(k-2)}(t_0)\right)$

should be computed. We consider that the first point $\left(\eta_{k-1}, \delta_{(k-1)}(t_0)\right)$ is scheduled based on the initial steady state operating point IP^{k-1} considered in the transient stability control procedure, such that η_{k-1} and $\delta_{(k-1)}(t_0)$ can be readily computed by simply running SIME analysis, as illustrated in Fig. 5.11. On the other hand, to assess the other point $\left(\eta_{k-2}, \delta_{(k-2)}(t_0)\right)$, at the first iteration of the stabilization procedure, the value of $\delta_{(k-2)}(t_0)$ is computed as,

$$\delta_{(k-2)}(t_0) = \delta_{(k-1)}(t_0) - \Delta\delta_{(k-1)}(t_0) \tag{5.22}$$

where $\Delta\delta_{(k-1)}(t_0)$ is a small increment on the previous OMIB angular deviation $\delta_{(k-1)}(t_0)$. Then the scalar value $\delta_{sh\ k}(t_0)$ is set to $\delta_{sh\ k}(t_0)$= $\delta_{(k-2)}(t_0)$, and is considered into (5.21). It must be noted that at this first step (5.21) is not by itself a stability constraint, but due to its inclusion into the TSC-OPF solution process, the initial unstable OMIB equivalent angular deviation $\delta_{UT}(t_0)$ is set to be $\delta_{(k-1)}(t_0)$, which consequentially yields a steady state operating point IP^{k-2}. Based on this point, SIME analysis is carried out to compute the stability margin η_{k-2}. With this information on hand, the sensitivity $S_k(t_0)$ and the first value $\delta_{sh1}(t_{ctrl})$ that might yield the system stable can be readily computed by (5.17) and (5.20), respectively, thus the stability constraint (5.21) can be now assembled, as shown in Fig. 5.11. When the stabilization procedure has passed the first iteration, the last two computed points namely (η_{k-1}, $\delta_{k-1}(t_0)$) and (η_{k-2}, $\delta_{k-2}(t_0)$) are considered to calculate $S_k(t_0)$ by (5.17), and the valued of $\delta_{sh\ k}(t_0)$ by (5.20), respectively to assemble constraint (5.21), as illustrated in Fig. 5.11.

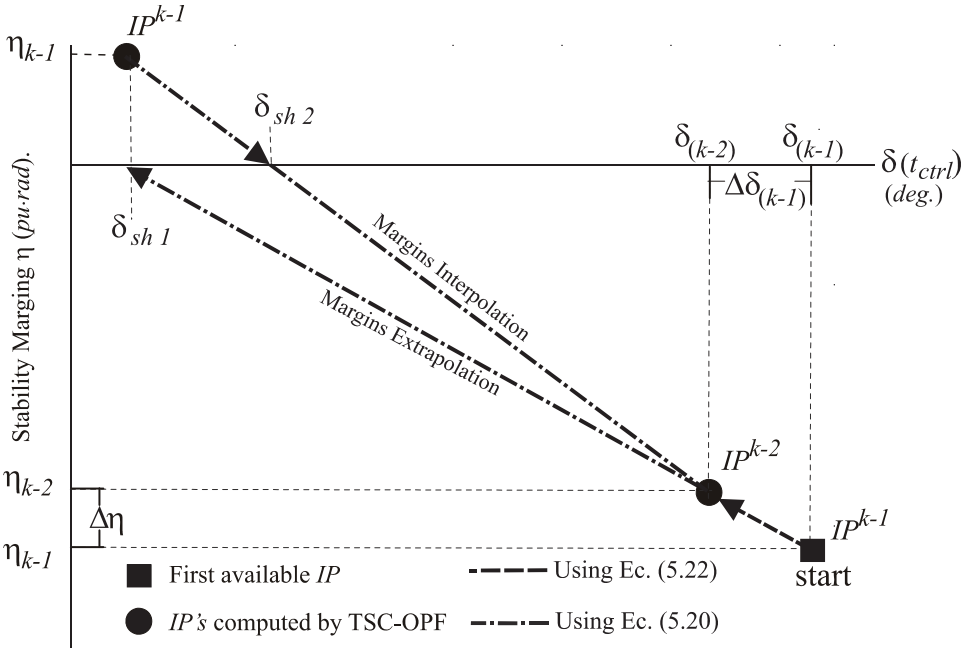

Fig. 5.11. Schematic process for assembling stability constraint (5.21).

The new proposed TSC-OPF approach readily derives from aforementioned observations and constraint (5.21), as given below.

5.5.3. Algorithm for TSC-OPF using SIME sensitivity analysis

Step 1.- Run a conventional OPF to obtain an base Initial operating Point (IP^0).

Step 2.- For the current iteration operating point IP^0 and fault scenario, run a SIME stability simulation of the multi-machine system to compute the OMIB's equivalent structure and determine the system stability. If the OMIB satisfies the stable condition, go to Step 8; else, determine the unstable margin η_u and obtain the OMIB's equivalent initial deviation $\delta_{UT}^{t_0}$ at t_0. Proceed to Step 3.

Step 3.- Determine an initial value of the OMIB angle stability limit δ_{sh} from $\delta_{UT}^{t_0}$ using $\delta_{sh} = \delta_{UT}^{t_0} - \lambda\delta_{UT}^{t_0}$, where λ represents a usually small decrement's percentage of $\delta_{UT}^{t_0}$ at t_0. λ is usually set to 0.1 and, if necessary, is changed as indicated in Steps 5 or 6. Set the iteration number n of the stabilization process as $n=1$.

Step 4.- Based on the structure of the last identified OMIB equivalent and of the computed value of the stability limit OMIB angle δ_{sh}, formulate the stability constraint (5.21), and solve the TSC-OPF model described by (4.36)-(4.42) and (5.21) to obtain a new, improved, initial operating point IP^n.

Step 5.- Starting from the new IP^n calculated at Step 4**,** run a SIME simulation to identify its corresponding OMIB equivalent system and to determine its stability condition. Two main cases could then be found:

5.1 If the stable condition (5.15) is met, compute the stable margin η_{stn} and the OMIB's initial deviation $\delta_{ST\,n}^{t_0}$ at t_0. If $\eta_{stn}<0.1 pu{\cdot}rad$ (a established stability tolerance), go to Step 8 or, if the stability margin is too conservative, the following two cases have to be considered;

a) The algorithm is at the beginning of the first iteration, $n=1$: set λ =0.5 λ and go to step 3.

b) The algorithm is at the beginning of the second or higher iteration: set $\eta_n=\eta_{stn}$ and $\delta_n^{t_0} = \delta_{ST\,n}^{t_0}$, then proceed to Step 6.

5.2 If the unstable condition (5.13) is met, compute the OMIB's initial rotor deviation $\delta_{UT\,n}^{t_0}$ and the unstable margin η_{un}; set $\eta_n=\eta_{un}$ and $\delta_n^{t_0} = \delta_{UT\,n}^{t_0}$, then proceed to Step 6.

Step 6.-If and only if the above computed pairs ($\delta_{UT}^{t_0}$**,** η_u) and ($\delta_n^{t_0}$, η_n) correspond to the same OMIB's *m*-swing structure, compute the new value of δ_{sh} that might make the system marginally stable by (5.20); then proceed to Step 7. Otherwise, set λ =0.05 and if the unstable condition (5.13) was met at Step 5, update $\delta_{UT}^{t_0} = \delta_n^{t_0}$ and $\eta_u = \eta_n$. Then go to Step 3.

Step 7.-If the unstable condition was satisfied in Step 5, update $\delta_{UT}^{t_0} = \delta_n^{t_0}$ and $\eta_u = \eta_n$ and increase the iteration counter as $n=n+1$, else, only increase $n=n+1$. Then go to Step 4.

Step 8.- The initial operating point is the transiently stable operating point sought, such that the transient stability control has been achieved. **END.**

At Step 3 of the proposed algorithm, the first desired value δ_{sh} is computed as a λ percentage of the unstable OMIB's initial angle condition $\delta_{UT}^{t_0}$. It must be pointed out that the λ percentage must be accurately selected so as to enforce a TSC-OPF solution in which the system is unstable or has a very small stable positive margin at Step 5. To accomplish this purpose, the proposed algorithm considers firstly λ=0.1 at Step 3; if the system is detected to be very stable at Step 5, λ is updated as λ=0.5λ and then the algorithm returns to step 3.

Lastly, the number of iterations required by the algorithm to reach convergence depends on the quasi-linear characteristic behavior of the OMIB unstable margin η_u with respect to the rotor angle initial condition $\delta_{UT}^{t_0}$; the closer the system behavior is to being linear, the less iterations are required. At any case, this quasi-linear characteristic behavior defines the algorithm's efficiency, but not the accuracy of results.

Despite the complexity that the algorithm seems to have, it is very efficient in terms of computational effort compared to other approaches, as inferred below.

5.5.4. TSC-OPF using SIME sensitivity constraint advantages

SIME method provides the possibility of representing the dynamics of a multi-machine system by means of the OMIB equivalent dynamics, which can be used to importantly reduce the programming size and complexity of conventional global TSC-OPF approaches [Gan et al., 2000] and [La Scala et al., 1998].

In this context, the transient stability constraint proposed in [Zárate-Miñano et al., 2010] is formulated based on the OMIB equivalent rotor angle derived by SIME, which allows a reduction of the number of constraints required to represent the system's stability limits into the TSC-OPF analysis, as displayed in Table 5.14. However, in order to importantly reduce the programming problem size and complexity, it is necessary to reduce the number of dynamic constraints to be considered into the TSC-OPF analysis. Approach I proposed in this work uses the OMIB equivalent to represent the system stability limits by only one single stability constraint. In addition, Approach I accurately assesses the length of the time integration interval to be considered into the TSC-OPF analysis by using SIME method, which substantially decreases the number of dynamic constraints, as displayed in Table 5.14.

Despite the advantages of Approach I, the proposed Approach II considers the OMIB equivalent and the SIME sensitivity analysis to formulate one single stability constraint and reduce to zero the number of dynamic constraints to be considered into the TSC-OPF analysis. These advantages of Approach II in the reduction of the programming problem size and complexity, with respect to Approach I and the ones presented in [Gan et al., 2000; La Scala et al., 1998; Zárate-Miñano et al., 2010], are explicitly displayed in Table 5.14. This table performs a direct size comparison between the TSC-OPF models associated with the different approaches; for the purpose of generality a system with "*Nb*" buses and "*Ng*" generators is considered.

Table 5.14. Size comparison between the Approach II, Approach I and other approaches

	Gan et al., 2000	**La Scala et al., 1998**	**Zárate-Miñano et al., 2010**	**Approach I**	**Approach II**
Upper integration period t_{end}	Arbitrary t_{end}	Arbitrary t_{end}	Arbitrary t_{end}	Not arbitrary t_u	Not arbitrary t_0
Number of integration steps	Arbitrary $N_{sa}=(t_{end} - t_0)/\Delta t$	Arbitrary $N_{sa}=(t_{end} - t_0)/\Delta t$	Arbitrary $N_{sa}=(t_{end} - t_0)/\Delta t$	Not arbitrary $N_{sb}=(t_u - t_0)/\Delta t$	Not arbitrary 0
Number of stability constraints	$N_g * N_{sa}$	N_{sa}	N_{sa}	1	1
Number of dynamic constraints	$(2Nb+2Ng)*N_{sa}$	$(2Nb+2Ng)*N_{sa}$	$(2Nb+2Ng)*N_{sa}$	$(2Nb+2Ng)*N_{sb}$	0
Heuristic stability criterion	Yes	No	No	No	No

5.6. TSC-OPF using SIME sensitivity analysis Results

In order to illustrate numerically the prowess of this second proposed approach to control the transient stability, the 3-machine 9-bus IEEE system [Sauer and Pai, 1998] and the 10-machine 39-bus New England system [Pai, 1989] already considered in Section 5.2 are newly focused in the further numerical examples, their corresponding system data parameters are given Appendix B and C, respectively. Additionally, this section presents a case study considering a reduced model of the Mexican power system. The system modeling details are as described in Section 5.2. It must be pointed out that some of the contingency scenarios given in that section are also considered here with the additional purpose of result comparisons.

The design of the examples and the stability control results applying this are given below.

5.6.1. Approach II: Three-Machine Nine-Bus system Results

The 3-machine 9-bus system is analyzed in this section to illustrate in detail how the multi-swing stabilization process is assessed by the proposed approach, by adjusting the generator's output power while satisfying the demand in the most economical manner. Generators are represented by the classical model and all loads by the constant impedance model. The transient period of simulation lasts from the time of fault inception t_0 to the time to instability t_u determined by the SIME method, with an integration time step of 0.01 s. For this study, the steady state voltage magnitude limits for all nodes are set to $0.95 \leq Vg \leq 1.05$ pu. The cost functions for generators and their ratings are given in Table 5.10. Taking into account these parameters and system data of Appendix B, the first initial steady state operating point IP^0 is computed by a conventional OPF study (Step 1), which gives the active power dispatch and generation cost reported in column 2 of Table 5.15.

A single credible contingency scenario with a critical clearing time *CCT*=291 *ms* is defined by a solid three-phase fault to ground at bus 7 applied at *t=0*, which is cleared by tripping line 7-5 at t_{cl}*=350 ms*, as reported in [Nguyen and Pai, 2003; Cai et al., 2008].

For this fault scenario and initial IP^0, a SIME simulation is performed (Step 2), which determines that the system is first-swing unstable with the critical generators connected at nodes 2 and 3, and the non-critical generator connected at node 1. The identification of this decomposition pattern of generators allows for representing the multi-machine system through a first-swing unstable OMIB equivalent, whose unstable margin and the rotor angle initial condition are η_u= -0.637*pu-rad* and $\delta_{UT}^{t_0} = 7.21°$, respectively.

In order to obtain the sensitivity of the stability margin with respect to changes in the rotor angle, the rotor initial condition $\delta_{UT}^{t_0}$ is decreased according with (5.22) by 10% (Step 3), which yields the scheduled value of $\delta_{sh} = 6.40°$. Row 1 of Table 5.16 summarizes the results of these initial steps.

The computed OMIB's unstable structure and scheduled value δ_{sh} are used to formulate the stability constraint (5.21), which is included in the TSC-OPF model to enforce the initial condition of the OMIB rotor angle to be the scheduled value δ_{sh} (Step 4). The solution of the TSC-OPF model yields the new operating point IP^1, whose active power dispatch and generation cost are given in column 3 of Table 5.15.

Table 5.15. Active power dispatches and generation costs for first swing stability control

Node	**Active Power Dispatch** (MW)				
	IP^0	IP^1	IP^2	IP^3	IP^4
1	105.93	109.97	115.48	116.41	117.07
2	113.05	110.50	107.05	106.50	106.10
3	99.24	97.65	95.60	95.29	95.08
Cost ($/hr)	1132.18	1132.37	1133.50	1134.03	1134.36

Table 5.16. Summary of the 9-bus system stabilization process

Iteration	**Computation of *IP's***	**OMIB's parameters**		**Assessment of δ_{sh}**	δ_{sh} (*deg*)	**Cost** (*$/hr*)
		η (*pu-rad*)	δ^{t_0} (*deg*)			
1	IP^0 (OPF)	-0.637	7.21	Eq. (5.22)	6.40	1132.18
	IP^1 (TSC-OPF)	-0.423	6.40	Eq. (5.20)	4.79	1132.37
2	IP^2 (TSC-OPF)	-0.099	4.79	Eq. (5.20)	4.20	1133.50
3	IP^3 (TSC-OPF)	-0.033	4.20	Eq. (5.20)	3.90	1134.03
4	IP^4 (TSC-OPF)	-0.004	3.90	Eq. (5.20)	3.80	1134.36
5	IP^5 (TSC-OPF)	-3.106	3.80	Eq. (5.22)	3.61	1134.48
	IP^6 (TSC-OPF)	+0.024	3.61	ENDS		1134.71

The stability of the system operating at the new point IP^1 is assessed by SIME method (Step 5), which revels that the previous first-swing unstable OMIB remains, but now the corresponding unstable margin is η_1= -0.423*pu-rad* and the rotor angle initial

condition is $\delta_1^{t_0} = 6.40°$. In this case unstable condition (5.13) described in Section 5.5.3 is satisfied.

Accordingly, the algorithm follows computing the pairs $(\delta_{UT}^{t_0}, \eta_u)$ and $(\delta_1^{t_0}, \eta_1)$, which correspond to the same first-swing OMIB's unstable structure. This makes it possible to use (5.20) in order to find, by extrapolation, the first schedule value δ_{sh} that might be associated with a positive margin (Step 6). This extrapolation calculates a value of δ_{sh} =4.79° as given in row 2 of Table 5.16. After updating the pair $(\delta_{UT}^{t_0}, \eta_u)$ with the values of $(\delta_1^{t_0}, \eta_1)$ (Step 7), the algorithm proceeds to the second iteration, starting at Step 4 as indicated in Section 5.5.3.

The active power dispatch and system generation cost corresponding to IP^2 computed by the TSC-OPF at this second iteration, as well as those related to the *IPs* computed at the third and fourth iterations, are reported in columns 4, 5, and 6 of Table 5.15, respectively. For all iterations, the same first-swing OMIB's unstable structure is obtained by using the SIME method. Similarly, the OMIB's stability properties and margin extrapolation parameters for the second, third and fourth iterations are reported in rows 3, 4, and 5 of Table 5.16, respectively.

At the fifth iteration, the last scheduled value δ_{sh} =3.80° is included in the stability constraint (5.21) of the TSC-OPF model to compute the operating point IP^5, whose power dispatch and generation cost are given in column 2 of Table 5.17. The SIME method is newly applied to assess system stability of point IP^5, and it is determined that the OMIB equivalent system has the same structure considered in all four previous iterations, but now the OMIB's instability condition is satisfied at the second-swing instead of the first-swing, as reported in [Zárate-Miñano et al., 2010].

Table 5.17. Multi-swing phenomena active power dispatches and generation costs

Node	**Active Power Dispatch** (MW)	
	***IP*^{5}**	***IP*^{6}**
1	117.38	117.62
2	105.91	105.78
3	96.96	94.90
Cost (*$/hr*)	1134.48	1134.71

The unstable margin at this second-swing instability is η_4=-3.106*pu-rad* and the initial rotor angle condition is $\delta_5^{t_0}$ =3.80°. Clearly, the pairs $(\delta_4^{t_0}, \eta_4)$ and $(\delta_5^{t_0}, \eta_5)$ do not correspond to the same *m*-swing instability, and therefore they can not be compared nor be extrapolated to calculate the next scheduled value δ_{sh}. However, this problem is not unsolvable because of the proposed algorithm is also valid for multi-swing instabilities.

In cases like these, where instability conditions of the last two iterations are satisfied in different swing numbers (in this case first and second-swing instabilities), the stabilization process must be only restarted at Step 3, starting from the last computed OMIB's structure and its stability information, and then the algorithm follows as described

in Section 5.5.3. Hence, the algorithm sets the pair $(\delta_{UT}^{t_0}, \eta_u)$ as $(\delta_5^{t_0}, \eta_5)$ at the fifth iteration, and then goes to Step 3 to compute the new scheduled value as δ_{sh}=3.80-(0.05)(3.80)=3.61° by evaluating (5.22), as reported in row 6 of Table 5.16. Then, the new equilibrium point IP^6 is computed by the TSC-OPF approach, which has the active power dispatch and generation cost reported in column 3 of Table 5.17. Lastly, the SIME method is applied to compute the transient stability margin of the system operating at IP^6, which results in a stable behavior with a margin of $\eta_6 = 0.024$*pu-rad*, as given in row 7 of Table 5.16. Hence, the system operating at point IP^6 is now secure from a transient stability viewpoint for the defined contingency scenario.

5.6.2. Approach II: New England system Results

Data of this system, generator ratings and quadratic generation cost curves are given in Appendix C. The steady state voltage magnitude limits in *pu* for generation and load nodes are $0.95 \le V_g \le 1.09$ and $0.95 \le V_l \le 1.07$. In this case study, the credible contingency scenario is defined by a solid three phase to ground fault at bus 29 applied at t=0*ms*, and cleared by tripping line 26-29 at t_{cl}=100 *ms*. Considering these system parameters, the proposed approach using conventional OPF firstly determines the Initial operating Point IP^0 (Step 1), whose complex power dispatch is shown in Table 5.18. According to SIME analysis (Step 2), the system operating at *IP* and subjected to the defined contingency scenario becomes unstable, where the machine at node 38 is the single critical machine *CM* whilst the remainder machines are non critical *NM*. The unstable OMIB equivalent is characterized by a rotor angle initial condition and an unstable margin of $\delta_{UT}^{t_0} = 29.92°$ and η_u = -0.552 *pu-rad*, respectively, as shown in row1 of Table 5.19.

Table 5.18. Initial operating point IP^0 of the New England system

Node	$\boldsymbol{P}_{m_{IP}}$ (MW)	$\boldsymbol{Q}_{g_{IP}}$ (MVAR)	**Node**	$\boldsymbol{P}_{m_{IP}}$ (MW)	$\boldsymbol{Q}_{g_{IP}}$ (MVAR)
30	242.00	-77.15	35	650.44	159.06
31	566.31	426.53	36	558.38	116.11
32	642.23	194.01	37	534.89	38.54
33	629.71	106.28	38	830.12	16.68
34	508.00	135.67	39	975.95	48.93
Total Generation Cost			60,892.3 (*$/hr*)		

Table 5.19. Stabilization process resume of the New England system

Iteration	**Computation of *IP's***	**OMIB's parameters**		**Assessment of δ_{sh}**	δ_{sh} (*deg*)	**Cost** (*$/hr*)
		η (pu-rad)	δ^{t_0} (*deg*)			
1	IP^0 (OPF)	-0.552	29.92	Eq. (5.22)	28.42	60,892.3
	IP^1 (TSC-OPF)	-0.229	28.42	Eq. (5.20)	27.36	60,896.6
2	IP^2 (TSC-OPF)	+0.021	27.36	ENDS		60,906.7

In order to determine the margin sensitivity of the previous OMIB w.r.t. its equivalent initial angular deviation $\delta_{UT}^{t_0}$ (Step 3), the schedule value is set as

δ_{sh} = 29.92-(0.05)(29.92)=28.42° (according to (5.22)), as given in row 1 of Table 5.19. Considering the unstable OMIB equivalent structure and the actual value of δ_{sh}, the stability constraint is formulated and included into the TSC-OPF analysis (Step 4). This analysis yields the operating point IP^1 whose complex dispatch is given in Table 5.20.

Table 5.20. Operating point IP^1 of the New England system

Node	$\boldsymbol{P}_{m_{IP}}$ (MW)	$\boldsymbol{Q}_{g_{IP}}$ (MVAR)	**Node**	$\boldsymbol{P}_{m_{IP}}$ (MW)	$\boldsymbol{Q}_{g_{IP}}$ (MVAR)
30	242.68	-82.06	35	651.94	161.17
31	568.51	429.97	36	559.73	116.36
32	644.43	200.66	37	535.96	38.05
33	631.19	111.34	38	809.18	15.44
34	509.27	132.51	39	984.31	38.23
Total Generation Cost			60,896.6 (*$/hr*)		

Based on this point IP^1 a second SIME analysis determines the system as unstable for the given contingency scenario (Step 5). For this case, the structure of the assessed unstable OMIB equivalent remains, the enforced rotor angle initial condition and the unstable margin are now $\delta_1^{t_0}$ =28.42° and η_1 = -0.229 *pu-rad*, respectively. Following with this first algorithm iteration, the extrapolation of the above computed pairs ($\delta_{UT}^{t_0}, \eta_u$) and ($\delta_1^{t_0}, \eta_1$) gives the OMIB initial rotor deviation that might make the system stable δ_{sh} = 27.36° (Step 6), given in row 2 of Table 5.19. Once computed δ_{sh} the algorithm goes to the second iteration (Step 7).

At the beginning of the second iteration, the algorithm updates the stability constraint with δ_{sh} = 27.36° and the last unstable OMIB equivalent structure (Step 4). The updated constraint is included into the TSC-OPF model, whose solution yields the operating point IP^2 with an economic power dispatch as given in Table 5.21. The SIME method is then used to assess the transient stability of the system operating at IP^2 and subjected to the defined credible contingency (Step 5). This analysis indicates that the system is stable for these operating conditions with a margin of η_1 =+0.021*pu-rad*, which is less than the maximum threshold defined as 0.1 *pu-rad* and therefore the algorithm ends at only two iterations, as shown in row 3 of Table 5.19. The steady state operating point IP^2 satisfies steady state operation and economic requirements, whilst system subjected to the contingency scenario remains transiently stable. The resulting stable swing curves w.r.t. COI are shown in Fig. 5.12, where the machine at node 38 remains the most advanced one due to the small positive stability margin of the system.

Table 5.21. Operating point IP^2 of the New England system

Node	$\boldsymbol{P}_{m_{IP}}$ (MW)	$\boldsymbol{Q}_{g_{IP}}$ (MVAR)	**Node**	$\boldsymbol{P}_{m_{IP}}$ (MW)	$\boldsymbol{Q}_{g_{IP}}$ (MVAR)
30	243.24	-73.17	35	653.15	163.66
31	570.24	429.4	36	560.84	116.81
32	646.14	197.11	37	536.88	40.81
33	632.38	116.41	38	792.43	10.63
34	510.29	129.89	39	991.00	28.49
Total Generation Cost			60,906.7(*$/hr*)		

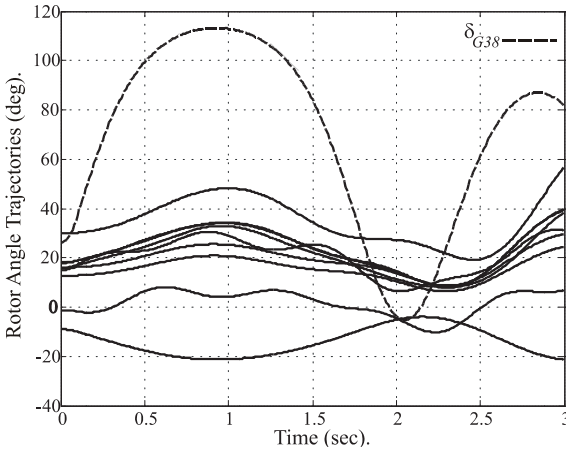

Fig. 5.12. Stable angular trajectories for New England system.

5.6.3. Approach II: 46-machine, 190-bus Mexican power system

The Mexican Interconnected System (MIS) covers a vast geographical area stretching interconnections from the southern border with Central America to its northern border with the USA. The MIS consists of eight operating regions, where 7 of these regional systems, referred to as north-western (NW), northern (N),north-eastern (NE), western (W), central (C), south-eastern (SE) and peninsular (P) systems, are interconnected to operate as a multi-area system as shown in Fig. 5.13 [Messina et al., 2002]. Main loads are located in the largest metropolitan areas of the country, namely Mexico City in the central system, Guadalajara city in the western system, and Monterrey city in the north-eastern system. Under normal operating conditions, the power flows from the north to the south systems, from the peninsular to the south-eastern system and from the south to the central system, respectively. However, given the longitudinal structure of these sparsely connected transmission paths, voltage and transient stability problems are acute and of prime importance.

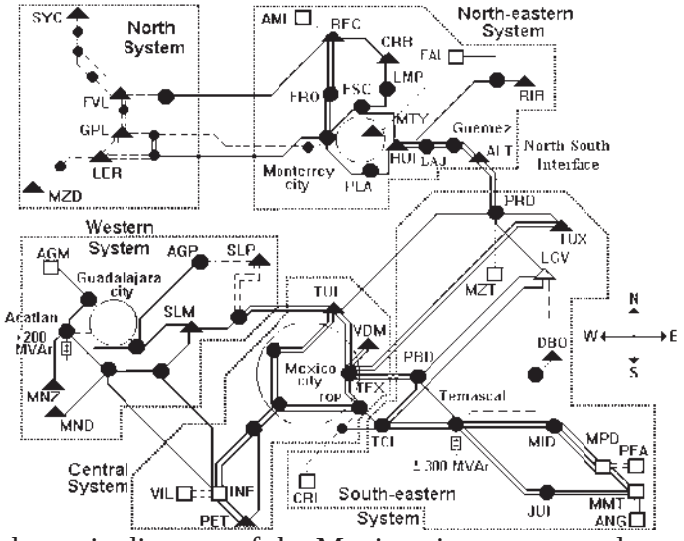

Fig. 5.13. Schematic diagram of the Mexican interconnected power system.

The proposed approach is applied on a reduced MIS model comprised by the northern, north-eastern, western, central and south-eastern areas. This equivalent consist of

190 buses, 46 generators, 90 loads and 265 transmission lines operating at voltage levels ranging from 400 kV to 115 kV. The study scope consists of computing a transiently stable optimal equilibrium point associated to the considered credible contingency scenario defined by a three-phase solid fault at bus 182, incepted at t=0*ms* and cleared at t_{cl}=150*ms* by tripping the line connecting nodes 182 and 186.

The analysis starts following the proposed approach, such that a conventional OPF analysis is carried out to assess the steady state system conditions (Step 1). This analysis yields an optimum steady state equilibrium point IP^0 with total generation cost of 21120.7*$/hr*, as shown in first row of Table 5.22.

Table 5.22. Stabilization process of the Mexican system with the Proposed Approach II

Iteration	**Computation of *IP's***	**OMIB's parameters**		**Assessment of δ_{sh}**	δ_{sh} (*deg*)	**Cost** (*$/hr*)
		η (*pu-rad*)	δ^{t_0} (*deg*)			
1	IP^0 (OPF)	-1.044	43.44	(5.22)	39.00	21,120.7
	IP^1 (TSC-OPF)	-0.426	39.00	(5.20)	35.90	21,122.2
2	IP^2 (TSC-OPF)	-0.069	35.90	(5.20)	35.30	21,123.6
3	IP^3 (TSC-OPF)	**+0.057**	35.30	**ENDS**		**21,122.7**

The steady state voltage profile and the active power dispatch corresponding to IP^0 are depicted in Fig. 5.14 (*a*) and (*b*), respectively. In order to assess the system transient stability at the operating point IP^0 with the defined contingency scenario, SIME analysis is executed (Step 2). This analysis determines that the system is transiently unstable, and therefore unsecure under that credible contingency. In this case, there are 16 critical machines producing the lost of synchronism and 30 noncritical-machines, as illustrated in Fig. 5.15. These two groups of machines compose the unstable OMIB equivalent assessed by SIME, whose initial angular deviation at t_0 is $\delta_{UT}^{t_0} = 43.44°$ and the unstable margin is η_u = -1.044 *pu-rad*, as reported in row 1 of Table 5.22.

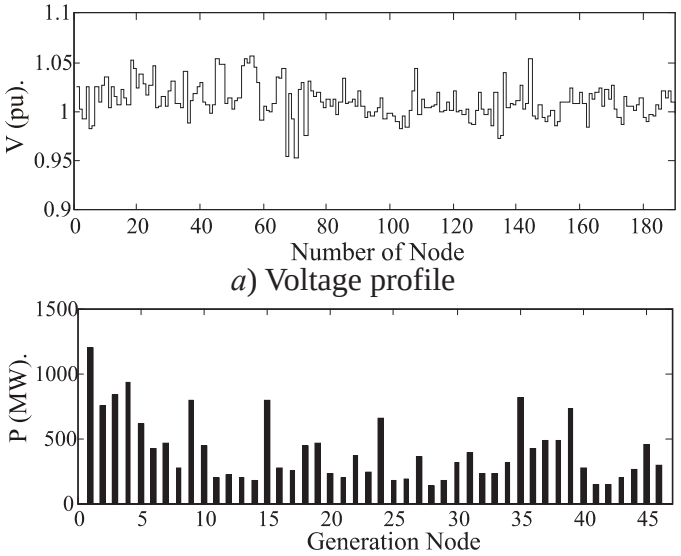

a) Voltage profile

b) Active power dispatch

Fig. 5.14. Initial steady state equilibrium point IP^0 of the Mexican system.

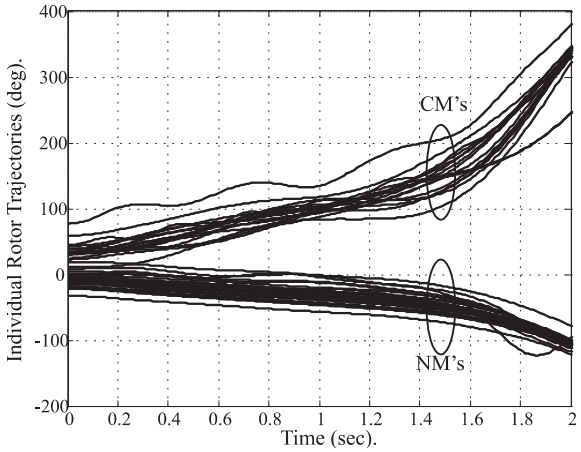

Fig. 5.15. Unstable angular trajectories for the Mexican system initially operating at IP^0.

In order to determine the OMIB equivalent margin sensitivity versus its angular deviation at t_0 (Step 3), the initial angular deviation $\delta_{UT}^{t_0}$ is used to compute δ_{sh} according to (5.22) as $\delta_{sh} = 43.44\text{-}(0.10)(\ 43.44) = 39.00°$, which is also reported in row 1 of Table 5.22.

The Algorithm uses this computed value of δ_{sh} and the last computed unstable OMIB structure to assemble the stability constraint (Step 4). This constraint is considered in the TSC-OPF model, which is solved to compute the new steady state equilibrium point IP^1. This equilibrium point is considered into the next SIME analysis, where the OMIB equivalent satisfies the unstable condition (Step 5). In this case the unstable margin is $\eta_1 = -0.426$*pu-rad* and the corresponding initial angular deviation is $\delta_1^{t_0} = 39.00°$, as reported in row 2 of Table 5.22.

The values $(\delta_{UT}^{t_0}, \eta_u)$ and $(\delta_1^{t_0}, \eta_1)$ computed at Steps 2 and 5 are linearly extrapolated to determine the scheduled value that should make the system stable, which yields $\delta_{sh} = 35.90°$, as reported in row 2 of Table 5.22 (Step 6). The algorithm goes to the second iteration, where the stability constraint is updated with the last computed value of δ_{sh}=35.90°, and solves the TSC-OPF model. The solution of this model yields the equilibrium point IP^2, where the system is newly assessed as unstable, with its unstable margin of $\eta_2 = -0.069$ pu-*rad* and an angular deviation of $\delta_2^{t_0} = 35.90°$, as reported in row 3 of Table 5.22. Similarly, the algorithm goes on according to that reported in the proposed stabilization approach, until reaching the steady state equilibrium point IP^3. The results are reported in row 3 of Table 5.22. The system operating in this IP^3 is now transiently stable since the system's OMIB equivalent satisfies the stable condition (5.15) with a positive stable margin of η_{st}=+0.057*pu-rad*, such that the algorithm ends at 3 iterations. The voltage profile and active power dispatch associated to this IP^3 are shown in Fig. 5.16 (*a*) and (*b*), respectively. It must be pointed out that the computed steady state point IP^3 is close to the initial operating point IP^0, as corroborated by comparing Fig. 5.14 and Fig. 5.16 and their corresponding generation costs given in Table 5.22.

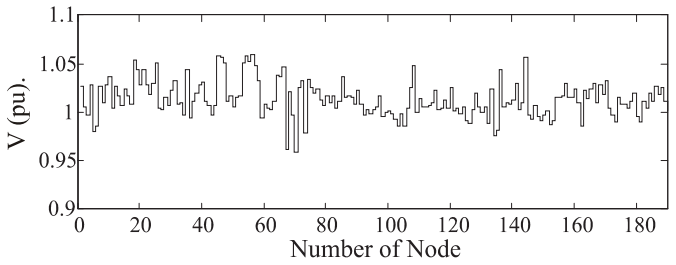

a) Voltage profile

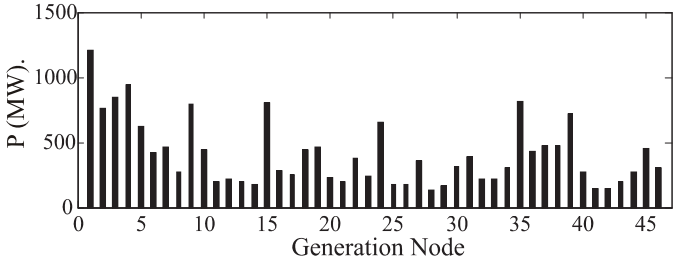

b) Active power dispatch

Fig. 5.16. Transiently stable steady state equilibrium point IP^3 of the Mexican system.

The stable condition of this system is twofold corroborated by observing the machines's rotor dynamics w.r.t. COI as illustrated in Fig. 5.17. Where the most advanced machines are the same to those declared as critical machines at the beginning of the stabilization process.

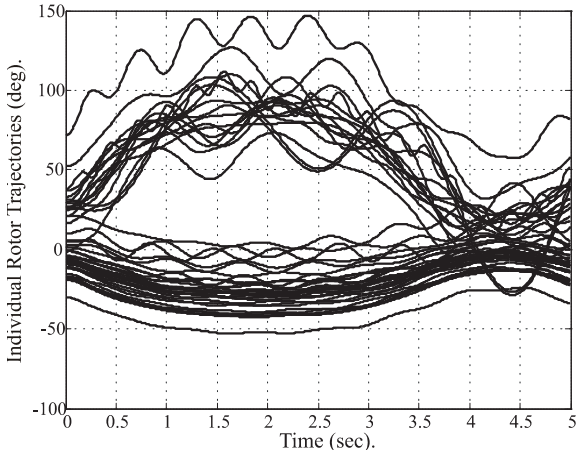

Fig. 5.17. Stable angular trajectories for the Mexican system initially operating at IP^3.

5.7. Approach II: Comparison to other approaches

This section presents numerical comparisons of the results of the proposed approaches with the ones of approaches reported by other authors considering the systems analyzed in the last sections.

5.7.1. Approach II: Three-Machine, Nine-Bus system results comparison

In this section the final results obtained by the proposed Approach II are compared to those obtained using Approach I and different Global TSC-OPF methods reported in the literature. These comparisons are performed based on the results shown in Table 5.23. The results related to the proposed approaches I and II correspond to those obtained in sections

5.4.1 and 5.6.1, respectively. The most economic dispatch corresponds to the one obtained by applying a conventional OPF to the base case, but for this economic operative condition the system is not transiently secure for the specified contingency scenario. All approaches reported in this table consider this power dispatch as base case to compute a new transiently stable equilibrium point. In [Nguyen and Pai, 2003], the secure operating point is computed using a conventional OPF and generation rescheduling based on a trajectory sensitivity method, which yields the less economic secure power dispatch. In [Cai et al., 2008] a differential evolution global search algorithm is used, but due to the selected transient stability constraint, the contingency scenario is over-stabilized at the computed transiently stable equilibrium point.

Table 5.23. Comparison of power dispatches of the 9-bus system using Approach II

Node	**OPF Dispatch (MVA)**					
	Base OPF	**Approach I**	**Approach II**	**Zárate-Miñano et al., 2010**	**Nguyen and Pai, 2003**	**Cai et al., 2008**
1	105.93	**121.55**	**117.62**	117.85	170.20	130.94
2	113.05	**99.79**	**105.78**	103.50	48.94	94.46
3	99.24	**96.57**	**94.89**	96.66	98.74	93.09
Cost ($/hr)	1, 132.18	**1, 135.2**	**1, 134.71**	1, 134.01	1, 191.56	1, 140.06

The TSC-OPF approach already proposed in [Zárate-Miñano et al., 2010] and proposed approaches I and II use the transient stability index based on an OMIB equivalent rotor angle limit in a different way, but calculate a similar active power dispatch and generation cost.

The results obtained by our proposed Approach II compare well with those obtained by Approach I and the reported in [Zárate-Miñano et al., 2010]. But in addition, it is very important to point out that the proposed Approach II has a paramount important advantage with respect to all the other Global TSC-OPF approaches mentioned in Table 5.23: its TSC-OPF model dimension is much smaller and comparable to that of a conventional OPF approach since the optimization model is mainly composed of steady state constraints. On the other hand, the stability constraint (5.19) and (5.21) considered in proposed approaches I and II, respectively, are only specified in terms of machine angles, which makes these approaches applicable to a system with any degree of modeling detail.

5.7.2. Approach II: New England system results comparison

In this section the New England system is considered to carry out the comparison of results obtained by the proposed Approach II, Approach I and the one reported in [Layden and Jeyasurya, 2004]. The final results obtained by approaches I and II in the study cases of sections 5.4.2 and 5.6.2, respectively, are summarized in Table 5.24 together with those reported in [Layden and Jeyasurya, 2004].

Table 5.24. Comparison results for New England system using Approach II

Proposal	**Generation Cost** (*$/hr*)	***CCT*** (*ms*)
Approach I	60,916.8	107.1
Approach II	60,906.7	100.5
Layden and Jeyasurya, 2004	61, 148.0	159.0

The proposed Approach II obtains the lowest cost and guarantees system stability with a *CCT* value which is only 0.5% above of the *CCT* originally specified of 100*ms*. Approach I yields good results (7% above the specified clearing time), whilst approach in [Layden and Jeyasurya, 2004] achieves the less economic dispatch and the most conservative security constrained steady state operating point. On the other hand, if it is considered that the integration interval is given by $T=[t_0, t_{end}]$, where t_{end} is arbitrarily defined as 1.5*s* in [Layden and Jeyasurya, 2004], whilst SIME finds the time to instability as t_u=0.5s, such that $t_{end} = t_u$, then the number of dynamic plus stability constraints employed in [Layden and Jeyasurya, 2004], and in approaches I and II, for a time step Δt=0.01, are respectively 14850, 4901 and only 1.

Despite Approach I reduces the computational burden of global TSC-OPF approaches, Approach II reduces the size of the programming problem to the minimum and importantly improves not only the practical applicability of the proposed Global TSC-OPF Approach II, but its numerical solution feasibility, by importantly reducing the number of constraints to be considered (and respected) and the complexity of the resulting nonlinear programming problem.

5.8. Size of the TSC-OPF model derived by different approaches

In order to numerically assess the size of the TSC-OPF model derived by different transient stability preventive control approaches, the number of dynamic plus stability constraints associated to the test systems considered in this chapter is computed in accordance with Table 5.14. To accomplish this objective, it is considered that the values of the upper integration interval t_{end} and time to instability t_u computed by SIME are 1.5s and 0.5s, respectively. The integration time step length is set as Δt=0.01. Taken into account these parameters, the number of dynamic plus stability constraints associated to the TSC-OPF model formulated for each one of the test systems by using different approaches is shown in Table 5.25.

Table 5.25. Size of the TSC-OPF model.

System	Number of stability plus dynamic constraints employed in,				
	Gan et al., 2000	La Scala et al., 1998	Zárate-Miñano et al., 2010	Approach I	Approach II
3-machine 9-bus	4050	3750	3750	1201	1
10-machine 39-bus	16200	14850	14850	4901	1
46-machine 190-bus	79050	71850	71850	23601	1

Table 5.25 shows that for any of the given test systems the proposed Approach I reduces the number of dynamic plus stability constraints by 70% w.r.t that reported in [Gan et al., 2000], and by 67% w.r.t. the proposals reported in [La Scala et al., 1998; Zárate-Miñano et al., 2010]. On the other hand, it must be noted that the proposed Approach II reduces the number of dynamic plus stability constraints by almost 100% w.r.t. any of the other approaches. These results indicates that proposed approach I and II substantially reduce the size of the TSC-OPF problem, but without affecting the solution optimality, as indicated by the results comparisons given in sections 5.4 and 5.7.

5.9. Conclusions

In this chapter two different novel SIME-based TSC-OPF approaches have been presented, they were proposed in order to reduce the huge computational burden associated with transient stability control global approaches. Both proposed approaches formulate their corresponding non-heuristic stability constraint based on the OMIB equivalent rotor angle equation derived by SIME method, which reduces to only one single constraint the number of constraints used to represent the system stability limits into TSC-OPF approaches. The main differences of Approach II w.r.t. Approach I are derived from the fact of that the later takes advantage of the quasi-linear relationship between the stability margin and the OMIB equivalent initial angular deviation. This advantage allows only considering into the TSC-OPF formulation a single stability constraint applied at the system steady state operating point, eliminating the (usually large) sets of dynamic and transient stability constraints required by other TSC-OPF formulations. The stabilization procedure is performed in the Euclidian space by means of an inter-(extra-)polation process, which yields a transiently stable steady state operating point that ensures the system's stability for the defined contingency scenario.

Comparisons between the proposed approaches and those presented by other authors are carried out in terms of programming problem size and complexity, as well as in numerical results accuracy. These comparisons clearly show the main advantages of the proposed approaches over those other proposals. SIME method stability assessment and sensitivity analysis make all advantages of the new global TSC-OPF approaches possible.

For the sake of clarity, the prowess of the proposed approaches has been illustrated in detail by different numerical examples. It is important to point out that the proposed approaches have not limitation on the power plant components modeling detail or system size.

Chapter 6

General Conclusions and Suggestions for Future Research Work

6.1. General Conclusions

The OPF tool has been widely accepted for assessing steady state and recommended control action for both off-line and on-line power system studies. Since its early stages the demand of this powerful tool has increased, such that many researchers have been investigating the way of solving the OPF problem in a more efficient and accurate way. Different techniques ranging from nonlinear programming to heuristic optimization techniques has been employed to deal with the complex problem that the conventional OPF represents. Despite that, modern power system are operating into a competitive and stressed environment, imposing more strict and complex requirements for solving in accurate and efficient way the OPF problem. As an example, modern power systems operate in a deregulated environment that seeks for economic benefits of supplying electric energy to the load centers or other interconnected power systems. Under this competitive environment the electric companies must provide to costumers a reliable product at competitive price. Reliability is composed of adequacy and security, this implies that economy and security requirements must be addressed in an integrated way for proper power system operation, despite both economy and security are opposed requirements.

Conventional OPF, in some sense, can be readily applied to handle in an integrated way static security and economy requirements of power systems. However, the conventional OPF must be accurately adjusted to consider modern power components that affect the steady state operation of power systems, otherwise static security and recommended control actions could not be properly assessed. Due to its control capabilities, the VSC-HVDC systems represent an option to send considerable amounts of electric energy along large distances or between interconnected power systems. In this research work, the steady state constraints representing the physical laws and operative limits that govern the steady state operation of a VSC-HVDC system are included into the conventional OPF. This development allows exploiting the device's capabilities whilst the given objective function is optimized under the considered static security and operative constraints.

In addition to the competitive environment, the rate of growth of the electric energy demand is much higher than the power system's supply capabilities. As result, the power systems are operated near their stability limits. The occurrence of instabilities that leave without electric energy the costumers of a part or the entire power system are the consequence of operating the power system in that stressed conditions. Contingency

scenarios of this kind might be preventively avoided in control centers by executing preventive control actions once a harmful credible contingency is declared.

The abovementioned issue is clearly associated to the dynamic security of power systems, such that in this research work the transient stability is considered as a main factor for assessing preventive control actions. This research work conciliates both economical requirements and transient stability limits into a conventional OPF. The stability limits are represented through two different stability constraints based on the proposed OMIB equivalent rotor angle limit. In addition to the OMIB equivalent structure, SIME salient parameters are used to derive the two proposed general, non heuristic, efficient and accurate transient stability preventive control approaches. The new single stability constraint is only specified in terms of machine angles, which makes the proposed approaches applicable to a power system with any degree of modeling detail and size. The solution of the proposed TSC-OPF model yields an optimal operating point whose mechanical power dispatch ensures the system transient stability for a credible harmful contingency. Therefore, the transient stability preventive control actions can be designed based on this optimal steady state operating point.

6.2. Suggestions for Future Research Work

Interesting research work could be carried out taking as basis the proposals presented in this document.

It could be interesting to consider detailed models of the synchronous machine and controls into the proposed approaches. This would allow computing more realistic results.

The proposed approaches consider that there is only one credible harmful contingency scenario; it should be investigated the stabilization of multiples contingencies. This topic has been well investigated in transient stability sequential approaches, but very promising results have not been reported using global approaches.

Available transfer capability is a very interesting problem in modern power systems operation. This problem could be readily solved taking as base the proposed transient stability control approaches.

The approach II was more efficient than proposed approach I, however it could be even enhanced in terms of computational effort. It should be achieved by controlling the OMIB equivalent mechanical power, instead of controlling the OMIB equivalent rotor angle initial condition.

The inclusion of modern power system devices, such as FACTS controllers, into the transient stability control procedures might be of interest. The effect on transient stability control has not been widely investigated by any research group.

Appendix A Elements of the Hessian Matrix

The elements of submatrices $\boldsymbol{W}_{ij}$ (i,j=1,2,3,4,5,6) of (3.33) corresponding to the second partial derivatives of the VSC-HVDC Lagrangian function $\mathcal{L}_{km}^{C}$ are given in this Appendix.

$$W_{1,1}=\left[\begin{array}{c|c|c|c} \dfrac{\partial^2 \mathcal{L}_{km}^{C}}{\partial V_k^2} & \dfrac{\partial^2 \mathcal{L}_{km}^{C}}{\partial V_k \partial \theta_k} & \dfrac{\partial^2 \mathcal{L}_{km}^{C}}{\partial V_k \partial \lambda_{pk}} & \dfrac{\partial^2 \mathcal{L}_{km}^{C}}{\partial V_k \partial \lambda_{qk}} \\ \hline \dfrac{\partial^2 \mathcal{L}_{km}^{C}}{\partial \theta_k \partial V_k} & \dfrac{\partial^2 \mathcal{L}_{km}^{C}}{\partial \theta_k^2} & \dfrac{\partial^2 \mathcal{L}_{km}^{C}}{\partial \theta_k \partial \lambda_{pk}} & \dfrac{\partial^2 \mathcal{L}_{km}^{C}}{\partial \theta_k \partial \lambda_{qk}} \\ \hline \dfrac{\partial^2 \mathcal{L}_{km}^{C}}{\partial \lambda_{pk} \partial V_k} & \dfrac{\partial^2 \mathcal{L}_{km}^{C}}{\partial \lambda_{pk} \partial \theta_k} & 0 & 0 \\ \hline \dfrac{\partial^2 \mathcal{L}_{km}^{C}}{\partial \lambda_{qk} \partial V_k} & \dfrac{\partial^2 \mathcal{L}_{km}^{C}}{\partial \lambda_{qk} \partial \theta_k} & 0 & 0 \end{array}\right] \quad \text{A.1}$$

$$W_{1,3}=\left[\begin{array}{cc|cc|c|c} \dfrac{\partial^2 \mathcal{L}_{km}^{C}}{\partial V_k \partial V_{Ck}} & \dfrac{\partial^2 \mathcal{L}_{km}^{C}}{\partial V_k \partial \theta_{Ck}} & 0 & 0 \\ \hline \dfrac{\partial^2 \mathcal{L}_{km}^{C}}{\partial \theta_k \partial V_{Ck}} & \dfrac{\partial^2 \mathcal{L}_{km}^{C}}{\partial \theta_k \partial \theta_{Ck}} & 0 & 0 \\ \hline \dfrac{\partial^2 \mathcal{L}_{km}^{C}}{\partial \lambda_{pk} \partial V_{Ck}} & \dfrac{\partial^2 \mathcal{L}_{km}^{C}}{\partial \lambda_{pk} \partial \theta_{Ck}} & 0 & 0 \\ \hline \dfrac{\partial^2 \mathcal{L}_{km}^{C}}{\partial \lambda_{qk} \partial V_{Ck}} & \dfrac{\partial^2 \mathcal{L}_{km}^{C}}{\partial \lambda_{qk} \partial \theta_{Ck}} & 0 & 0 \end{array}\right] \quad \text{A.2}$$

$$W_{1,4}=\left[\begin{array}{ccc|c} \dfrac{\partial^2 \mathcal{L}_{km}^{C}}{\partial V_k \partial \lambda_{CD}} & \dfrac{\partial^2 \mathcal{L}_{km}^{C}}{\partial V_k \partial \lambda_{CP_{km}}} & \dfrac{\partial^2 \mathcal{L}_{km}^{C}}{\partial V_k \partial \lambda_{CQ_{km}}} & 0 \\ \hline \dfrac{\partial^2 \mathcal{L}_{km}^{C}}{\partial \theta_k \partial \lambda_{CD}} & \dfrac{\partial^2 \mathcal{L}_{km}^{C}}{\partial \theta_k \partial \lambda_{CP_{km}}} & \dfrac{\partial^2 \mathcal{L}_{km}^{C}}{\partial \theta_k \partial \lambda_{CQ_{km}}} & 0 \\ \hline 0 & 0 & 0 & 0 \\ \hline 0 & 0 & 0 & 0 \end{array}\right] \quad \text{A.3}$$

$$W_{1,6}=\left[\begin{array}{ccc|c} 0 & 0 & 0 & \dfrac{\partial^2 \mathcal{L}_{km}^{C}}{\partial V_k \partial \lambda_{r_{Ck}}} & 0 \\ \hline 0 & 0 & 0 & \dfrac{\partial^2 \mathcal{L}_{km}^{C}}{\partial \theta_k \partial \lambda_{r_{Ck}}} & 0 \\ \hline 0 & 0 & 0 & 0 & 0 \\ \hline 0 & 0 & 0 & 0 & 0 \end{array}\right] \quad \text{A.4}$$

$$W_{2,2}=\left[\begin{array}{c|c|c|c} \dfrac{\partial^2 \mathcal{L}_{km}^{C}}{\partial V_m^2} & \dfrac{\partial^2 \mathcal{L}_{km}^{C}}{\partial V_m \partial \theta_m} & \dfrac{\partial^2 \mathcal{L}_{km}^{C}}{\partial V_m \partial \lambda_{pm}} & \dfrac{\partial^2 \mathcal{L}_{km}^{C}}{\partial V_m \partial \lambda_{qm}} \\ \hline \dfrac{\partial^2 \mathcal{L}_{km}^{C}}{\partial \theta_m \partial V_m} & \dfrac{\partial^2 \mathcal{L}_{km}^{C}}{\partial \theta_m^2} & \dfrac{\partial^2 \mathcal{L}_{km}^{C}}{\partial \theta_m \partial \lambda_{pm}} & \dfrac{\partial^2 \mathcal{L}_{km}^{C}}{\partial \theta_m \partial \lambda_{qm}} \\ \hline \dfrac{\partial^2 \mathcal{L}_{km}^{C}}{\partial \lambda_{pm} \partial V_m} & \dfrac{\partial^2 \mathcal{L}_{km}^{C}}{\partial \lambda_{pm} \partial \theta_m} & 0 & 0 \\ \hline \dfrac{\partial^2 \mathcal{L}_{km}^{C}}{\partial \lambda_{qm} \partial V_m} & \dfrac{\partial^2 \mathcal{L}_{km}^{C}}{\partial \lambda_{qm} \partial \theta_m} & 0 & 0 \end{array}\right] \quad \text{A.5}$$

$$W_{2,3}=\left[\begin{array}{cc|cc|c|c} 0 & 0 & \dfrac{\partial^2 \mathcal{L}_{km}^{C}}{\partial V_m \partial V_{Cm}} & \dfrac{\partial^2 \mathcal{L}_{km}^{C}}{\partial V_m \partial \theta_{Cm}} \\ \hline 0 & 0 & \dfrac{\partial^2 \mathcal{L}_{km}^{C}}{\partial \theta_m \partial V_{Cm}} & \dfrac{\partial^2 \mathcal{L}_{km}^{C}}{\partial \theta_m \partial \theta_{Cm}} \\ \hline 0 & 0 & \dfrac{\partial^2 \mathcal{L}_{km}^{C}}{\partial \lambda_{pm} \partial V_{Cm}} & \dfrac{\partial^2 \mathcal{L}_{km}^{C}}{\partial \lambda_{pm} \partial \theta_{Cm}} \\ \hline 0 & 0 & \dfrac{\partial^2 \mathcal{L}_{km}^{C}}{\partial \lambda_{qm} \partial V_{Cm}} & \dfrac{\partial^2 \mathcal{L}_{km}^{C}}{\partial \lambda_{qm} \partial \theta_{Cm}} \end{array}\right] \quad \text{A.6}$$

$$W_{2,4}=\left[\begin{array}{cc|cc} \dfrac{\partial^2 \mathcal{L}_{km}^{C}}{\partial V_m \partial \lambda_{CD}} & 0 & 0 & \dfrac{\partial^2 \mathcal{L}_{km}^{C}}{\partial V_k \partial \lambda_{CQ_{mk}}} \\ \hline \dfrac{\partial^2 \mathcal{L}_{km}^{C}}{\partial \theta_m \partial \lambda_{CD}} & 0 & 0 & \dfrac{\partial^2 \mathcal{L}_{km}^{C}}{\partial \theta_m \partial \lambda_{CQ_{mk}}} \\ \hline 0 & 0 & 0 & 0 \\ \hline 0 & 0 & 0 & 0 \end{array}\right] \quad \text{A.7}$$

$$W_{2,5}=\left[\begin{array}{c|c|c|c} 0 & \dfrac{\partial^2 \mathcal{L}_{km}^{C}}{\partial V_m \partial V_{CDm}} & 0 & 0 \\ \hline 0 & \dfrac{\partial^2 \mathcal{L}_{km}^{C}}{\partial \theta_m \partial V_{CDm}} & 0 & 0 \\ \hline 0 & 0 & 0 & 0 \\ \hline 0 & 0 & 0 & 0 \end{array}\right] \quad \text{A.8}$$

$$W_{2,6} = \begin{bmatrix} \frac{\partial^2 \mathcal{L}^C_{km}}{\partial V_m \partial \lambda_V} & 0 & 0 & 0 & \frac{\partial^2 \mathcal{L}^C_{km}}{\partial V_m \partial \lambda_{r_{Cm}}} \\ \frac{\partial^2 \mathcal{L}^C_{km}}{\partial \theta_m \partial \lambda_V} & 0 & 0 & 0 & \frac{\partial^2 \mathcal{L}^C_{km}}{\partial \theta_m \partial \lambda_{r_{Cm}}} \\ 0 & 0 & 0 & 0 & 0 \\ 0 & 0 & 0 & 0 & 0 \end{bmatrix} \quad \text{A.9}$$

$$W_{3,3} = \begin{bmatrix} \frac{\partial^2 \mathcal{L}^C_{km}}{\partial V^2_{Ck}} & \frac{\partial^2 \mathcal{L}^C_{km}}{\partial V_{Ck} \partial \theta_{Ck}} & 0 & 0 \\ \frac{\partial^2 \mathcal{L}^C_{km}}{\partial \theta_{Ck} \partial V_{Ck}} & \frac{\partial^2 \mathcal{L}^C_{km}}{\partial \theta^2_{Ck}} & 0 & 0 \\ 0 & 0 & \frac{\partial^2 \mathcal{L}^C_{km}}{\partial V^2_{Cm}} & \frac{\partial^2 \mathcal{L}^C_{km}}{\partial V_{Cm} \partial \theta_{Cm}} \\ 0 & 0 & \frac{\partial^2 \mathcal{L}^C_{km}}{\partial \theta_{Cm} \partial V_{Cm}} & \frac{\partial^2 \mathcal{L}^C_{km}}{\partial \theta^2_{Cm}} \end{bmatrix} \quad \text{A.10}$$

$$W_{3,4} = \begin{bmatrix} \frac{\partial^2 \mathcal{L}^C_{km}}{\partial V_{Ck} \partial \lambda_{CD}} & \frac{\partial^2 \mathcal{L}^C_{km}}{\partial V_{Ck} \partial \lambda_{CP_{km}}} & \frac{\partial^2 \mathcal{L}^C_{km}}{\partial V_{Ck} \partial \lambda_{CQ_{km}}} & 0 \\ \frac{\partial^2 \mathcal{L}^C_{km}}{\partial \theta_{Ck} \partial \lambda_{CD}} & \frac{\partial^2 \mathcal{L}^C_{km}}{\partial \theta_{Ck} \partial \lambda_{CP_{km}}} & \frac{\partial^2 \mathcal{L}^C_{km}}{\partial \theta_{Ck} \partial \lambda_{CQ_{km}}} & 0 \\ \frac{\partial^2 \mathcal{L}^C_{km}}{\partial V_{Cm} \partial \lambda_{CD}} & 0 & 0 & \frac{\partial^2 \mathcal{L}^C_{km}}{\partial V_{Cm} \partial \lambda_{CQ_{mk}}} \\ \frac{\partial^2 \mathcal{L}^C_{km}}{\partial \theta_{Cm} \partial \lambda_{CD}} & 0 & 0 & \frac{\partial^2 \mathcal{L}^C_{km}}{\partial \theta_{Cm} \partial \lambda_{CQ_{mk}}} \end{bmatrix} \quad \text{A.11}$$

$$W_{3,5} = \begin{bmatrix} 0 & 0 & 0 & 0 \\ 0 & 0 & 0 & 0 \\ 0 & \frac{\partial^2 \mathcal{L}^C_{km}}{\partial V_{Cm} \partial V_{DCm}} & 0 & 0 \\ 0 & \frac{\partial^2 \mathcal{L}^C_{km}}{\partial \theta_{Cm} \partial V_{DCm}} & 0 & 0 \end{bmatrix} \quad \text{A.12}$$

$$W_{3,6} = \begin{bmatrix} 0 & \frac{\partial^2 \mathcal{L}^C_{km}}{\partial V_{Ck} \partial \lambda_{tk}} & 0 & \frac{\partial^2 \mathcal{L}^C_{km}}{\partial V_{Ck} \partial \lambda_{r_{Ck}}} & \\ 0 & 0 & 0 & \frac{\partial^2 \mathcal{L}^C_{km}}{\partial \theta_{Ck} \partial \lambda_{r_{Ck}}} & 0 \\ \frac{\partial^2 \mathcal{L}^C_{km}}{\partial V_{Cm} \partial \lambda_V} & 0 & \frac{\partial^2 \mathcal{L}^C_{km}}{\partial V_{Cm} \partial \lambda_{tm}} & 0 & \frac{\partial^2 \mathcal{L}^C_{km}}{\partial V_{Cm} \partial \lambda_{r_{Cm}}} \\ \frac{\partial^2 \mathcal{L}^C_{km}}{\partial \theta_{Cm} \partial \lambda_V} & 0 & 0 & 0 & \frac{\partial^2 \mathcal{L}^C_{km}}{\partial \theta_{Cm} \partial \lambda_{r_{Cm}}} \end{bmatrix} \quad \text{A.13}$$

$$W_{4,4} = \begin{bmatrix} 0 & 0 & 0 & 0 \\ 0 & 0 & 0 & 0 \\ 0 & 0 & 0 & 0 \\ 0 & 0 & 0 & \frac{\partial^2 \mathcal{L}^C_{km}}{\partial \lambda^2_{CQ_{mk}}} \end{bmatrix} \quad \text{A.14}$$

$$W_{4,5} = \begin{bmatrix} 0 & \frac{\partial^2 \mathcal{L}^C_{km}}{\partial \lambda_{CD} \partial V_{DCm}} & 0 & 0 \\ 0 & 0 & 0 & 0 \\ 0 & 0 & 0 & 0 \\ 0 & 0 & 0 & 0 \end{bmatrix} \quad \text{A.15}$$

$$W_{5,5} = \begin{bmatrix} 0 & 0 & \frac{\partial^2 \mathcal{L}^C_{km}}{\partial V_{DCk} \partial M_{Ck}} & 0 \\ 0 & \frac{\partial^2 \mathcal{L}^C_{km}}{\partial V_{DCm} \partial V_{DCm}} & 0 & \frac{\partial^2 \mathcal{L}^C_{km}}{\partial V_{DCm} \partial M_{Cm}} \\ \frac{\partial^2 \mathcal{L}^C_{km}}{\partial M_{Ck} \partial V_{DCk}} & 0 & 0 & 0 \\ 0 & \frac{\partial^2 \mathcal{L}^C_{km}}{\partial M_{Cm} \partial V_{DCm}} & 0 & 0 \end{bmatrix} \quad \text{A.16}$$

$$W_{5,6} = \left[\begin{array}{c|c|c|c|c} \dfrac{\partial^2 \bar{\mathcal{L}}_{km}^C}{\partial V_{DCk}\partial \lambda_V} & \dfrac{\partial^2 \bar{\mathcal{L}}_{km}^C}{\partial V_{DCk}\partial \lambda_{tk}} & 0 & 0 & 0 \\ \hline \dfrac{\partial^2 \bar{\mathcal{L}}_{km}^C}{\partial V_{DCm}\partial \lambda_V} & 0 & \dfrac{\partial^2 \bar{\mathcal{L}}_{km}^C}{\partial V_{DCm}\partial \lambda_{tm}} & 0 & 0 \\ \hline 0 & \dfrac{\partial^2 \bar{\mathcal{L}}_{km}^C}{\partial M_{Ck}\partial \lambda_{tk}} & 0 & 0 & 0 \\ \hline 0 & 0 & \dfrac{\partial^2 \bar{\mathcal{L}}_{km}^C}{\partial M_{Cm}\partial \lambda_{tm}} & 0 & 0 \end{array}\right] \quad \text{A.17}$$

$$W_{6,6} = \left[\begin{array}{c|c|c|c|c} 0 & 0 & 0 & 0 & 0 \\ \hline 0 & 0 & 0 & 0 & 0 \\ \hline 0 & 0 & 0 & 0 & 0 \\ \hline 0 & 0 & 0 & \dfrac{\partial^2 \bar{\mathcal{L}}_{km}^C}{\partial \lambda_{r_{Ck}}^2} & 0 \\ \hline 0 & 0 & 0 & 0 & 0 \end{array}\right] \quad \text{A.18}$$

Appendix B Data of the 3-machine 9-bus system

The 3-machine 9-bus system diagram and data were taken from [Sauer and Pai, 1998], in this appendix are given on a MVA base of 100MW as follows,

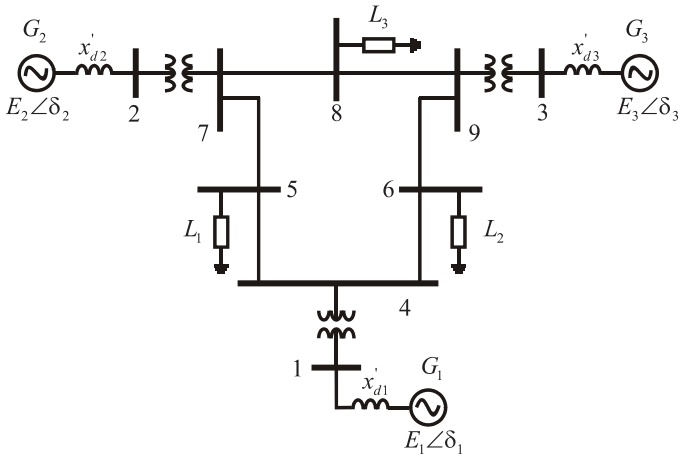

Fig. B.1. One-line diagram of the IEEE 3-machine 9-bus test system.

Table B.I. Number of nodes and plant components

Number of components					
Nodes	**Transmission lines**	**Transformers**	**Generators**	**Loads**	**Slack node**
9	6	3	3	3	1

Table B.II. Network parameters

Nodes		***R*** (*pu*)	***X*** (*pu*)	***B/2*** (*pu*)
4	5	0.0100	0.0850	0.0880
5	7	0.0320	0.1610	0.1530
7	8	0.0085	0.0720	0.0745
8	9	0.0119	0.1008	0.1045
9	6	0.0390	0.1700	0.1790
6	4	0.0170	0.0920	0.0790

Table B.III. Transformer parameters

Nodes		R_s (*pu*)	X_s (*pu*)	**Tap Ratio**	
				Tv	**Uv**
1	4	0.0000	0.0576	1	1
2	7	0.0000	0.0625	1	1
3	9	0.0000	0.0586	1	1

Table B.IV. Load parameters

Node	***P*** (*pu*)	***Q*** (*pu*)
1	1.25	0.50
2	0.90	0.30
3	1.00	0.35

Table B.VI. Generator's parameters

Node	x'_d (*pu*)	***H*** (*pu-sec*)	***D*** (*sec/rad*)
1	0.0608	23.64	0.0125
2	0.1198	6.40	0.0068
3	0.1813	3.01	0.0048

Appendix C Data of the New England system

The data of this system were taken from [Pai, 1989], whilst the generator's quadratic cost curves and ratings were taken from [Nguyen and Pai, 2003], they are given on a MVA base of 100MW.

Table C.I. Number of nodes and plant components

Number of components					
Nodes	**Transmission lines**	**Transformers**	**Generators**	**Loads**	**Slack node**
39	34	12	10	19	39

Table C.II. Network parameters

Nodes		***R*** *(pu)*	***X*** *(pu)*	***B/2*** *(pu)*
1	2	0.0035	0.0411	0.6987
1	39	0.001	0.025	0.75
2	3	0.0013	0.0151	0.2572
2	25	0.007	0.0086	0.146
3	4	0.0013	0.0213	0.2214
3	18	0.0011	0.0133	0.2138
4	5	0.0008	0.0128	0.1342
4	14	0.0008	0.0129	0.1382
5	6	0.0002	0.0026	0.0434
5	8	0.0008	0.0112	0.1476
6	7	0.0006	0.0092	0.113
6	11	0.0007	0.0082	0.1389
7	8	0.0004	0.0046	0.078
8	9	0.0023	0.0363	0.3804
9	39	0.001	0.025	1.2
10	11	0.0004	0.0043	0.0729
10	13	0.0004	0.0043	0.0729
13	14	0.0009	0.0101	0.1723
14	15	0.0018	0.0217	0.366
15	16	0.0009	0.0094	0.171
16	17	0.0007	0.0089	0.1342
16	19	0.0016	0.0195	0.304
16	21	0.0008	0.0135	0.2548
16	24	0.0003	0.0059	0.068
17	18	0.0007	0.0082	0.1319
17	27	0.0013	0.0173	0.3216
21	22	0.0008	0.014	0.2565
22	23	0.0006	0.0096	0.1845
23	24	0.0022	0.035	0.361
25	26	0.0032	0.0323	0.513
26	27	0.0014	0.0147	0.2396
26	28	0.0043	0.0474	0.7802
26	29	0.0057	0.0625	1.029
28	29	0.0014	0.0151	0.249

Table C.III. Transformer parameters

Nodes		R_s *(pu)*	X_s *(pu)*	**Tap Ratio**	
				Tv	**Uv**
12	11	0.0016	0.0435	1.006	1
12	13	0.0016	0.0435	1.006	1
6	31	0	0.025	1.07	1
10	32	0	0.02	1.07	1
19	33	0.0007	0.0142	1.07	1
20	34	0.0009	0.018	1.009	1
22	35	0	0.0143	1.025	1
23	36	0.0005	0.0272	1	1
25	37	0.0006	0.0232	1.025	1
2	30	0	0.0181	1.025	1
29	38	0.0008	0.0156	1.025	1
19	20	0.0007	0.0138	1.06	1

Table C.IV. Load parameters

Node	***P*** *(pu)*	***Q*** *(pu)*
3	322	2.4
4	500	184
7	233.8	84
8	522	176
12	7.5	88
15	320	153
16	329	32.3
18	158	30
20	628	103
21	274	115
23	247.5	84.6
24	308.6	-92.2
25	224	47.2
26	139	17
27	281	75.5
28	206	27.6
29	283.5	26.9
31	9.2	4.6
39	1104	250

Table C.V. Generator's parameters

Node	x_d' (*pu*)	*H* (*pu-sec*)	*D* (*sec/rad*)
30	0.031	42	0
31	0.0697	30.3	0
32	0.053	35.8	0
33	0.044	28.6	0
34	0.132	26	0
35	0.05	34.8	0
36	0.049	26.4	0
37	0.057	24.3	0
38	0.057	34.5	0
39	0.006	500	0

Table C.VI. Generator's cost curves and ratings

Node	A $\left(\frac{\$}{\text{hr}}\right)$	B $\left(\frac{\$}{\text{MWhr}}\right)$	C $\left(\frac{\$}{\text{MW}^2\text{hr}}\right)$	Rating (MW)
30	0	6.9	0.0193	350
31	0	3.7	0.0111	650
32	0	2.8	0.0104	800
33	0	4.7	0.0088	750
34	0	2.8	0.0128	650
35	0	3.7	0.0094	750
36	0	4.8	0.0099	750
37	0	3.6	0.0113	700
38	0	3.7	0.0071	900
39	0	3.9	0.0064	1200

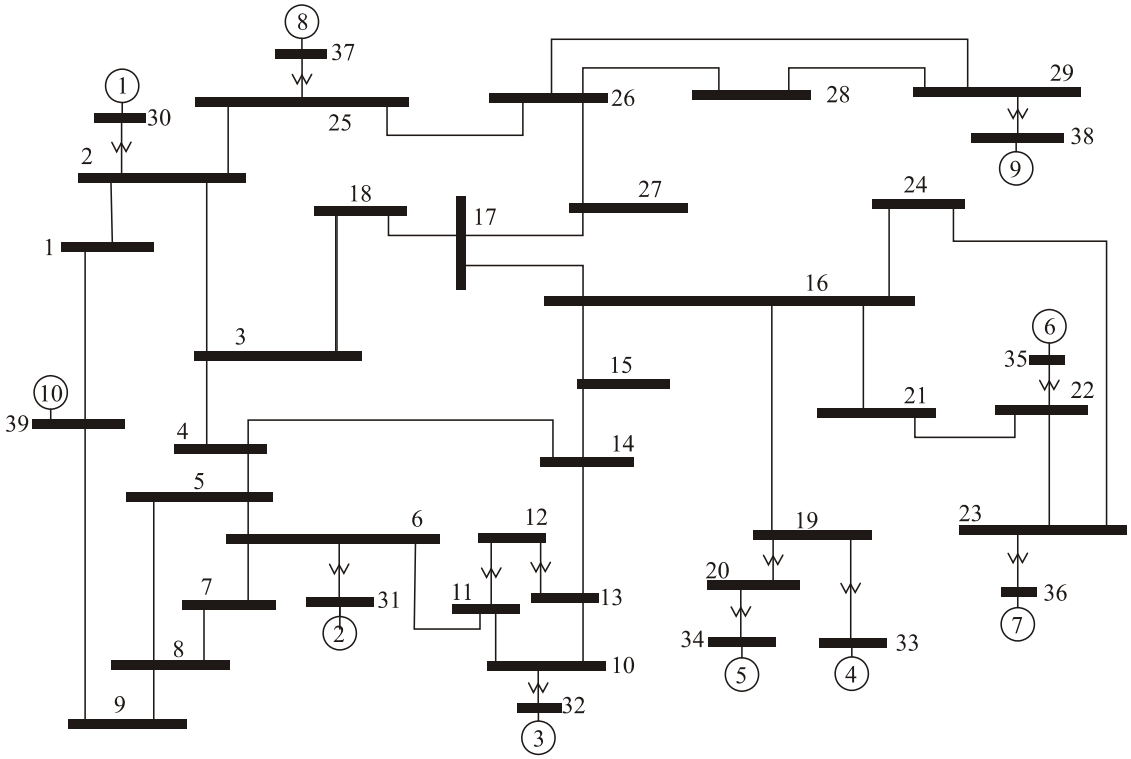

Fig. C.1. One-line diagram of the New England test system.

Bibliography

[Aboytes and Arroyo, 1986]
F. Aboytes and G. Arroyo, “Security assessment in the operation of longitudinal power systems,” *IEEE Trans. Power Syst.*, Vol. 1, No. 2, pp. 225-232, May. 1986.

[Alsac et al., 1990]
O. Alsac, J. Brigth, M. Prais, and B. Sttot, “Experiences with implementing optimal power flow for reactive scheduling in the Taiwan power system,” *IEEE Trans. Power Syst.*, Vol. 5, No. 3, pp. 697-711, Aug. 1990.

[Ambriz-Pérez, 1998]
H. Ambriz-Pérez: Flexible AC Transmission Systems Modelling in Optimal Power Flows Using Newton's Method, Ph.D. Thesis, University of Glasgow, 1998.

[Asplund, 2001]
G. Asplund, “Application of HVDC Light to power system enhancement,” in *Proc. 2001 IEEE-PES Winter Meeting*, Vol. 4, pp. 2498-2503.

[Abdel-Moamen and Padhy, 2003]
M.A. Abdel-Moamen and N.P. Padhy, “Optimal power flow incorporating FACTS devices-bibliography and survey,” in *Proc. 2003 IEEE-PES Trans. and Dist. Conf.*, Vol. 2, pp. 669-676.

[Angeles-Camacho et al., 2003]
C. Angeles-Camacho, O.L. Tortelli, E. Acha, and C.R. Fuerte-Esquivel, “Inclusion of a high voltage DC-voltage source converter model in a Newton-Raphson power flow algorithm,” *IEE Proc.-Gener. Transm. Distrib*, Vol. 150, No.6, pp. 691-696, Nov. 2003.

[Acha et al., 2004]
E. Acha, C. R. Fuerte Esquivel, H. Ambriz Pérez, C. Angeles Camacho: FACTS: Modelling and Simulation in Power Networks. John Wiley and Sons, 2004.

[ABB, 2005]
ABB power technologies AB, “Technical description of HVDC Light® technology,” Technical report, April 2005, available from http://www.abb.com.

[Bertsekas, 1979]
D.P. Bertsekas, “Convexification procedures and decomposition methods for nonconvex optimization problems,” Journal of Optimization Theory and Applications, Vol. 29, No. 2, pp. 169-197, Oct. 1979.

[Bertsekas, 1996]
D.P. Bertsekas, Constrained optimization and Lagrange multiplier methods. Athena Scientific, 1996.

[Bettiol et al., 1999]
A.L. Bettiol, L. Wehenkel, and M. Pavella, "Transient stability-constrained maximum allowable transfer," *IEEE Trans. on Power Syst.*, Vol.14, No.2, pp.654-659, May 1999.

[Bahrman et al., 2003]
M.P. Bahrman, J.G. Johansson, and B. Nilsson, “Voltage source converter transmission technologies-the right fit for the application,” in *Proc. 2003 IEEE-PES General Meeting*, Vol. 3, pp.1840-1847.

[Carpentier and Bornard, 1991]
J. Carpentier and P. Bornard, “Towards an integrated secure optimal operation of power systems,” in *Proc. IEE APSCOM-91 Conf.*, 16pp., Nov. 1991.

[Crisan and M. Mohtadi, 1992]
O. Crisan, and M. Mohtadi, “Efficient identification of binding inequality constraints in optimal power flow Newton approach,” *IEE Proc.-Gener. Transm. Distrib*, Vol. 139, No.5, pp. 365-370, Sept. 1992.

[Chen et al., 2001]
L. Chen, Y. Tada, H. Okamoto, R. Tanabe, and A. Ono. “Optimal operation solutions of power systems with transient stability constraints,” *IEEE Trans. Circuits Syst. I*, Vol.48, No.3, pp. 327-339, March 2001.

[Cai et al., 2008]
H.R. Cai, C.Y. Chung, and K.P. Wong, “Application of differential evolution algorithm for transient stability constrained optimal power flow,” *IEEE Trans. on Power Syst.*, Vol.23, No.2, May 2008.

[Ernst et al., 2001]
D. Ernst, D. Ruiz-Vega, M. Pavella, P. Hirsch, and D. Sobajic, “A unified approach to transient stability contingency filtering, ranking and assessment,” *IEEE Trans. Power Syst.*, vol. 16, pp. 435–443, Aug. 2001.

[Fouad and Jianzhong, 1993]
A. A. Fouad and T. Jianzhong, "Stability constrained optimal rescheduling of generation," *IEEE Trans. on Power Syst.*, Vol.8, No.1, pp.105-112, Feb., 1993.

[Gan et al., 2000]
D. Gan, R. J. Thomas, and R. D. Zimmerman, "Stability-constrained optimal power flow," *IEEE Trans. on Power Syst.*, Vol.15, No.2, May, pp.535-540, 2000.

[Gonzalez et al., 2009]
J. M. Gonzalez, C. A. Cañizares, and J. M. Ramirez, "Stability Modeling and Comparative Study of Series Vectorial Compensators," accepted for publication in *IEEE Transactions on Power Delivery*, May 2009, 11 pages.

[Gomez-Exposito et al., 2009]
A. Gómez-Expósito, A. J. Conejo and C. A. Cañizares. *Electric Energy Systems Analysis and Operation*. Boca Raton, FL: CRC, 2009.

[Hong, 1992]
Hong Y.Y.: ‘Enhanced Newton optimal power flow approach experiences in Taiwan power system’, *IEE Proc.-Gener. Transm. Distrib*, Vol. 139, No.3, pp. 205-210, May 1992.

[Hingorani and Gyugyi, 1999]
N.G. Hingorani and L. Gyugyi, Understanding FACTS Concepts and Technology of Flexible AC Transmission Systems. IEEE Press, 1999.

[Hakim et al., 2009]
L. Hakim, J. Kubokawa, Y. Yuan, T. Mitani, Y. Zoka, N. Yorino, Y. Niwa, K. Shimomura, and A. Takeuchi, “A study on the effect of generation shedding to total transfer capability by means of transient stability constrained optimal power flow,” *IEEE Trans. on Power Syst.*, Vol.24, No.1, pp.347-355, Feb. 2009.

[Huneault and Galiana, 2009]
M. Huneault and F. D. Galiana, "A survey of the optimal power flow literature," *IEEE Trans. on Power Syst.*, Vol.6, No.2, pp.762-770, May 1991.

[Kundur, 1994]
P. Kundur: Power System Stability and Control. McGraw Hill, 1994.

[Kuo and Bose, 1995]
D. H. Kuo, and A. Bose, "A generation rescheduling method to increase dynamic security of power systems," *IEEE Trans. on Power Syst.*, Vol.10, No.1, pp.68-76, Feb. 1995.

[Kundur et al., 2004]
P. Kundur, J. Paserba, V. Ajjarapu, G. Andersson, A. Bose, C. Canizares, N. Hatziargyriou, D. Hill, A. Stankovic, C. Taylor, T. Van Cutsem, and V. Vittal, “Definition and classification of power system stability,” *IEEE Trans. on Power Syst.*, Vol. 19, No. 2, May 2004.

[Luenberger, 1984]
D.G. Luenberger: ‘Introduction to Linear and Nonlinear Programming. Addison-Wesley Publishing Co., Second Edition, 1984.

[La Scala et al., 1996]
M. La Scala, G. Lorusso, R. Sbrizzai, and M. Trovato, “A qualitative approach to the transient stability analysis,” *IEEE Trans. Power Syst.*, Vol. 11, No. 4, pp. 1996–2002, Nov. 1996.

[La Scala et al., 1998]
M. La Scala, M. Trovato, and C. Antonelli, "On-line dynamic preventive control: an algorithm for transient security dispatch," *IEEE Trans. on Power Syst.*, Vol.13, No.2, pp.601-610, May 1998.

[Lee et al., 1998]
K. Y. Lee, M. A. Mohtadi, J. L. Ortiz and Y. M. Park, “Optimal operation of large-scale power systems,” *IEEE Trans. on Power Syst.* Vol.3, No.2, pp. 243-253, May 1998.

[Layden and Jeyasurya, 2004]
D. Layden and B. Jeyasurya, “Integrating security constraints in optimal power flow studies,” *Proc. of the 2004 IEEE PES General Meeting*, pp. 125-129.

[Maria and Findlay, 1987]
G.A. Maria, and J.A. Findlay, “A Newton optimal power flow program for Ontario Hydro EMS,” *IEEE Trans. Power Syst.*, Vol. 2, No. 3, pp. 576-584, Aug. 1987.

[Messina et al., 2002]
A.R. Messina , H. Hernández, E. Barocio, M. Ochoa, J. Arroyo “Coordinated application of FACTS controllers to damp out interarea oscillations”. Electric Power Systems Research 62 (2002) 43-53.

[Momoh et al., 1997]
J.A. Momoh, R.J. Koessler, M.S. Bond, B. Stott, D. Sun, A. Papalexopoulos, and P. Ristanovic, "Challenges to optimal power flow," *IEEE Trans. on Power Syst.* Vol.12, No.1, pp.444-455, Feb. 1997.

[Momoh et al., 1997]
J.A. Momoh, R.J. Koessler, M.S. Bond, B. Stott, and D. Sun, A. Papalexopoulos and P. Ristanovic, “Challenges to optimal power flow,” *IEEE Trans. Power Syst.* Vol. 12, No. 1, pp. 444-455, Feb. 1997.

[Momoh et al., 1999a]
J. A. Momoh, M.E. El-Hawari, and R. Adapa, “A review of selected optimal power flow literature to 1993: part I: nonlinear and quadratic programming approaches,” *IEEE Trans. Power Syst.*, Vol. 14, No. 1, pp. 96-104, February 1999.

[Momoh et al., 1999b]
J. A. Momoh, M.E. El-Hawari, and R. Adapa, “A review of selected optimal power flow literature to 1993 part II: Newton, linear programming and interior point methods,” *IEEE Trans. Power Syst.*, Vol. 14, No. 1, pp. 105-111, February 1999.

[Nocedal and Wright, 1999]
J. Nocedal and S. J. Wright: Numerical Optimization. Springer, 1999.

[Nguyen and Pai, 2003]
T.B. Nguyen and M.A. Pai, "Dynamic security-constrained rescheduling of power systems using trajectory sensitivities," *IEEE Trans. on Power Syst.*, Vol.18, No.2, pp. 848-854, May 2003.

[Pai, 1989]
M. A. Pai: Energy Function Analysis for Power System Stability. Kluwer, 1989.

[Pavella et al., 2000]
M. Pavella, D. Ernst, and D. Ruiz-Vega, Transient Stability of Power Systems: A Unified Approach to Assessment and Control. Kluwer, 2000.

[PTI Version 30.2.1]
Power Technologies International, “Reference manual: Version 30.2.1, PSS/E, Optimal Power Flows Module,” Siemens Power Transmission and Distribution, Inc. [Rafian et al., 1987] M. Rafian, M. J. H. Sterling and M. R. Irving,“ Real Time Power System Simulation,” in *Proc. IEE Conf.*, Vol, 134, pp. 206-223, 1987,

[Ruiz-Vega and Pavella, 2003]
D. Ruiz-Vega and M. Pavella, "A comprehensive approach to transient stability control. I. Near optimal preventive control," *IEEE Trans. on Power Syst.*, Vol.18, No.4, pp. 1446-1453, Nov. 2003.

[Stott, 1979]
B. Stott, "Power system dynamic respond calculations," *Proc. of the IEEE*, Special Issue on Computers in Power System Operations, Vol. 67, No. 2, pp. 219-241, Feb. 1979.

[Sun et al., 1984]
D.I. Sun, B. Ashley, B. Brewer, A. Hughes, and W.F. Tinney, "Optimal power flow by Newton approach," *IEEE Trans. On Power App. and Syst.*, Vol. PAS-103, No. 10, pp. 2864-2880, Oct. 1984.

[Stott et al., 1987]
B. Stott, O. Alsac and A.J. Monticelli, "Security Analysis and Optimization," *Proc. of the IEEE*, Special Issue on Computers in Power System Operations, Vol. 75, No. 12, pp. 1623-1644, Dec. 1987.

[Sun et al., 1988]
D.I. Sun, T.I. Hu, G.S. Lin, C.J. Lin, and C.M. Chen, "Experiences with implementing optimal power flow for reactive scheduling in the Taiwan power system," *IEEE Trans. Power Syst.*, Vol. 3, No. 3, pp. 1193-1200, Aug. 1988.

[Soman et al., 1994]
S.A. Soman, K. Parthasarathy and D. Thukaram, "Curtailed number and reduced controller movement optimization algorithms for real time voltage/reactive power control," *IEEE Trans. Power Syst.*, Vol. 9, No. 4, pp. 2035-2041, Nov. 1994.

[Sauer and Pai, 1998]
P. W. Sauer and M. A. Pai, *Power System Dynamics and Stability*. Prentice-Hall, 1998.

[Sun et al., 2004]
Y. Sun, Y. Xinlin, and H.F. Wang, "Approach for optimal power flow with transient stability constraints," *IEE Proc.-Gener. Transm. Distrib.*, Vol.151, No.1, pp. 8-18, Jan. 2004.

[Vittal, 2000]
V. Vittal, "Consequence and impact of electric utility industry restructuring on transient stability and small signal stability analysis," *Proc. Of IEEE*, Vol. 88, No. 2, pp. 196-207, Feb. 2000.

[Wollenberg and Wood, 1984]
B. Wollenberg and A. J. Wood, Power Generation, Operation and Control, John Wiley & Sons Inc., Second Edition, 1984.

[Xu et al., 1998]
X. Xu, R.M. Mathur, J. Jiang, G.J. Rogers and P. Kundur, "Modeling of generators and their controls in power system simulations using singular perturbations," *IEEE Trans. on Power Syst.*, Vol. 13, No. 1, pp. 109-114, Feb. 1998.

[Xia and Chan, 2006]
Y. Xia and K. W. Chan, "Dynamic constrained optimal power flow using semi-infinite programming," *IEEE Trans. on Power Syst.*, Vol. 21, No.3, pp. 1455-1457, Aug. 2006.

[Yuan et al., 2003]
Y. Yuan, J. Kubokawa and H. Sasaki, "A solution of optimal power flow with multicontingency transient stability constraints," *IEEE Trans. on Power Syst.*, Vol.18, No.3, pp. 1094-1102, Aug. 2003.

[Zhang, 2005]
X.P. Zhang, "Multiterminal voltage-sourced converter-based HVDC models for power flow analysis," *IEEE Trans. Power Syst.*, Vol. 19, No. 4, pp. 1877-1884, Nov. 2004.

[Zárate-Miñano et al., 2010]
R. Zárate-Miñano, T. Van Cutsem, F. Milano, and A.J. Conejo, "Securing transient stability using time-domain simulations within an optimal power flow," *IEEE Trans. on Power Syst.* Vol.25, No.1, pp. 243-253, Feb. 2010.